



DISCRETE FILM COOLING IN A  
ROCKET WITH CURVED WALLS

DISSERTATION

Jonathan Floyd McCall, P.E.

AFIT/DS/ENY/09-D02

DEPARTMENT OF THE AIR FORCE  
AIR UNIVERSITY

***AIR FORCE INSTITUTE OF TECHNOLOGY***

Wright-Patterson Air Force Base, Ohio

APPROVED FOR PUBLIC RELEASE; DISTRIBUTION UNLIMITED.

The views expressed in this thesis are those of the author and do not reflect the official policy or position of the United States Air Force, Department of Defense, or the United States Government.

DISCRETE FILM COOLING IN A  
ROCKET WITH CURVED WALLS

DISSERTATION

Presented to the Faculty  
Graduate School of Engineering and Management  
Air Force Institute of Technology  
Air University  
Air Education and Training Command  
In Partial Fulfillment of the Requirements for the  
Degree of Doctor of Philosophy

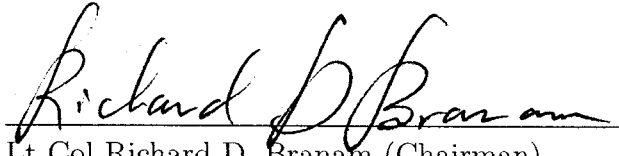
Jonathan Floyd McCall, P.E., B.S.A.E., M.S.A.E.  
Captain, USAF

December 2009


DISCRETE FILM COOLING IN A  
ROCKET WITH CURVED WALLS

Jonathan Floyd McCall, P.E., B.S.A.E., M.S.A.E.  
Captain, USAF

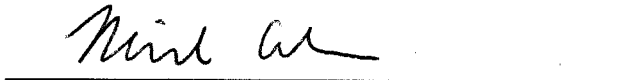
Approved:

  
Lt Col Richard D. Branam (Chairman)


30 Sep 09  
Date

  
David J. Bunker, PhD (Member)


2 Oct 09  
Date

  
Richard K. Cohn, PhD (Member)

23 Sept 09  
Date

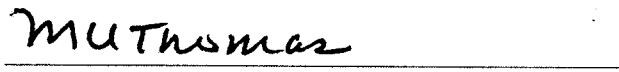
  
Robert B. Greendyke, PhD (Member)

30 Sept. 09  
Date

  
Paul I. King, PhD (Member)

30 Sept 09  
Date

Accepted:

  
M. U. Thomas  
Dean, Graduate School of  
Engineering and Management

26 Oct 09  
Date

*Abstract*

This study quantified the effects of discrete wall-based film cooling in a rocket with curved walls. Simulations and experiments showed decreasing with wall radius of curvature, holding jet diameter constant, improves net heat flux reduction (NHFR) and adiabatic effectiveness ( $\eta$ ) for 90° compound injected cylindrical jets, though  $\eta$  is reduced at the highest curvature. NHFR and  $\eta$  improved further with a high favorable stream-wise pressure gradient ( $K=2.1 \times 10^{-5}$ ) at all tested blowing ratios, but were affected little by a high density ratio ( $DR=1.76$ ) using carbon dioxide as the coolant. Experiments were run at a Reynolds number of 31K and a free-stream turbulence intensity of 26% with varying wall and jet radii. Simulations showed the Rannie transpiration model may be used to predict the cooling performance of a wall with full coverage film cooling using a correction formula based on the hole coverage area. Three improvements were made to the method of simultaneous acquisition of adiabatic wall temperature and heat flux coefficient: solving for the needed variables via a multi-point non-linear least squares curve fit instead of a two-point direct solution; correctly applying the free-stream fluid temperature boundary condition to account for drifting temperature instead of assuming it to be constant; and showing a repeatable way to reduce uncertainty in the test start time.

## *Acknowledgements*

Many good people helped me with this project in some way, but the following people have really been the bumpers on my dissertation bowling lane. Success was possible only with guidance and wisdom from my adviser and mentor Lt Col Rich Branam. I learned much from him and am indebted to him for the success of this publication and the growth of my professional character. To the other members of my committee I owe thanks for the honest, precise, and well-thought-out feedback and direction they provided. Thanks also to everyone who assisted with the setup of successful experiments, including but not limited to John Hixenbaugh, Dan Ryan, and Jake Schmidt. Jay Rutledge, Dan Karrels, and Dave Evans are owed a special thanks for insight, camaraderie, and helping me develop ideas which, ultimately, culminated in this work. I'd also like to thank Dr. William Baker and Dr. Mark Polanka for their guidance in finalizing this document.

Jonathan Floyd McCall, P.E.

# *Table of Contents*

	Page
Abstract . . . . .	iv
Acknowledgements . . . . .	v
List of Figures . . . . .	viii
List of Tables . . . . .	xiii
List of Symbols . . . . .	xiv
List of Abbreviations . . . . .	xvi
 I. Thermal Requirements for Increased Rocket Performance . . . . .	 1
1.1 Definition of Effusion Cooling . . . . .	2
1.2 Research Purpose . . . . .	5
 II. Current Effusion Cooling Models . . . . .	 7
2.1 Key Parameters . . . . .	9
2.2 Implementation in Rockets . . . . .	16
2.3 Spalding's Formulation . . . . .	22
2.4 Empirical Correlations of Cooling Effectiveness . . . . .	24
2.5 Pressure Gradient Effects . . . . .	26
2.6 Flowfield Dependence . . . . .	29
2.7 Summary . . . . .	37
 III. Computational Performance Prediction . . . . .	 38
3.1 Transpiration vs FCFC . . . . .	38
3.2 Simulations of Curved Geometry . . . . .	45
3.3 Results of Radial Concave Curvature Simulations . . . . .	50
3.4 Summary . . . . .	59
 IV. Experimental Method to Determine Effects of Radial Curvature . . . . .	 60
4.1 Simultaneous Acquisition of $T_{aw}$ and $h$ . . . . .	60
4.2 Design of Experiments Methodology . . . . .	62
4.3 Test Rig Design . . . . .	67
4.4 Improvements to the Transient Technique . . . . .	72
4.5 Experimental Procedure . . . . .	76
4.6 Analysis of Experimental Uncertainty . . . . .	78

	Page
V. Inert Gas Experiment Results . . . . .	87
5.1 Curvature Effects . . . . .	88
5.2 Stream-wise Pressure Gradient Effects . . . . .	96
5.3 Density Ratio Effects . . . . .	98
5.4 Interactions Between Variables . . . . .	103
5.5 Zero Compound Injection Angle Results . . . . .	105
5.6 Heat Flux Reduction Effects . . . . .	114
5.7 Comparison to Simulation . . . . .	119
5.8 Summary . . . . .	120
VI. Conclusions and Future Work . . . . .	122
6.1 Summary of Work Accomplished . . . . .	123
6.2 Transient Technique Lessons Learned . . . . .	124
6.3 Future Work in Film Cooling/Curvature . . . . .	126
Appendix A. . . . .	128
A.1 Properties of Polyurethane foam . . . . .	128
A.2 Hotwire Anemometry Measurements of Turbulent Intensity . . . . .	129
A.3 Infrared Thermography System . . . . .	134
A.4 Repeatability of Transient Technique . . . . .	136
A.5 Figures of pressure gradient Comparisons . . . . .	137
A.6 Figures of Density Ratio Comparisons . . . . .	142
A.7 Figures of Zero Compound Injection Angle Comparisons . . . . .	147
A.8 Figures of $D_\infty/D_j = 64$ . . . . .	151
Bibliography . . . . .	153
Vita . . . . .	159



## *List of Figures*

Figure		Page
1.	Film cooling vs. transpiration cooling. . . . .	3
2.	Injection angle definitions. . . . .	15
3.	Definition of stream-wise (axial) and span-wise (radial) curvature. . . . .	15
4.	Heat flux ratio as a function of blowing ratio . . . . .	18
5.	Strong favorable stream-wise pressure gradient inducing flow acceleration. . . . .	27
6.	$\zeta/\eta_t$ results of area comparison . . . . .	44
7.	Contour plots of adiabatic effectiveness, $F = 0.5$ . . . . .	51
8.	Simulation of $\eta_{\overline{span}}$ for $\alpha = 90^\circ$ . . . . .	52
9.	Span-wise averaged adiabatic effectiveness for $90^\circ$ compound injection at a variety of $C$ values . . . . .	52
10.	Simulation of $\eta_{\overline{span}}$ for $\alpha = 0^\circ, 45^\circ$ . . . . .	53
11.	Comparison of jet widths for $90^\circ$ compound injection at a variety of $C$ values. . . . .	54
12.	Comparison of net heat flux reduction (NHFR) for all three $D_\infty/D_j$ values at the tested blowing ratios . . . . .	56
13.	Contour plots of NHFR for the $90^\circ$ compound injection angle cases at blowing ratio of $F = 0.5$ . . . . .	57
14.	Contour plots of NHFR for the $90^\circ$ compound injection angle cases at blowing ratio of $F = 0.7$ . . . . .	57
15.	Contour plots of NHFR for the $90^\circ$ compound injection angle cases at blowing ratio of $F = 1.0$ . . . . .	58
16.	Contour plots of NHFR for the $90^\circ$ compound injection angle cases at blowing ratio of $F = 1.25$ . . . . .	58
17.	Contour plots of NHFR for the $90^\circ$ compound injection angle cases at blowing ratio of $F = 1.50$ . . . . .	58
18.	Transient heating process on a semi-infinite slab. . . . .	62

Figure		Page
19.	Physical testing apparatus . . . . .	68
20.	Conceptual drawing of plenum construction. . . . .	70
21.	Comparison of 2-point and $n$ -point Correlations . . . . .	73
22.	Coolant temperature drift effect . . . . .	74
23.	Example of time error histogram . . . . .	76
24.	Adjacent pixels undergoing transient convective heating. . . . .	84
25.	Area averaged adiabatic effectiveness vs. blowing ratio. . . . .	89
26.	New curvature parameter . . . . .	91
27.	$\eta$ vs. $x/D_j$ at different blowing ratios . . . . .	94
28.	$\eta$ vs. $x/D_j$ at different radial curvatures . . . . .	95
29.	New curvature parameter with strong favorable pressure gradient	97
30.	Area-averaged adiabatic effectiveness vs. blowing ratio with strong pressure gradient. . . . .	97
31.	$\eta$ vs. $x/D_j$ for at the same radial curvatures with strong $dp/dx$	99
32.	New curvature parameter with high density ratio . . . . .	100
33.	Area-averaged adiabatic effectiveness vs. blowing ratio with high density ratio. . . . .	101
34.	$\eta$ vs. $x/D_j$ for at the same radial curvatures with high $DR$ . .	102
35.	New curvature parameter including all tested phenomena . . .	104
36.	New curvature parameter, $\alpha = 0^\circ$ . . . . .	106
37.	Area-averaged adiabatic effectiveness vs. blowing ratio, $\alpha = 0^\circ$ .	107
38.	$\eta$ vs. $x/D_j$ for different radial curvatures, $\alpha = 0^\circ$ . . . . .	108
39.	$\eta$ vs. $x/D_j$ for at the same radial curvatures, $\alpha = 0^\circ$ . . . . .	109
40.	New curvature parameter with strong favorable pressure gradient, $\alpha = 0^\circ$ . . . . .	110
41.	Area-averaged adiabatic effectiveness vs. blowing ratio with strong pressure gradient, $\alpha = 0^\circ$ . . . . .	111
42.	$\eta$ vs. $x/D_j$ for at the same radial curvatures with $dp/dx$ , $\alpha = 0^\circ$	111
43.	New curvature parameter with high density ratio, $\alpha = 0^\circ$ . . .	112

Figure		Page
44.	Area-averaged adiabatic effectiveness vs. blowing ratio with high density ratio, $\alpha = 0^\circ$ . . . . .	113
45.	Area-averaged NHFR vs. blowing ratio, $\alpha = 90^\circ$ . . . . .	116
46.	Area-averaged NHFR vs. blowing ratio, $\alpha = 0^\circ$ . . . . .	116
47.	Area-averaged NHFR vs. blowing ratio with strong favorable stream-wise pressure gradient . . . . .	117
48.	Area-averaged NHFR vs. blowing ratio with high density ratio	118
49.	Comparison of experimental data to simulation . . . . .	119
50.	Hotwire data for the zero pressure gradient configuration, 9.25 <i>cm</i> from the wall, 3 <i>cm</i> upstream of the hole. . . . .	130
51.	Hotwire data for the favorable pressure gradient configuration, 9.25 <i>cm</i> from the wall, 3 <i>cm</i> upstream of the hole. . . . .	130
52.	Power spectral density for the favorable pressure gradient configuration, 8 <i>cm</i> from the wall, 3 <i>cm</i> upstream of the hole. . . .	131
53.	Power spectral density for the favorable pressure gradient configuration, 9.25 <i>cm</i> from the wall, 3 <i>cm</i> upstream of the hole. .	131
54.	Power spectral density for the favorable pressure gradient configuration, 10.5 <i>cm</i> from the wall, 3 <i>cm</i> upstream of the hole. .	132
55.	Power spectral density for the zero pressure gradient configuration, 8 <i>cm</i> from the wall, 3 <i>cm</i> upstream of the hole. . . . .	132
56.	Power spectral density for the zero pressure gradient configuration, 9.25 <i>cm</i> from the wall, 3 <i>cm</i> upstream of the hole. . . . .	133
57.	Power spectral density for the zero pressure gradient configuration, 10.5 <i>cm</i> from the wall, 3 <i>cm</i> upstream of the hole. . . . .	133
58.	Infrared camera calibration curve . . . . .	135
59.	Results of repeatability tests . . . . .	136
60.	Effect of pressure gradient on adiabatic effectiveness, $F = 0.5$ , $\alpha = 90^\circ$ . . . . .	137
61.	Effect of pressure gradient on adiabatic effectiveness, $F = 0.7$ , $\alpha = 90^\circ$ . . . . .	138

Figure		Page
62.	Effect of pressure gradient on adiabatic effectiveness, $F = 1.0$ , $\alpha = 90^\circ$ . . . . .	139
63.	Effect of pressure gradient on adiabatic effectiveness, $F = 1.25$ , $\alpha = 90^\circ$ . . . . .	140
64.	Effect of pressure gradient on adiabatic effectiveness, $F = 1.50$ , $\alpha = 90^\circ$ . . . . .	141
65.	Effect of high density ratio on adiabatic effectiveness, $F = 0.5$ , $\alpha = 90^\circ$ . . . . .	142
66.	Effect of high density ratio on adiabatic effectiveness, $F = 0.7$ , $\alpha = 90^\circ$ . . . . .	143
67.	Effect of high density ratio on adiabatic effectiveness, $F = 1.0$ , $\alpha = 90^\circ$ . . . . .	144
68.	Effect of high density ratio on adiabatic effectiveness, $F = 1.25$ , $\alpha = 90^\circ$ . . . . .	145
69.	Effect of high density ratio on adiabatic effectiveness, $F = 1.50$ , $\alpha = 90^\circ$ . . . . .	146
70.	Effect of pressure gradient on adiabatic effectiveness, $F = 0.5$ , $\alpha = 0^\circ$ . . . . .	147
71.	Effect of pressure gradient on adiabatic effectiveness, $F = 0.7$ , $\alpha = 0^\circ$ . . . . .	147
72.	Effect of pressure gradient on adiabatic effectiveness, $F = 1.0$ , $\alpha = 0^\circ$ . . . . .	148
73.	Effect of pressure gradient on adiabatic effectiveness, $F = 1.25$ , $\alpha = 0^\circ$ . . . . .	148
74.	Effect of pressure gradient on adiabatic effectiveness, $F = 1.50$ , $\alpha = 0^\circ$ . . . . .	148
75.	Effect of high density ratio on adiabatic effectiveness, $F = 0.5$ , $\alpha = 0^\circ$ . . . . .	149
76.	Effect of high density ratio on adiabatic effectiveness, $F = 0.7$ , $\alpha = 0^\circ$ . . . . .	149
77.	Effect of high density ratio on adiabatic effectiveness, $F = 1.0$ , $\alpha = 0^\circ$ . . . . .	149

Figure		Page
78.	Effect of high density ratio on adiabatic effectiveness, $F = 1.25$ , $\alpha = 0^\circ$ . . . . .	150
79.	Effect of high density ratio on adiabatic effectiveness, $F = 1.50$ , $\alpha = 0^\circ$ . . . . .	150
80.	Adiabatic effectiveness for $D_\infty/D_j = 64$ . . . . .	151
81.	Adiabatic effectiveness with strong favorable pressure gradient for $D_\infty/D_j = 64$ . . . . .	152
82.	Adiabatic effectiveness with high density ratio for $D_\infty/D_j = 64$	152

# *List of Tables*

Table		Page
1.	Results of $\zeta$ and Error For P/d Values Tested in full-coverage film cooling (FCFC) Study . . . . .	44
2.	Radial Curvature Parameter $C$ Values Used in $\eta_f$ Simulations .	47
3.	Closure Coefficients Used In The <i>Realizable</i> $k - \epsilon$ Model . . . .	50
4.	Matrix Of Tests To Be Performed . . . . .	78
5.	Absolute Errors of Measured Quantities . . . . .	79
6.	Summary of Fit Coefficients for Experimental Data . . . . .	121
7.	Properties of Polyurethane Foam . . . . .	128
8.	Turbulence Statistical Properties from Hotwire Tests . . . . .	129

## *List of Symbols*

### *English letter symbols*

$B$	driving force
$B_h$	blowing parameter (often $F$ is used)
$c_f$	skin friction coefficient
$c_p$	specific heat capacity at constant pressure, J/(kg*K)
$D, d$	hole diameter, m
$F$	blowing ratio, same as $B_h$ in many cases
$G$	mass flux, kg/(m <sup>2</sup> *s)
$g$	mass transfer conductance, kg/(m <sup>2</sup> s)
$h$	convective heat conductance, W/(m <sup>2</sup> K)
$I$	momentum ratio
$i$	specific enthalpy, J/kg
$K$	permeability; dimensionless pressure gradient severity
$k$	thermal conductivity, W/(m*K)
$L$	characteristic length, m
$\mathcal{M}$	molecular weight, kg/kmol
$O/F$	oxidizer to fuel ratio
$P$	hole pitch, or spacing
$\dot{q}''$	heat flux, W/(m <sup>2</sup> )
$R$	radial distance from surface, m; Rannie temperature difference factor
$r$	hole radius, m
$Sp$	Spalding function
$S$	surface area, m <sup>2</sup>
$s$	slot width, m
$T$	temperature, K
$Tu$	turbulent intensity
$u, v$	velocity, m/s
$x, y, z$	distance along or into surface, m

### *Greek letter symbols*

$\alpha$	molecular thermal diffusivity, m <sup>2</sup> /s; compound injection angle
$\beta$	ratio of occluded area to total flow area
$\varepsilon$	expansion ratio between rocket exit area and throat area
$\eta$	cooling efficiency; adiabatic effectiveness
$\gamma$	isentropic exponent
$\Lambda$	integral length scale, mm
$\mu$	dynamic viscosity coefficient, N*s/m <sup>2</sup>
$\nu$	kinematic viscosity, m <sup>2</sup> /s
$P$	ratio of radii
$\phi$	overall effectiveness for film cooling
$\rho$	density, kg/m <sup>3</sup>

$\tau$	shear stress, N/m <sup>2</sup>
$\xi, \gamma$	length for area-averaging, m
$\zeta$	area-average adiabatic effectiveness

*Superscripts*

$\overline{()}$	average
$()'$	fluctuating component
$()''$	per unit area, flux
$()\dot{}$	per unit time, rate
$()^+$	dimensionless wall coordinates

*Subscripts*

$\infty$	free-stream conditions
$aw$	adiabatic wall temperature of the gas
$c$	coolant
$crit$	critical
$f$	film cooling
$i$	initial
$o$	non-cooled condition
$rms$	root mean square
$S$	surface conditions
$span$	in the span-wise direction
$t$	transpiration; turbulent



## *List of Abbreviations*

1-D	one-dimensional
2-D	two-dimensional
ARES	the Advanced Rocket Engine System
AFIT	the Air Force Institute of Technology
AFRL	the Air Force Research Laboratory
C/C	carbon/carbon
CARS	Coherent Anti-Stokes Raman Spectroscopy
CFD	Computational Fluid Dynamics
CMCs	Ceramic Matrix Composites
COAL	Combustion Optimization and Analysis Laboratory
DLR	the German Aerospace Center
DNS	Direct Numerical Simulation
DOE	design of experiments
DR	density ratio
FCFC	full-coverage film cooling
IR	infrared
LES	Large Eddy Simulation
NASA	the National Aeronautics and Space Administration
Nd:YAG	Neodymium-doped Yttrium Aluminum Garnet
NHFR	net heat flux reduction
O/F	oxidizer to fuel ratio
PIV	Particle Image Velocimetry
PLIF	Planar Laser-Induced Fluorescence
TDK	Two Dimensional Kinetics
UCC	Ultra Compact Combustor
$I_{sp}$	specific impulse
$c_f$	skin friction coefficient
$Bi$	Biot number
$Nu$	Nusselt number
$Pe$	Péclet number

$Pr$	Prandtl number
$Pr_t$	turbulent Prandtl number
$St$	Stanton number
$Re$	Reynolds number

# DISCRETE FILM COOLING IN A ROCKET WITH CURVED WALLS

## I. Thermal Requirements for Increased Rocket Performance

Ever since the first liquid fueled rockets were launched by Robert Goddard in 1926 [1], they have been the workhorses of astronautical and aerospace propulsion. Liquid fueled rockets are essential to spacecraft launch and orbital maneuvering since they generally have very high specific impulse ( $I_{sp}$ ) compared to solid- or monopropellant-fueled thrusters, and a high thrust compared to electric propulsion devices; therefore, steadily searching for ways to extract more powerful and efficient performance out of these engines is of critical importance to future space launch capability. There are several ways to improve rocket thrust and  $I_{sp}$ . One is to increase the expansion ratio,  $\varepsilon$ , by contracting the throat.

Of course, changing one operating condition in a system usually affects all others. The effects of a smaller throat are increased chamber pressure (which raises the combustion temperature) for a fixed mass flow rate. One drawback of increased chamber pressure and temperature is increased heat transferred to the chamber and nozzle wall. In general, the wall would melt or sublime quickly under the thermal and mechanical loads of a combustion chamber were it not actively cooled. Therefore, the problem of cooling the nozzle wall ultimately limits the chamber pressures and temperatures attainable with current technology. Presently, high-thrust engines employ regenerative cooling to limit the wall temperature, requiring very high-pressure pumps and hundreds of small cooling channels to function. [1] The pressure loss associated with the torturous paths in these cooling channels, coupled with substantially higher chamber pressures, puts a prohibitively high requirement on pump outlet pressures. Hence, researchers are actively seeking more efficient methods of wall cooling.

### 1.1 *Definition of Effusion Cooling*

One effective method of supplementing regenerative cooling is known as effusion cooling. Effusion cooling uses cool fluid to create a cool fluid region between hot free-stream gasses and the wall. There are currently two types of effusion cooling: film cooling and transpiration cooling. In rockets, film cooling can be further divided into injector-based and wall-based cooling (see Fig. 1). Here, care must be taken to prevent nomenclature confusion between those familiar with turbines and rockets. Film cooling is frequently employed in gas turbine engines, but is analogous to wall-based film cooling in rockets. However, in rockets it is much more common to have injector-based film cooling, though the current trend is shifting towards the more efficient wall-based film cooling near the throat. Thus it is important to specify whether film cooling is wall-based or injector-based.

Most large rocket engines use injector film cooling. The injector is designed to deliver combustible mixtures of fuel and oxidizer away from the wall and nearly pure un-combusted fuel near the wall. This annulus of cold fuel travels along the combustion chamber wall keeping the wall cool (see Fig. 1). It gradually mixes with the oxidizer present in the core flow and is partly combusted by the time the mixture reaches the throat. When combined with regenerative cooling, injector film cooling is an effective and efficient way of cooling the combustion chamber walls. The throat region, the region with the highest heat flux, does not benefit as much from this type of cooling since the fuel has mostly combusted by the time the coolant reaches the throat.

*Transpiration Cooling.* Transpiration cooling occurs when high pressure coolant is forced through a porous wall, as in Fig. 1. The boundary layer thickness increases and the heat flux into the wall thereby decreases. Currently, the most effective way to implement this cooling method is to fix a porous liner of varying thickness beginning in the converging section of the chamber and ending a bit after the throat. This provides maximum cooling effectiveness in an area where it is difficult for regenerative cooling

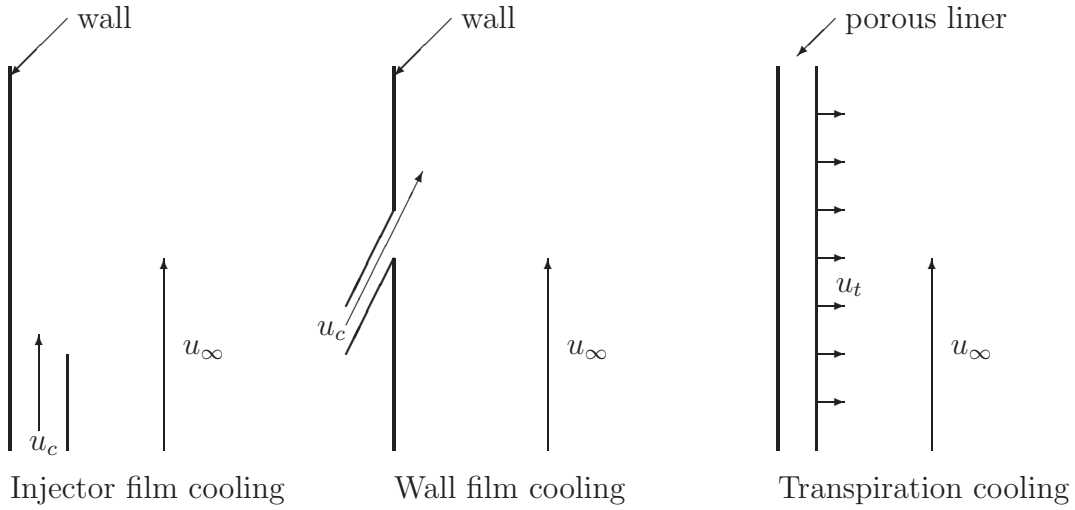


Figure 1: Film cooling vs. transpiration cooling. Free-stream flow is labeled  $u_\infty$ . Film coolant flow is labeled  $u_c$ . Transpiration coolant flow is labeled  $u_t$ .

to succeed. Transpiration has been empirically and analytically shown to decrease wall temperatures and thus increase material survivability. Indeed, it may be the most efficient method of cooling a hot wall by injection [2]. Practical implementation of transpiration cooling is limited by barriers such as structural limitations of the porous liner and an inability to effectively distribute the coolant in areas of the highest heat flux [3]. Current thermal protection systems researchers and designers are well aware of these difficulties in implementing true transpiration cooling in a rocket.

Many of the transpiration cooling models explained in Chap. II assume the coolant does not react with the free stream flow, and few account for diffusion effects. Of most importance to rocket applications is the effect of transpiration cooling on nozzle performance when compared to other cooling schemes, specifically regenerative cooling alone. Determining precisely how the coolant disperses through the free stream flow, especially while it is accelerated in the throat, and how it reacts chemically is imperative to predicting performance gains or losses from this type of cooling.

*Film Cooling.* Another way to implement effusion cooling is with wall film cooling. Several holes are placed in a solid wall, which increases structural strength over the porous liner while still cooling the wall by injection, as in Fig. 1. This method of cooling is difficult to implement practically in rockets, since small closely-spaced holes are desired for maximum cooling efficiency, which is a major manufacturing challenge. A new method of manufacturing using diffusion bonded and formed platelets has helped to bridge the gap between theory and practice [4]. These chamber cooling schemes are now being aggressively scrutinized for application to rockets.

Film cooling in gas turbine engines has been researched for several decades, and a good understanding of the phenomenon is beginning to take shape. The research shows the most significant parameter is blowing ratio (the ratio of coolant mass flux to free-stream mass flux) [5]. Choosing a blowing ratio results in a certain cooling effectiveness characterized by the non-dimensional wall temperature surrounding the hole. Several other factors, such as injection angle, turbulent intensity, surface roughness, surface geometry, hole shape, rotation, and stream-wise pressure gradients have also been studied [5]. In turbine engines, relatively cool air (compared to rocket combustion temperatures) is the chief component of both the free-stream and coolant gasses, so some parameters specific to rockets have not been heavily researched. The most important of these differences include high density ratio ( $\gg 2$ ), steep favorable pressure gradients, specific heat differences between free-stream and coolant gasses, radial curvature effects, and the combustion of coolant downstream of the injection point. All of these phenomena are discussed in more detail in Chap. II

Most film cooling research for turbine applications has been performed using flat plates or surfaces with stream-wise curvature. Rocket combustion chambers not only experience stream-wise curvature near the throat, but axisymmetric rockets also have walls with radial curvature. Radial curvature effects on film cooling performance have never been investigated until now. These effects are documented here.

## ***1.2 Research Purpose***

The purpose of this research was to determine how a radially-curved wall affects film cooling performance under rocket-like conditions, the results of which will provide new understanding and data to thermal protection systems designers regarding performance in rocket-specific environments. This was accomplished via three experimental goals:

1. to determine the change in cooling adiabatic effectiveness by varying the wall curvature radius and compound injection angle out of a radially curved surface over a range of blowing ratios;
2. to determine the effect of a high favorable pressure gradient on cooling adiabatic effectiveness over a range of blowing ratios and determine what new pressure gradient related phenomena occur due to variations in compound injection angle and radial curvature;
3. to determine the effects of density ratio on film cooling adiabatic effectiveness on a radially curved wall.

This work documents the successful accomplishment of these goals. After a review of the fundamentals of effusion cooling and its application to rockets in Chap. II (p. 7), Chap. III (p. 38) documents three Computational Fluid Dynamics (CFD) studies which explored the relation between transpiration cooling and full coverage film cooling and predicted the effects of radial curvature on the effectiveness of effusion cooling in a typical rocket geometry. In Chap. IV (p. 60), a detailed description of the setup of the completed experiments is presented, including improvements to a transient technique for the simultaneous acquisition of surface temperature and heat flux. Chapter V (p. 87) will discuss the fulfillment of goals 1-3 in the course of these experiments. Finally, Chap. VI (p. 122) contains recommendations for future work on this topic, including suggestions for further improvement to the transient technique and other information to be gleaned from laser diagnostic work.

This research was fully funded and supported by AFRL/RZS at Edwards Air Force Base, California.



## II. Current Effusion Cooling Models

Wall injected film cooling has a promising application for future high-pressure rockets. Most past efforts have been focused on transpiration cooling of the rocket chamber walls, since film cooling was difficult to achieve from manufacturing capabilities. It is important to note transpiration cooling and film cooling describe a similar phenomenon. In a film cooled wall, discrete jets of coolant exit holes with constant diameters at a certain angle, and a certain hole spacing. As one makes the holes smaller, more numerous, and closer together, the behavior of the coolant jets begins to more closely resemble a transpiration cooling scheme. In a transpiration cooled wall, the coolant “jets” are so close together and so small that they now form a sheet. The porous wall generally does not have any injection angle since the exit angles are randomly distributed (diffuse) over the surface. So a film cooled wall will exhibit many characteristics of a transpiration cooled wall, though jet phenomena come into play.

While all of the current models are applicable over a limited range and fluid choice, there is some insight to be gained by observing the process of effusion cooling in its most basic elements. In rocket applications, the first desired condition is the temperature of the hot side of a porous wall remain below a reasonable operating temperature as determined by thermal and mechanical limits of the material. Second, the effused coolant mass flow rate must not be so high as to offset the benefits in performance (specific impulse ( $I_{sp}$ )) and thrust over other cooling schemes.<sup>1</sup>

Film cooling is the injection of coolant into a boundary layer via discrete holes. Many so-called transpiration cooled rocket chambers are actually film cooled, but previous research still provides useful information since film cooling can be approximated by the transpiration cooling equations when the film cooling holes are small in diameter and numerous in surface density. However, film cooling differs from transpiration cooling via the ability to choose the coolant injection angle. Further, as the cooling holes become larger and more discrete, an increase in blowing ratio tends to

---

<sup>1</sup>Regenerative cooling alone in particular.

behave more like a jet than a thickened boundary layer. An excellent and thorough examination of film cooling in its application to gas turbines has recently been presented by Bogard and Thole. [5] There are notable differences in rocket combustion chambers when compared to gas turbines: super-critical operating conditions, intense free-stream combustion and turbulence, relatively sharp radial concave curvature, a strong favorable axial pressure gradient, very high density ratios, specific heat capacity differences and combustion of the coolant in the wake. Still, much of gas turbine research is applicable to rocket combustion chambers.

Starting in the late 1940's, research into the practical applications of transpiration cooling was mostly analytical with few experiments. [6] Experimentation led to over a dozen models of mass and heat transfer, each one matching the respective data sets and different in their simplifying assumptions, boundary conditions, and final forms. By the mid 70's, analytical progress on this topic had mostly subsided, with interest to be renewed by the advent of new, high temperature porous materials, new manufacturing processes, and fast computers for numerical solutions. Thus, we find the current surge in transpiration cooling research, beginning around 1995, to be based mostly on empirical adjustments of the original mathematical relationships and one-dimensional (1-D) numerical simulations of the momentum and energy equations. It is important to remember transpiration cooling in rockets is in actuality some form of effusion cooling lying between transpiration and full coverage film cooling.

Any cooling scheme implemented in a rocket must improve the efficiency of the rocket over other available cooling schemes. Rocket efficiency may be measured in units of specific impulse, which is the ratio of rocket thrust to propellant mass. It is often given solely as a function of propellant, though in reality it is the efficiency by which a given rocket converts the chemical energy into thrust. It is defined as

$$I_{sp} = \frac{F}{\dot{m}g_0} \quad (1)$$

where  $F$  is the thrust,  $\dot{m}$  is the mass flow of propellant, and  $g_o$  is the gravitational constant  $9.807 \text{ m/s}^2$ . The equation for the thrust of a rocket is

$$F = \dot{m}v_e + (p_e - p_a)A_e \quad (2)$$

Clearly,  $I_{sp}$  is a function of the exit flow pressure  $p_e$ , the ambient pressure  $p_a$ , the gas exit velocity  $v_e$ , and nozzle exit area  $A_e$ . In general,  $I_{sp}$  can be calculated from

$$I_{sp} = \frac{1}{g_o} \left[ v_e + \frac{A_e}{\dot{m}}(p_e - p_a) \right] \quad (3)$$

where  $v_e$  is

$$v_e = \sqrt{\frac{2\gamma}{\gamma - 1} \frac{\mathcal{R}_u T_o}{\mathcal{M}} \left\{ 1 - \left( \frac{p_e}{p_o} \right)^{\frac{\gamma-1}{\gamma}} \right\}} \quad (4)$$

For a given rocket with a bulk chamber temperature  $T_o$  and pressure  $p_o$ , and combustion gas with bulk molecular weight  $\mathcal{M}$  and isentropic exponent  $\gamma$ , the specific impulse can be calculated using Eqs. 3 and 4. Film cooling affects specific impulse by changing the bulk molecular weight of the exhaust gases and the exit temperature. While the exit temperature does not explicitly appear in Eq. 4, the chamber temperature  $T_o$  does. Exit temperature is assumed to be purely a function of rocket geometry after the chamber, a result of the adiabatic process assumption. If coolant is injected into the combustion gas after the chamber, the *effective*  $p_o$ ,  $T_o$ , and  $\mathcal{M}$  are changed.

## 2.1 Key Parameters

The key parameters related to transpiring through a porous medium most affecting the heat and mass transfer rates are the wall permeability and porosity, wall thickness, coolant manifold pressure and temperature, chamber gas pressure and temperature (results of the overall system design), and material choices for the coolant and the porous wall. For the wall, these choices will be dependent on the required con-

ductivity, density, and specific heat capacity. For the coolant, viscosity is important for the desired wall temperature. The coolant mass flow rate and material porosity combine in some form to create the blowing ratio, which in most transpiration cooling models is based on relative mass flux.

Many dimensionless parameters are used in these models. What follows is a brief description of each.

Reynolds number: The ratio of inertial to viscous forces in a moving fluid. It is useful in determining if two fluids flowing in geometrically similar conditions are also dynamically similar. When multiplied by the Prandtl number ( $Pr$ ), a result (the Péclet number ( $Pe$ )) greater than 5 indicates axial conduction effects in a fluid flowing through a pipe may be neglected.

$$Re = \frac{\rho u L}{\mu} = \frac{GL}{\mu} = \frac{uL}{\nu} \quad (5)$$

Prandtl number: The ratio of kinematic to thermal diffusiveness in a fluid. It indicates the relative quickness a momentum effect will diffuse through a fluid with respect to a thermal effect at the same location. A  $Pr$  less than one means a temperature boundary layer will develop more rapidly than a velocity boundary layer. Most gases have a  $Pr$  approximately equal to or slightly less than unity.

$$Pr = \frac{c_p \mu}{k} = \frac{\nu}{\alpha} \quad (6)$$

Nusselt number: The ratio of convective conductance in a fluid to thermal conductivity of the fluid along an adjacent wall. It is the temperature boundary layer analog of skin friction coefficient for velocity boundary layers, and thus is a constant for developed internal laminar flow. Turbulent flows require empirical relationships to determine local values of the Nusselt number ( $Nu$ ) along a wall.

$$Nu = \frac{hL}{k}, h = h(Re, Pr, \text{geometry}) \quad (7)$$

Stanton number: The ratio of convective heat flow in a fluid to the fluid mass flux and specific heat. If there exists flow over a flat plate with constant pressure and free-stream velocity, constant properties, and a constant fluid-surface temperature difference, the Stanton number ( $St$ ) number will be exactly equal to the change in the enthalpy thickness of the thermal boundary layer with respect to length of plate traveled ( $d\Delta_i/dx$ ). Also defined as the ratio of heat transfer perpendicular to a wall/fluid interface to the heat transfer parallel to the interface.

$$St = \frac{\dot{q}_s''}{\rho u_\infty c_p (T_s - T_\infty)} = \frac{h}{\rho u_\infty c_{p,\infty}} = \frac{h}{G_\infty c_{p,\infty}} \quad (8)$$

Skin friction coefficient: Skin friction is the relative rate a fluid's momentum is dissipated to a wall. The Reynolds analogy implies skin friction coefficient ( $c_f$ ) is nearly equal to twice the  $St$  number. Though this approximation is not correct for highly turbulent flows, it is used nonetheless in several models. For turbulent flows,  $c_f$  decreases with increasing Mach number.

$$\frac{c_f}{2} = \frac{\tau_w}{\rho u_\infty^2} = \mu \left. \frac{\partial u}{\partial y} \right|_w \frac{1}{\rho u_\infty^2} \approx St \quad (9)$$

Blowing ratio: The ratio of the free-stream mass flux to the effusion cooling fluid mass flux. All heat and momentum transfer models are based in some way on the blowing ratio:

$$F = \frac{\rho_c v_c}{\rho_\infty u_\infty} \quad (10)$$

Density ratio: The ratio of the density of a coolant to the density of the free-stream flow. This is written:

$$DR = \frac{\rho_c}{\rho_\infty} \quad (11)$$

Momentum ratio: The ratio of the free-stream kinetic energy to the effusion cooling fluid kinetic energy:

$$I = \frac{\rho_c u_c^2}{\rho_\infty u_\infty^2} \quad (12)$$

Notice the blowing ratio and momentum ratio are related by the density ratio:

$$I * DR = F^2 \quad (13)$$

For  $DR = 1$ , the momentum ratio is simply the square of blowing ratio.

Cooling efficiency: The ratio of the heat flux of a wall cooled by effusion to the heat flux to the same wall without cooling. Usually this is expressed in terms of  $St$ :

$$\eta_t = \frac{St}{St_o} \quad (14)$$

though in film cooling models it is expressed in terms of temperature reduction:

$$\eta_f = \frac{T_\infty - T_{aw}}{T_\infty - T_c} \quad (15)$$

which is called the *adiabatic effectiveness*. In this document,  $\eta$  with no subscript is assumed to be this  $\eta_f$ . Adiabatic effectiveness is frequently span-wise averaged according to

$$\eta_{\overline{span}}(y) = \frac{1}{\xi_2 - \xi_1} \int_{-\xi_1}^{\xi_2} \eta_f \, dx \quad (16)$$

where  $\xi$  denotes the lateral distance between holes, and  $y$  is in the direction of bulk flow. Further, the *area averaged* adiabatic effectiveness is:

$$\zeta = \frac{1}{(\xi_2 - \xi_1)(\gamma_2 - \gamma_1)} \int_{-\xi_1}^{\xi_2} \int_{-\gamma_1}^{\gamma_2} \eta_f \, dx \, dy \quad (17)$$

The limits  $\xi$  and  $\gamma$  should be chosen in proportion to the hole spacing  $P$ , called the *pitch*, in the span-wise ( $x$ ) and stream-wise ( $y$ ) direction, respectively.

NHFR: The net heat flux reduction (NHFR) is the fractional decrease in heat flux to the wall from the same wall were there not a jet. NHFR is defined as

$$\text{NHFR} = 1 - \frac{\dot{q}_f''}{\dot{q}_o''} \quad (18)$$

where  $\dot{q}_o''$  is the heat flux to the wall without effusion cooling. By expanding the heat flux terms according to Newton's law of cooling, one may write

$$\text{NHFR} = 1 - \frac{h_f(T_{aw} - T_S)}{h_o(T_\infty - T_S)} \quad (19)$$

$$= 1 - \frac{h_f}{h_o} \left( \frac{T_{aw} - T_S}{T_\infty - T_S} \frac{T_\infty - T_c}{T_\infty - T_c} \right) \quad (20)$$

$$= 1 - \frac{h_f}{h_o} \left( \frac{T_\infty - T_S - T_\infty + T_{aw}}{T_\infty - T_c} \frac{T_\infty - T_c}{T_\infty - T_S} \right) \quad (21)$$

$$= 1 - \frac{h_f}{h_o} \left( \frac{T_\infty - T_S}{T_\infty - T_c} - \frac{T_\infty - T_{aw}}{T_\infty - T_c} \frac{T_\infty - T_c}{T_\infty - T_S} \right) \quad (22)$$

Remember the definition of  $\eta_f$  from Eq. 15 and define the *overall effectiveness*  $\phi$  as

$$\phi = \frac{T_\infty - T_S}{T_\infty - T_c} \quad (23)$$

One may now write NHFR as

$$\text{NHFR} = 1 - \frac{h_f}{h_o} \left( 1 - \frac{\eta_f}{\phi} \right) \quad (24)$$

It includes the overall effectiveness, which for rockets can range from 0.5 to 0.8 depending on coolant temperatures and wall material thermal limits. For gas turbines  $\phi$  is almost always assumed to be 0.6 [5].

Analytical transpiration cooling models attempt to correct the non-transpired convective heat transfer coefficient  $h$  (usually via  $St$  number or  $c_f$ ) with a parameter involving at least blowing ratio, and sometimes molecular weight or specific heat capacity ratios [7]. These corrections for wall blowing were derived for sub- or super-

sonic flow and moderate gas temperatures of less than 1000 K. A few models take into account foreign gas injection and thus diffusion [8]. For space applications, the limits of these relations are that they simply do not account for typical effects in rocket engines, such as dissociation and recombination, variable temperature dependent fluid properties, or injection of super-critical fluids [8]. Very little experimentation has been done accounting for these effects.

As Jeromin [9] points out, using a relative measure of heat transfer reduction (effectiveness) is a temporarily useful one and should be replaced when a theory of the turbulent transport mechanism is available. Currently, the Bartz equation [10] is standard for predicting heat transfer in rocket nozzles, though it admittedly has low accuracy ( $\pm 25\%$ ) in most applications. Obviously, a universal theory has not yet come to fruition.

*Injection Angles.* There are two angles which define the direction of a film cooling jet, shown in Fig. 2.  $\theta$  is called the injection angle, and  $\alpha$  the *compound* injection angle. They are defined in two different, orthogonal planes.  $\theta$  is the angle between the bulk coolant flow and free-stream flow vectors in the plane defined by the free-stream flow vector and the surface normal vector at the point of injection.  $\alpha$  is the angle between the bulk coolant flow and free-stream flow vectors in the plane *parallel* to the surface at the point of injection.

*Curvature Definitions.* Turbine blades are almost always curved in the stream-wise direction. This means as the flow travels in one direction, a nearby wall appears to either encroach upon or fall away from the flow. In a rocket, the walls are usually curved in the span-wise, or radial, direction and the stream-wise, or axial, direction. These two types of curvature are shown in Fig. 3. A summary of previous research on film cooling flows and stream-wise curvature begins on p. 26.



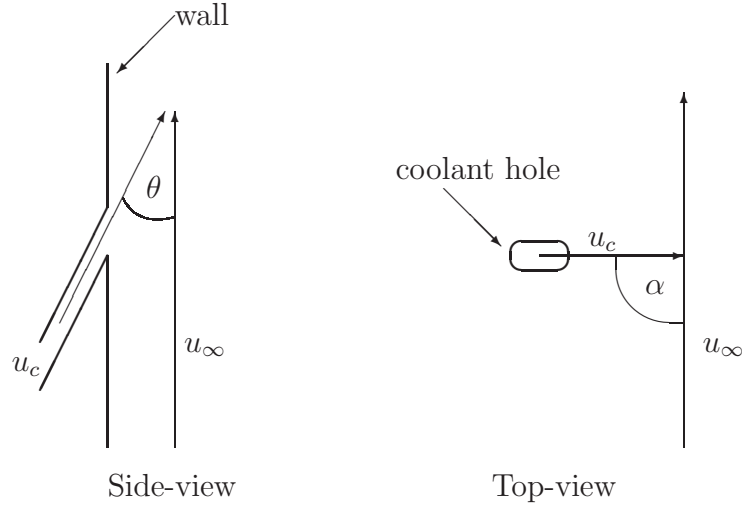


Figure 2: Definition of the injection angle  $\theta$  and the *compound* injection angle  $\alpha$ . Free-stream flow is labeled  $u_\infty$ . Film coolant flow is labeled  $u_c$ .

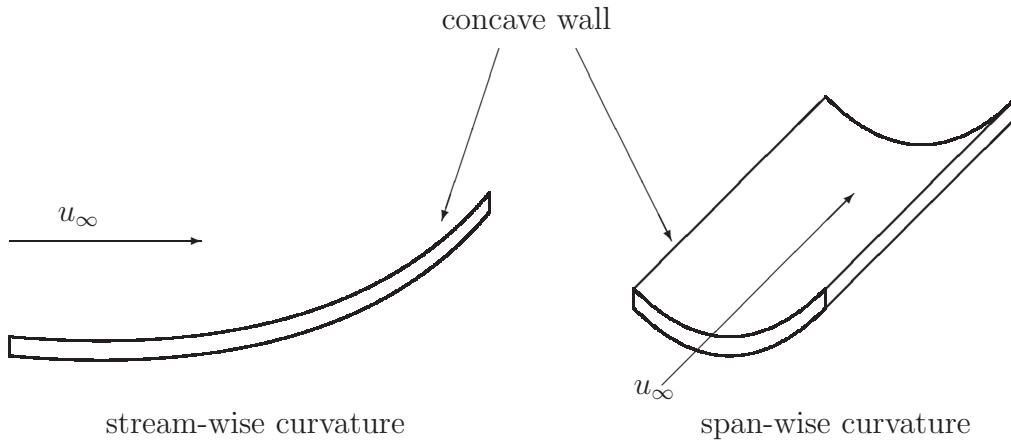


Figure 3: Definition of stream-wise (axial) and span-wise (radial) curvature. Free-stream flow is labeled  $u_\infty$ .

## 2.2 *Implementation in Rockets*

Aerojet first successfully demonstrated effusion cooling in a rocket engine in 1967 on the Advanced Rocket Engine System (ARES) 100,000 lbf thrust, 3000 psi engine [4]. They tested this engine, and performed much more work in this type of cooling over the next decades, using formed platelets. Though initially designed for use in regenerative cooling, formed platelets hold great appeal for transpiration applications because of their manufacturability, customizable channel configuration, and structural strength. This manufacturing process consists of taking several very thin sheets of metal, photo-etched in a specific pattern, chemically milled, and then stacked. After diffusion-bonding the plates together, the resultant micro channels, of literally any desired configuration, are then filled with coolant to keep the wall cool [4]. If the micro channels end in a coolant plenum, it is called regenerative cooling. If the micro channels place coolant in the chamber itself, it is called effusion cooling. This cooling method has already been successfully implemented on  $O_2/H_2$  injector face plates, and is currently being investigated for use with combustion chamber walls. [11]

Work on ARES eventually ceased, and later Lee and Burkhardt [4] attempted to determine the relationship between the key parameters in transpiration cooling and life enhancement of combustion chambers. Though they tested only at 1500 psi and one transpiration flow rate, the results were promising. By building and testing on three different methane and RP-1 fueled sub-scale nozzles, two of which employed transpiration cooling in the throat, they were able to determine transpiration cooling can be effective while only using 67% of the coolant the 1-D computational model predicted would be necessary. Furthermore, the  $I_{sp}$  was increased by 3 to 10 seconds over model predictions.

*Range of Performance Enhancement.* Several experiments were conducted at the Air Force Institute of Technology (AFIT) in the 1960's to determine what effect the blowing ratio has on heat flux. Weisinger [12] conducted some of the first exper-

iments with transpiration cooling a plate subjected to heating from hydrocarbon-air combustion. Using propane as fuel and room temperature air as coolant, he found the  $St$  number was reduced as the blowing ratio increased, but not precisely in the way the Kays-Crawford relation predicts (see Eq. 39, p. 29). He also correctly observed, by experimenting with zirconia and stainless steel flat plates, the wall material choice does not greatly affect the wall temperature (this was to be later proven by Landis [13]). However, the majority of the experimental and numerical work at AFIT was carried out 30 years later, beginning with efforts by Lenertz [14].

Though it is well known the blowing parameter  $B_h$  can be correlated to heat flux reduction, Lenertz determined a linear relationship between the two might be accurately used over a limited range, since the heat flux is mostly determined in the near-linear sub-layer. He conducted low blowing ratio experiments with air which showed a near-linear relationship between blowing ratio and heat transfer coefficient. This led to a heat transfer coefficient correction factor of:

$$\frac{h}{h_o} = (1 - 27.4 * F) \quad (25)$$

This relation was derived purely from experimental data, and is valid as an average correction over the entire transpiration cooled wall. The data was taken from experiments in a 2-D Mach 2 nozzle. The coolant was distributed equally along the chamber and throat wall in the axial direction. The linear behavior of the blowing ratio was restricted to low blowing ratios ( $F < 0.02$ ).

Chen [15] proposed from experimentation the following relation (using the same rig as Lenertz):

$$\frac{h}{h_o} = (1 - 38.0F) \quad (26)$$

$$0.0000 < F < 0.0117$$

The difference between his and Lenertz's constant (38.0 vs. 27.4) stems from Chen's coolant distribution. He concentrated more of the coolant at the hottest part of the

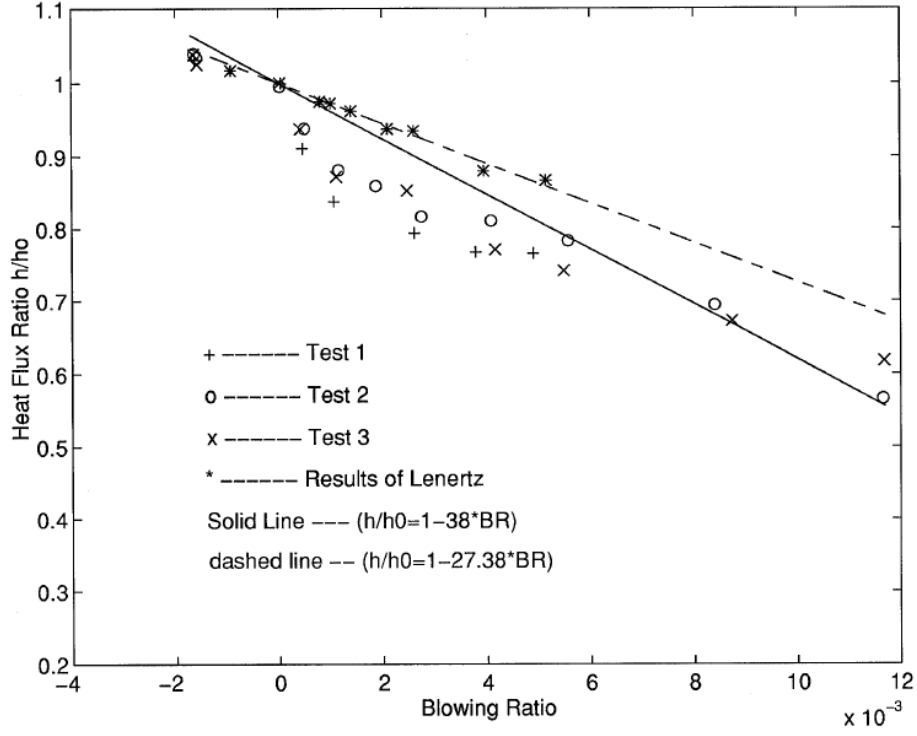


Figure 4: Heat flux ratio as a function of blowing ratio compared to Eqs. 25 and 26. [15]

throat, thus achieving a lower total heat transfer when averaged over the whole wall. Thus, an average or total heat transfer measurement is not appropriate to determine blowing ratio effects.

Chen [16] further pointed out there are both upper and lower limits of blowing ratio for the applicability of transpiration cooling when compared to regenerative cooling. The lower bound of blowing factor  $F$  occurs when the wall temperature is too hot for structural survivability. The upper bound occurs when the transpired mass flow is so high as to result in a negative performance impact, specifically on  $I_{sp}$ .

Landis [13] simulated a porous media as a bed of tightly packed spheres of specified diameter. His code simulated the interior of the porous wall, and set the heat flux as a boundary condition. This code was used to show the Space Shuttle main engine would benefit from transpiration cooling over regenerative cooling if the blowing ratio were  $0.004 < F < 0.007$  (via Chen's argument).

*Porous Walls.* Since transpiration cooling forces lower temperatures throughout the wall, very high temperature gradients occur on the hot side of the wall. Landis [17] thus suggested suitable materials for this cooling scheme, whether slotted or porous, must have a very high tolerance for thermal gradients, lest the material fracture under the thermal stresses. He also verified numerically the wall temperature is equal to the coolant temperature for all but an extremely thin section of the wall close to the hot gasses (and for configurations with very large porosities or hole sizes). Thus, the wall assumes the coolant temperature throughout almost all of its thickness.

Further investigations into transpiration cooling continued at AFIT, especially to evaluate its potential to replace regenerative cooling in liquid rockets. Bowman et al. [18] determined, for laminar flow, the inside temperature of a transpiration cooled wall was chiefly a function of the  $St$  number. Regenerative cooling yields a wall temperature dependent mostly on the Biot number ( $Bi$ ). Using fully developed flow in a porous-wall pipe,  $Nu$  comparisons were made between a numerical simulation and experimental Poiseuille flow for transpiration cooled pipes. These comparisons were validated by experiment, showing transpiration cooling and regenerative cooling are both useful options for rocket chamber walls. A decision on which method to use should depend on the relative magnitudes of  $Bi$  and  $St$ .

Computational researchers at the National Aeronautics and Space Administration (NASA) have attempted to characterize the effects of transpiration cooling on engine performance. A study by Kacynski and Hoffman [19] showed the prediction of thrust coefficient using the NASA code Proteus is quite accurate when compared to experimental data taken from a transpiration cooled spool and plug nozzle. The code includes mixing of free stream and injection gasses while modeling the pressure gradient seen in the converging section. The Soret mass transfer and Dufour heat transfer effects were included in the program, with the former contributing greatly to an accurate solution. The latter proved negligible in transpiration cooling applications.

Other NASA codes have been used for transpiration cooling for hypersonic vehicles. Glass et al. [20, 21] performed some 1-D computational analyses, the results of which echo the previous trends of blowing ratio vs. heat transfer reduction. They showed there exists a point of diminished returns for blowing ratio, past which no useful decrease in heat transfer is obtained. This was only an observation, and no method for predicting this point was given.

Using methane as the transpiration coolant and fuel, Bucchi, Bruno, and Congiunti [22] developed a 1-D model of transpiration through a porous wall. They implemented Landis' bed of packed spheres model. Porosity and permeability were related and they used the common  $Pr^{1/3}$  relation for effective hot gas temperatures at the wall ( $T_{aw}$ ). They used a relation developed at the German Aerospace Center (DLR) for cooling efficiency (see Eq. 48). No experiments were run to verify the model, but they made some very pertinent observations.

First, they showed a higher wall material thermal conductivity means less coolant mass flux is required for a given wall temperature, at the expense of a heavier porous wall. They showed the porosity of the wall material is a critical parameter; in their case a 2% change affected the required wall thickness by an order of magnitude. Also, separating the porous material axially into slices would prevent flow of the coolant towards the low pressure throat exit, thus distributing it evenly throughout the wall. They also pointed out a low coolant injection temperature may cause vaporization of the coolant in the porous channels, presenting structural problems.<sup>2</sup> Finally, cooling an entire engine with transpiration would result in too high a performance loss when compared to regenerative cooling. Cooling only the throat would provide the most benefit for a given performance impact.

Recently, Bai and Chung [23] at the University of Florida used Fluent<sup>®</sup> to determine the pressure drop through porous material as an aid in sizing transpiration cooled walls. Rather than using a bed of packed spheres, the metal foam micro-structure was

---

<sup>2</sup>This would not be as big a problem for super-critical fluids since they do not boil in the same way as non-super-critical fluids, though they do generally expand with temperature.

modeled as a network of thin beams. Using the fin heat transfer equation, the 1-D analytical model was compared against the FLUENT simulation and a simulation of regenerative cooling. Over twice the heat transfer rate was shown for the same pressure drop and mass flow in the transpired wall when compared to the regenerative cooled wall. This implies that a 50% reduction in pump power would be possible with transpiration cooling, lowering overall system mass and complexity. Further, the analytical model predicted heat fluxes about 30% higher than the FLUENT model predicted for transpiration cooling.

They also delved into which boundary conditions are appropriate for various Reynolds number ( $Re$ ) regimes. It was mentioned for  $Re < 10^5$ , the constant heat flux at the wall hot side should be used, while for  $Re > 10^5$  the constant wall temperature should be used. These choices were postulated earlier in theoretical detail [7], and Bai and Chung agreed since this method fit the FLUENT data well. It seems clear this observation highlights the effect of free stream conditions and blowing ratio on heat transfer and hot gas temperatures.

At the University of Michigan, Sozer and Shyy [24] predicted the fluid flow and heat transfer through a Rigimesh material. They volume-averaged the continuity, momentum, and energy equations and used Ergun's [25] equation to relate permeability to pressure drop:

$$-\partial_i p = \frac{\mu}{K} u_{Di} + \frac{C_E}{\sqrt{K}} \rho |u_{Di}| u_{Di} \quad (27)$$

Several closure coefficients, which should be determined experimentally, were required to solve the new equations. Thus, this method of solving fluid flow through the porous medium could be used with very little increase in computational resources.

*Film Cooling Hole Geometry.* In film cooling, the hole geometry has a great effect on adiabatic effectiveness,  $\eta_f$ , through injection angle, hole shape, and hole configuration. Generally, the shallower the injection angle, the better. The coolant tends to stay attached to the wall further downstream if the normal velocity is very small. Manufacturing and structural limits keep the injection angle to no less than

about  $30^\circ$ . If the hole fans out toward the exit so the coolant expands, the coolant will exit at a lower momentum, allowing the jet to better stick to the wall. Coolant is distributed more evenly if the coolant hole spacing, or pitch  $P$ , is small. As the jets get close together the flow behaves more like transpiration cooling than film cooling. In general, if  $P/d$  ( $d$  is hole diameter) is less than 1.5, the coolant jets will combine to form a continuous film, like in transpiration cooling [26]. Cooling efficiency also increases at higher blowing ratios if multiple rows of holes are used. In combustor cooling for 4-8 rows of holes the cooling effectiveness reached a maximum of  $\eta_f = 0.30$  with heat flux to the wall decreasing by 35-40% [27, 28].

### ***2.3 Spalding's Formulation***

Most of the transpiration cooling models presented in this chapter were derived from Spalding's theoretical formulation in 1960. Some empirical models were known to Spalding [29] when he made use of the "flux resistance" (Ohm's) models used several times before his research in different forms. He used this information to present his work in deriving a general method of solving steady mass and heat transfer problems. His method is ideally not limited by chemically reacting flows, turbulence, or pressure gradients, but is conceptually simple and not entirely accurate for turbulent flows or flows where  $Pr$  is far from one.

Spalding determined mass flux across any boundary, be it a phase boundary or wall, can be represented by a dimensionless driving force  $B$  and a surface conductance  $g$ :

$$\dot{m}'' = gB \quad (28)$$

By separating the two physical phenomena in this way, he lumped all of the aerodynamic factors affecting heat transfer and momentum into  $g$  and all of the thermodynamic factors into  $B$ . He noted this separation was not completely possible in the boundary layer. Nonetheless, he then went on to describe analytically several relationships for  $B$  and  $g$  based on simplifying assumptions for a given problem. At



the time, a formula for mass transfer through turbulent boundary layers was not fully developed, though the problem was being actively pursued by many. Still, he presented his formulation as:

$$\frac{g}{G_\infty} = 0.0365 \left[ \frac{\ln(1+B)}{B} \right] \left[ \frac{\mu R^{5/4}}{\int_0^x R^{5/4} G_\infty dx} \right]^{1/5} \quad (29)$$

He also treated the case of a transpired turbulent boundary layer specifically. He stated the specific heat transfer simply equals

$$Q = \dot{q}''/\dot{m}'' = c_{p,c}(T_s - T_\infty) \quad (30)$$

and consequently the driving force is

$$B = \frac{c_{p,\infty}(T_\infty - T_s)}{c_{p,c}(T_s - T_c)} \quad (31)$$

Eqs. 29 and 31 may be used to describe the mass flux through a turbulent boundary layer with transpiration.

Spalding [30,31] also developed a theory for the solution of heat transfer problems for similar cases. He introduced a function which allows one to determine the Stanton number ( $St$ ) based on a new parameter  $Sp$ :

$$\begin{aligned} Sp &= \frac{St \cdot Pr}{\sqrt{\frac{1}{2}c_f}} \\ Sp \left( x^+, \frac{Pr}{Pr_t} \right) &= - \left( \frac{\partial \theta}{\partial u^+} \right)_{u^+=0} \\ \theta &= \theta \left( x^+, u^+, \frac{Pr}{Pr_t} \right) \end{aligned} \quad (32)$$

where the + superscript denotes wall coordinates [32]. This relation does not require  $Pr$  to equal turbulent Prandtl number ( $Pr_t$ ) for accurate results. The solutions to the Spalding function are very applicable to turbulent boundary layers. Spalding claimed

boundary layers with transpiration could use the same equation, a claim he never experimentally verified.

Al Saji [33] found through experimentation the Spalding function requires different coefficients for each different turbulent boundary layers with transpiration, though  $Sp$  with these new coefficients (derived for each case) matched his data quite well. He derived a temperature law of the wall for transpired turbulent boundary layers, similar to and based on Stevenson's [34] law of the wall. He went on to say, as shown from his experiments at least, these boundary layers are not similar. In other words, the Reynolds analogy does not precisely apply due largely to  $Pr_t$  not being a constant 0.887, an assumption made in analytical models. He stated  $Pr_t$  is moderately influenced by blowing ratio. He verified these results, as well as those of Spalding, using a 26-ft wind tunnel with hot air as the free stream and cold air as the coolant.

Other early models were developed by many involved in investigating turbulent boundary layers, including Rubesin [35] Hacker [36], Mickley [37], Bartle and Leadon [38], Kutateladze and Leon'ev [39], and Kinney [40]. An excellent and thorough survey of most of these early analytic transpiration cooling models was produced by Jeromin [9]. All of these models share similarities with the Spalding model in the attempt to relate blowing parameter to  $c_f$  ratio, which via the Reynolds analogy is equal to  $St$  number ratio. However, the Kays/Crawford model (Eq. 39, p. 29) is proven [41] to be the most accurate of today's existing analytical models.

## 2.4 *Empirical Correlations of Cooling Effectiveness*

The first analytical models of the transpiration process with heat transfer came about in the 1950's and 60's. The first such model was the Rannie model which is commonly used to predict wall temperatures:

$$R = \frac{T_\infty - T_c}{T_s - T_c} = \left[ 1 + \{1.18 Re_\infty^{0.1} - 1\} \left\{ 1 - e^{-37 F Re_\infty^{0.1}} \right\} \right] \left[ e^{37 F Re_\infty^{0.1} Pr_\infty} \right] \quad (33)$$

The right hand side of this equation is purely empirical, though the use of  $R$  has analytical significance. [6, 42] Eq. 33 is common because it was the first to predict wall temperatures in a transpiration cooled wall. Its limit is the lack of use of the properties of the transpired fluid. As more experiments were performed it became apparent these properties play a significant role in heat transfer reduction.

Ren, et al. [43] developed another 1-D model for predicting the performance of transpiration cooling, this time including chemical reactions to a limited extent. They found a critical blowing ratio, and determined at blowing ratios below this there would be negligible effects on the free stream conditions. They also noted their multi-species boundary layer equation solution method<sup>3</sup> possessed fast iteration and convergence properties, even with large gradients in density and temperature.

In turbine film cooling, the adiabatic efficiency,  $\eta_f$ , is expressed as a surface temperature change (similar to  $R$  in Eq. 33) instead of a heat flux change:

$$\eta_f = \frac{T_\infty - T_{aw}}{T_\infty - T_c} \quad (15)$$

$T_{aw}$  is the adiabatic temperature of the gas immediately above the wall being cooled, and as  $T_{aw} \rightarrow T_c$ ,  $\eta_f \rightarrow 1$ .  $T_c$  is the coolant temperature at the exit of the cooling hole. This is hotter than the reservoir temperature since the coolant picks up heat from the wall as it passes through. Many factors affect  $\eta_f$ , and some of these factors may interact in a coupled fashion: injection angle, blowing ratio, momentum ratio, density ratio, species difference, compound injection, and hole spacing. Much of the testing leading to the conclusions in this section was performed on flat plates at subsonic conditions. Free-stream Mach number is assumed to have little or no effect on cooling efficiency.

If the coolant is injected through slots,  $\eta_f$  is proportional to  $x/sF$ , where  $x$  is the distance downstream of the slot and  $s$  is the slot width. Teekaram [45] found it

---

<sup>3</sup>Simply Keller's box method [44].

is also inversely proportional to  $F$  in general. For a  $45^\circ$  injection angle, the curve fit

$$\eta_f = 16.9 (x/Fs)^{-0.8} \quad (34)$$

was proposed by Hartnett [46]. Further, slot injection is known to be more efficient than round hole injection, since the maximum coolant coverage width cannot exceed the hole width. Also the injection velocity is higher for the same blowing ratio when using holes vs. slots, thus tending to increase mixing and heat transfer.

Gas turbine film cooling tests typically involve injecting cool air into hot free-stream air. For these flows, the density ratio (DR),  $\rho_c/\rho_\infty$ , is  $\approx 2$ . Blowing ratio,  $F$ , is usually used as a comparison for DR, although the momentum ratio,

$$I = \rho_c u_c^2 / \rho_\infty u_\infty^2 \quad (35)$$

is sometimes used. Cutbirth [47] found over a wide range of blowing ratios (1-4), cooling efficiency near the hole is not greatly affected by a change in DR until DR increases above some minimum. Then there is a slight increase in cooling efficiency. A higher DR tends to exhibit higher cooling efficiencies at higher momentum ratios. DR may have a considerable effect on cooling efficiency in rockets, where cryogenic liquid fuel is injected into hot gas. Though in a turbine DRs on the order of 2-3 are expected, in a rocket DR can range from 10 to over 1000, depending on the fuel and chamber conditions. This means the DR effects determined pertinent to turbine film cooling may not apply to rockets, and similarly there may be huge density ratio phenomena which come into play at these higher DRs. No data has been taken on cooling effectiveness at these DRs.

## ***2.5 Pressure Gradient Effects***

A favorable pressure gradient is what causes flow to accelerate, and is usually due to a contraction in the available flow area, as in Fig. 5. Pressure gradients are

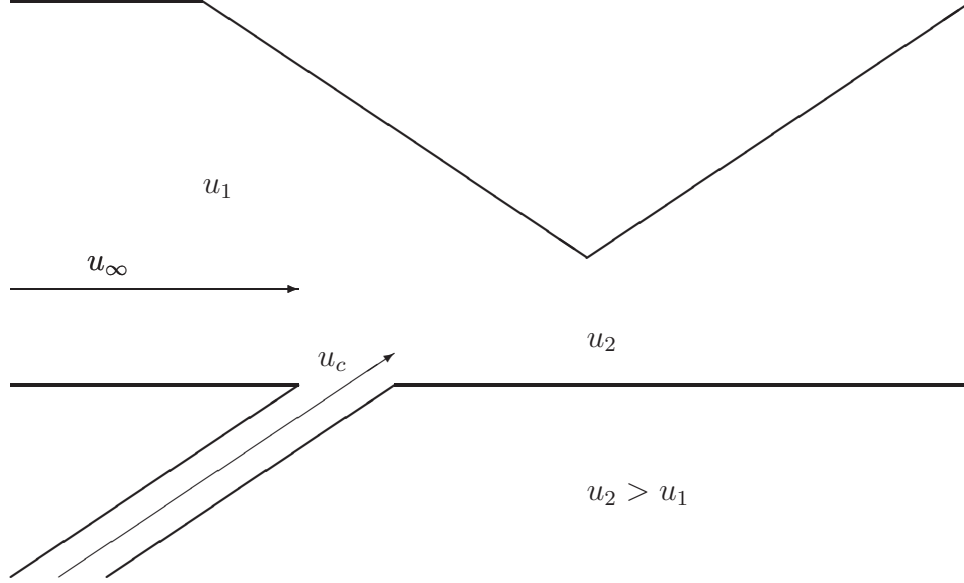


Figure 5: Strong favorable stream-wise pressure gradient inducing flow acceleration. The pressure decreases from point 1 to point 2 because of the constriction on the upper wall, which causes an acceleration,  $u_2 > u_1$ .

measured by their severity using an acceleration parameter defined by

$$K = \left( \frac{\nu}{u^2} \right) \frac{du}{ds} \quad (36)$$

A positive value for  $K$  indicates a favorable pressure gradient. Turbulent boundary layers will tend to re-laminarize if  $K > 3 \times 10^{-6}$  approximately [48]. Pressure gradients have a moderate effect on film cooling adiabatic effectiveness at low blowing ratios and Mach numbers but until recently contradictory data from experiments clouded whether favorable pressure gradients are beneficial or detrimental to cooling efficiency. High Mach numbers or high blowing ratios minimize the effect of pressure gradients on adiabatic effectiveness.

Though the effects of pressure gradient on cooling effectiveness appeared to be contradictory, the present data may represent a single trend. Dellimore et al. [49] at the University of Maryland improved film cooling models by showing pressure gradient effects are dependent on the velocity ratio. If the film velocity is greater than the free-stream flow, a favorable pressure gradient will increase cooling effectiveness since it

helps to force the coolant stream back to the wall. Conversely, favorable pressure gradients in a free-stream velocity-driven system reduces cooling performance. This is due to the movement induced upon the impingement point, the point the coolant layer begins to mix heavily with the free-stream shear layer.

Free-stream turbulence and flow separation (in the presence of extreme adverse pressure gradients) were cited as reasons for the the two cases not explained by their new model. Additionally, their model was based on geometry encountered in injector-based film cooling, wherein a ring of cold fuel is injected along the combustion chamber wall parallel to the injected fuel and oxidizer meant for combustion. This is a different setup than the wall-injected film cooling discussed so far, but the same general trends may apply [49].

Stream-wise curvature has been studied heavily in the past, as most turbine blades are cooled in areas of both convex and concave curvature. Ito [50] found wall curvature can increase or decrease adiabatic effectiveness by as much as 80% compared to flat plate values. Concave curvature decreases effectiveness for the same reasons it generally increases heat transfer and skin friction coefficient. The measure of curvature commonly employed is:

$$Cr = \frac{\nu}{u_{\infty} R} \quad (37)$$

This amounts to an inverse  $Re$  based on the radius of curvature of the wall. Sharp concave curvature tends to reduce effectiveness in terms of both temperature and heat transfer for several reasons. [7] First,  $Pr_t$  is affected by curvature, resulting in increased turbulent mixing. Second, the impingement of the boundary layer on the wall tends to thin the layer and consequently increase heat transfer. Data for a concave wall at several blowing ratios is available for the case  $Cr \approx 2.1 \times 10^{-3}$ . Flat plate data starts to lose applicability when  $Cr > 0.26 \times 10^{-6}$  [7]. In other words, flows with high  $Re$  in the direction of curvature or very large radius of curvature are nearly unaffected.

## 2.6 Flowfield Dependence

*Free-stream Turbulence and Roughness.* Free-stream turbulence and surface roughness can have a huge effect on the effectiveness of any effusion cooling scheme. The higher the turbulence level, defined by

$$Tu = \frac{u'_{rms}}{\bar{u}} \quad (38)$$

the more quickly the coolant mixes into the free-stream. Jumper [51] showed near the hole low levels of turbulence ( $Tu \leq 8\%$ ) have very little effect. Bons [52] explained the exact amount cooling effectiveness will decrease is dependent on blowing ratio, frequency and amplitude, so it is difficult to quantify. For example, when  $Tu$  was increased from 10% to 17% Schmidt [53] found  $\eta_f$  decayed to zero at 20 hole diameters from the hole ( $x/d = 20$ ), and the adiabatic effectiveness near the hole was reduced by half. Using higher blowing ratios can compensate for this effect, but as Kadotani [54] points out, this could result in a detrimental increase in coolant use for a rocket.

Rutledge et al. [55,56] showed higher surface roughness affects cooling efficiency and heat flux. Roughness downstream of the hole can increase the heat transfer coefficient  $h$  by as much as 150%, much more than typical NHFR values found in film cooling. The addition of upstream roughness decreases the high  $h$  value by  $\approx 10\%$  due to the thickness of the boundary layer increasing. Further testing revealed heat transfer to the wall can double due to roughness alone.

*Specific Heat Capacity.* Simpson et al. [57] experimented with transpiration cooling in the late 1960's. They developed a model of transpiration cooling using the ratio of specific heat capacities to determine the blowing parameter. By solving the Couette-simplified momentum equation and using the Reynolds analogy a result similar to, but simpler than, Spalding's (Eq. 29, p. 23) was obtained:

$$\frac{c_f}{c_{f,o}} = \frac{\ln(B_h + 1)}{B_h} \approx \frac{St}{St_o} \quad (39)$$

with the new similarity-based thermal blowing parameter given by:

$$B_h = \frac{F}{St_o} \left( \frac{c_{p,\infty}}{c_{p,c}} \right)^{0.6} \quad (40)$$

This relation appears to be valid for enthalpy boundary layer thicknesses of  $800 < Re_{\Delta_i} < 11,000$ . It provides a good fit for transpiration cooling processes without resorting to empirical correlations. Lezuo [41] states it is commonly used to predict wall heat flux reduction. However, like all  $St$  number correction models, its accuracy in predicting actual heat flux is limited by the relation used to predict the un-cooled Stanton number  $St_o$  (for rockets, often the semi-empirical Bartz [10] equation is used). The Reynolds analogy is also required to arrive at this equation, implying that if  $Pr_t$  is far from unity, Eq. 40 will not apply.

Consequently, Kays and Crawford [7] related  $St$  with transpiration to the  $Pr$  and  $St$  of the free stream flow, resulting in the implicit equation:

$$St \cdot Pr^{0.4} = 0.0287 Re_x^{-0.2} \frac{\ln(B_h + 1)}{B_h} \quad (41)$$

The applicability of this equation was shown for flows including blowing, suction, acceleration, and deceleration with good agreement, although the data used to verify the relation admittedly had poor accuracy ( $\pm 10\%$ ).

Transpiration cooling can also be applied to supersonic and hypersonic reentry vehicles as protection for the outer surface. Raghuraman [58] used the Bartle-Leadon [38] model of  $St$  reduction:

$$\begin{aligned} \frac{St}{St_o} &= \frac{B_h}{(B_h/3 + 1)^3 - 1} \\ B_h &= \frac{F}{St_o} \left( \frac{c_{p,\infty}}{c_{p,c}} \right) \end{aligned} \quad (42)$$

derived from data for high speed flows,  $2.0 < M < 3.2$ . Although the test data did not correlate very well with the model, they did achieve a drastic reduction in surface



temperatures (in most cases over 50% with transpiration cooling) with quite small (3.402 g/sec) transpiration mass flow rates. Work in this field presently continues at Aerojet.

When cooling a combustion chamber wall, the fuel or the oxidizer are may be used as coolants. In 1998 several studies were carried out in China to determine the utility of transpiration cooling in controlling heat flux to the combustion chamber wall. One analysis used liquid oxygen, rather than fuel as other studies had done, as the transpirant. Weiqiang et al. [59,60] developed an analytical 1-D model to predict the performance of such a device using RP-1 as fuel. They concluded higher blowing ratios over fuel (as coolant) would be required to keep more of the wall cold. They also concluded (somewhat obviously) liquid hydrogen would make a better coolant than oxygen simply because the specific heat is higher for hydrogen.

Though the dependence of cooling effectiveness on specific heat has been experimentally shown for transpiration cooled walls, it has not been shown for the film cooling cases since most data is from air injected into air. The same relations may apply for many blowing ratios, and should apply well at very close hole spacing and small jet diameter, all other factors being equal.

*Mach Number.* Since 1994 the German Aerospace Center (DLR) has run several simulations and tests using transpiration cooling in rocket combustion chambers. Lezuo et al. [61] built a combustor using  $H_2/O_2$  to test the effectiveness of transpiration cooling using porous wall segments. Their first tests used gaseous hydrogen and water as coolants at up to 1.5 MPa. They showed an increase in combustion chamber pressure tends to decrease the transpiration cooling efficiency,  $\eta_t$ . Likewise, an increase in chamber hot gas average velocity tends to decrease the cooling efficiency. Finally, both the Stanton number and hot side wall temperature decreased with an increased coolant mass flux.

In parallel with more tests using hydrogen as coolant, Lezuo [41] then developed an analytical 1-D model of the transpiration cooling process. The model is valid for

constant property flow, and uses the Darcy equation [62] to relate permeability to porosity. This model was compared to existing analytical models and with experimental data. These tests were with an oxidizer to fuel ratio (O/F) of 6.5 and chamber pressures varying from 0.3 to 1.6 MPa. Comparing their data to several of the early analytical models, they found the Bartle-Leadon model [38] tended to underestimate the wall temperature, while the Kutateladze model [39] tended to overestimate it. The Kays/Crawford [7] and Hacker [36] models were almost identical in their predictions, and though they fit the data better than the other models, neither one accounted for the cooling boundary layer thickness and its effect on cooling efficiency. They found for  $B_h/St_o < 4$ ,  $St$  had a large effect on heat transfer. They therefore determined a modified version of the Kays/Crawford model would best fit the data.

The experimental data showed a linear relationship between the  $St$  and the cooling efficiency. Therefore Eq. 39 was modified to include this effect, yielding:

$$\eta_t = \frac{St}{St_o} = \frac{\ln(B_h + 1)}{B_h} \frac{Re_D}{Re_{bex}} \quad (43)$$

with Eq. 40 used to calculate  $B_h$ .<sup>4</sup> This relation agreed well with their experimental data, though it requires the assumption the wall temperature and coolant temperature are equal (verified by Landis). The relation between wall temperature and this new cooling efficiency was then simplified:

$$R = \frac{1}{1 + \frac{1}{\eta} \frac{F}{St_o} \frac{c_{p,\infty}}{c_{p,c}}} \quad (44)$$

Frohlke et al. [63] ran more tests, this time at pressures from 3.5 to 10 MPa, with the O/F still at 6.5. The results verified  $\eta_t$  was indeed related to the Reynolds number, but not precisely in the way thought previously. An empirical correction

---

<sup>4</sup> $Re_{bex}$  is a constant that was found to not vary with chamber pressure or free-stream velocity; the value was not given.

factor was added to Eq. 44, which now read:

$$\begin{aligned}
R &= \frac{1}{1 + \frac{e^{B_h}-1}{B_h} \frac{F}{St_o} \frac{c_{p,\infty}}{c_{p,c}} K(\text{Re}_D, F)} \\
K(\text{Re}_D, F) &= a(\text{Re}_D) e^{b(\text{Re}_D)F} \\
a(\text{Re}_D) &= 1.8357 \times 10^6 \text{Re}_D^{-0.9516} \\
b(\text{Re}_D) &= 1.148 \times 10^{-10} \text{Re}_D^2 - 1.967 \times 10^{-4} \text{Re}_D - 164.06
\end{aligned} \tag{45}$$

$$2.78 \times 10^5 < \text{Re}_D < 6.92 \times 10^5$$

Using this relation, more tests were run using hydrogen coolant to discern the effect of material properties and porosity on the transpiration cooling effectiveness. In particular, the feasibility of carbon/carbon (C/C) porous liners was in question. This experiment intended to prove their utility in combustion chamber wall cooling. From a materials standpoint, the results were promising—after 500 total seconds of firing the liner had sustained no observable damage. Furthermore, the results showed material porosity had a minor but discernible effect on cooling film temperature (though not as much of an effect as Reynolds number). A minimum blowing ratio of 0.005 was determined to be the limit at which materials with thermal integrity above 1000  $K$  would be required. Also, the temperature ratio still increased with increasing Reynolds number, but it was determined this nonlinear relationship needed more refinement.

Therefore, already heavily-adjusted Eq. 45 was once again modified:

$$\begin{aligned}
K &= a + b(\text{Re}_D) e^{c(\text{Re}_D)F} \\
a &= 0 \\
b(\text{Re}_D) &= \frac{149,000}{\text{Re}_D} \\
c(\text{Re}_D) &= 0.001923 \text{Re}_D - 9.1596
\end{aligned} \tag{46}$$

No range, in terms of Reynolds number or blowing factor, was included with this expression.

The next year Meinert and Huhn [2] at the University of Dresden, Germany, working with DLR, ran experiments on their own hot air wind tunnel to determine the effects of molecular weight ratio between transpired coolants and the hot free stream gas on skin friction and heat transfer. Using argon, helium, nitrogen, hydrogen, and methane as coolants, they showed a strong correlation between molecular weight ratios and a lesser dependance on specific heats, as in Eq. 40. Building upon the empirical results from DLR, they were able to show the critical blowing ratio, the point at which blowing induces flow separation, is given by:

$$\frac{2F_{crit}}{c_{f,o}} \left( \frac{M_\infty}{M_c} \right)^{0.9} \approx 5.0 \quad (47)$$

They also modified (33) to compensate for Reynolds number effects:

$$\begin{aligned} R &= \frac{\exp(A\varphi^* \text{Pr}^* F)}{1 + \frac{c_{p,c}}{c_{p,\infty}} (B\varphi^* - 1) [1 - \exp(A\varphi^* F)]} \\ \varphi^* &= \eta \text{Re}_x^{0.1} \\ A &= -67.5, B = 0.51 \end{aligned} \quad (48)$$

There was an asymptotic response of  $\eta_t$  with increasing  $F/St_o$  to not go to zero as the above equation predicts. Instead  $\eta_t$  decayed to about 0.04, which is close to the predicted radiation heat flux for this scenario. Radiation was cited for the discrepancy, since  $H_2O$  vapor (a radiating gas) constituted about 60% of the free stream gas by mol fraction.

*Material Requirements for High Thermal Gradients.* As identified by students at AFIT [13], any material used in transpiration cooling of a hot rocket wall must have a very high tolerance to thermal gradients. Thus the next step in the investigation of transpiration cooling at DLR was to apply Ceramic Matrix Composites (CMCs) to its use. While the material performed well under operating conditions, there was a bit of trouble correlating their data to their previously derived models for the same reasons

stated before. Specifically, radiation effects were not accounted for in the model, but were present in the data.

In addition to testing the material feasibility of CMCs, the effect of upstream cooling was also examined. Serbest et al. [64] found adding upstream cooling in addition to throat cooling would lower wall temperatures an additional 1-4%. Furthermore, a distinct effect on wall heat flux was observed with a change in chamber pressure, as was noted previously. Their experiments were run at a chamber pressure of  $0.8\text{ MPa}$  and temperature of  $3340\text{ K}$ .

After some optimization of the internal structure of the CMCs, further tests were run to determine the benefits of transpiration cooling over regenerative cooling. Specifically, detailed studies were performed to determine the effect of blowing ratio on  $I_{sp}$ . Dunn [65] verified Landis' [17] operational range of blowing ratios of  $0.004 < F < 0.007$  using Two Dimensional Kinetics (TDK). Since a suitable expression for the local cooling efficiency inside a converging section has not been developed, numerical calculation continues to be the only basis for a useful comparison [8].

Several other European experiments were run outside of DLR which demonstrated empirically the effectiveness of transpiration cooling in controlling wall temperatures. Pioneering the German-Russian relationship in rocket technology investigation, Zinner et al. [3, 66] ran tests using transpiration cooling in several sections of a combustion chamber, including the convergent part, using water and hydrogen as coolants. This method of cooling was inefficient when used in all parts of the chamber, leading them to conclude only the throat should be cooled via transpiration for maximum performance gain.

While testing the  $1500\text{ psi}$ ,  $100,000\text{ lbf}$  thrust engine, they found some anomalous behavior (when compared to the previous work shown herein). In some parts of the chamber, the heat flux was actually increased with transpiration, when compared to the un-transpired control tests. No explanations were given for this strange behavior. However, Kays has noted [7] below a certain  $F$ , effusion serves to increase

turbulent mixing more than reduce heat flux, possibly accounting for this anomaly. Further, when two chamber sections were transpiration cooled, one downstream of the other, the downstream section experienced only half of the heat flux reduction as the upstream one. In the throat section, expected behavior was observed and the heat flux was reduced by approximately 30% with transpiration. The nozzle was also cooled, but with such low wall temperatures even when un-cooled, the benefit of transpiration cooling in this section was not very great (about a 10% reduction in heat flux).

Though it is unknown if new analytical models are being developed at DLR, several experiments designed to tune CMCs to transpiration cooling use are being planned and carried out over the next few years [67]. So far, the high temperature tolerance and low thermal conductivity of C/C suggest a stellar performance in this application.

At the University of Alabama [68], perforated plates were considered for transpiration cooling applications. The holes' average diameter was 44 microns, and the open area for coolant flow was just over 5%. The plate behaved more like a porous media and less like a film cooling surface. Numerical analysis confirmed Landis' results via implementing Eq. 46. Although wind tunnel testing apparently never took place, this is another example of successful 1-D modeling of transpiration with heat transfer.

Wang and Wang [69] developed a numerical model for transpiration and ablation cooling to predict heat flux and wall temperature. Their model applied a high heat flux on one side of a porous plate and a gaseous coolant and high pressure on the other side. Neglecting the heat conduction through the porous solid, the 1-D model used the compressible, transient, constant property continuity and energy equations with the ideal gas law. Variable viscosity was accounted for via Sutherland's law. Though using a simplistic model, they made some relevant conclusions. First, any numerical model of transpiration cooling should include variable thermal properties

because of the wide range of fluid temperatures encountered.<sup>5</sup> Second and somewhat obvious, increasing the transpiration coolant flux would help to avoid the ablation of wall material caused by high temperature. Third, a change in  $St$  only affects the transient response of the hot side wall temperature; the steady state temperature remains the same regardless of  $St$ . Fourth, the coolant flux has a drastic effect on the hot side wall temperature.

## 2.7 *Summary*

A general trend is observed in effusion cooling: increasing blowing ratio, up to a certain point, decreases heat transfer to a wall or the wall temperature, or both. Several factors, like turbulence, pressure gradients, hole geometry, and injection angle (for film cooling) can have large effects on wall temperature and heat flux. Manufacturing improvements have introduced film cooling as a viable cooling method for rocket walls. The utility and importance of an algebraic solution for cooling effectiveness in rocket conditions cannot be ignored, despite the availability of powerful Computational Fluid Dynamics (CFD) tools. Bogard and Thole [5] point out many simulations have been run, but CFD is still weak when predicting the jet separation from the wall, regardless of the turbulence model being used. The governing equations resist conventional simplifications in these flows, but much progress has been made to understand the general behavior of effusion cooling and its limits of applicability. Much work remains to be done to characterize the injection of a super-critical fuel into a highly turbulent, transonic, combusting environment.

---

<sup>5</sup>Most of the analytical models available are based on the constant property assumption.

### III. Computational Performance Prediction

Simulations used in this project yielded preliminary estimates of relative performance between cases for objective 1 (p. 5). First, an investigation on the relation between full coverage film cooling and transpiration cooling was performed. Next, predictions on cooling performance were made based on three diameter ratios, three compound injection angles, and five blowing ratios.

#### 3.1 *Transpiration vs FCFC*

As discussed in Chapter II, full-coverage film cooling (FCFC) is the injection of coolant via discrete holes, while transpiration cooling forces coolant through a porous media. Though the nomenclature is often used interchangeably in the rocket community, large differences exist in terms of each schemes ability to cool the wall. Transpiration cooling will cool the wall better than FCFC in many cases simply because the exit velocity of the coolant is so low, and there is a correspondingly low increase in turbulent mixing near the wall, if any at all. The claim has been made, however, that if the holes are sufficiently small, and sufficiently close together, that FCFC behaves like transpiration cooling [7], and this section seeks to quantify the claim.

*Method of Comparison for Transpiration and Film Cooling Schemes.* The velocity blowing ratio as commonly used in film cooling is defined as

$$F = \frac{\rho_c v_c}{\rho_\infty v_\infty} = \frac{\dot{m}_c''}{\dot{m}_\infty''} \quad (49)$$

where  $\rho$  is the density,  $v$  is the velocity, and  $\dot{m}''$  is the mass flux of both the coolant, subscripted  $c$ , and the free-stream, subscripted  $\infty$ , fluids. The mass flux is equal to the mass flow rate  $\dot{m}$  divided by the flow's cross-sectional area,  $A$ . The velocity of a fluid exiting through a coolant passage (even if that passage is the entire wall area as with transpiration cooling) is:



$$v_c = \frac{\dot{m}_c}{\rho_c A_f} \quad (50)$$

where  $A_f$  is the coolant flow cross-sectional area in the plane of the wall being cooled.

Thus the blowing ratio  $F$  can be written

$$F = \frac{\dot{m}_c/A_f}{\rho_\infty v_\infty} \quad (51)$$

$$= \frac{\dot{m}_c/A_f}{\dot{m}''_\infty} \quad (52)$$

If the wall is transpiration cooled, then  $A_f = A_t$ ,  $A_t$  being the total wall area. If the wall is film cooled, then there is a relation between  $A_f$  and  $A_t$ . Assume the coolant passages have equal circular cross sections of radius  $r$  and have equal spacing  $P$  over the area ( $P$  is the *pitch*, or spacing between holes). Also assume the coolant exits at velocity  $v_f$  in the direction normal to the wall. Then the portion of the surface area which is coolant channel,  $S$ , is

$$S = \frac{\pi r^2}{P^2} = \frac{A_f}{A_t} \quad (53)$$

For transpiration cooled walls,  $S = 1$ . It is important to know how the coolant velocity changes for a fixed total coolant mass flow, as this allows one to find the maximum efficiency for a cooling process. To find how the transpiration coolant velocity for a fixed mass flux changes as the coolant passages assume less and less of the surface area (approaching full-coverage film cooling), Eq. 50 is used:

$$\frac{v_f}{v_t} = \frac{A_t}{A_f} \quad (54)$$

This equation is simple because it does not account for the difference in coolant exit temperature resulting from the flow conditions inside the plenum (in the case of

film cooling) or the porous media (in the case of transpiration cooling). Instead, it is a pure conservation of mass comparison between two ideal flow conditions which maintains the coolant use proportional to the total flow through the rocket. Substituting Eq. 53 into Eq. 54 yields

$$\frac{v_f}{v_t} = \frac{1}{S} \quad (55)$$

So for a given total coolant mass flow, the coolant velocity will increase linearly as the coolant surface area decreases. For this computational study circular cross sectional flow channels are used. So an equation relating blowing ratio to coolant hole radius is needed:

$$\begin{aligned} F_f &= \frac{\dot{m}_c/A_f}{\dot{m}''_\infty} \\ \frac{F_f}{F_t} &= \frac{A_t}{A_f} \\ &= \frac{1}{S} \\ &= \frac{P}{\pi r^2} \end{aligned} \quad (56)$$

Equation 56 constrains the hole geometry for a given transpiration blowing ratio and, for a given pitch  $P$ , can be used to find required hole radius so that the total coolant used is the same as the transpiration case. The radii for a variety of commonly desired film cooling blowing ratios are shown with the results in Table 1. The *pitch to hole diameter ratio*,  $P/d$ , was used as the comparison value for each case. The transpiration blowing ratio used for comparison is  $F_t = 0.007$ . This ratio is typical of what would be required to cool the converging section of a rocket nozzle as found by Lenertz [14].

The area-averaged adiabatic effectiveness was used to compare full coverage film cooling to transpiration cooling. Recall from p. 12 adiabatic effectiveness for film

cooling is defined as

$$\eta_f = \frac{T_\infty - T_{aw}}{T_\infty - T_c} \quad (15)$$

where  $T_\infty$  is the free-stream temperature,  $T_{aw}$  is the adiabatic wall temperature, and  $T_c$  is the coolant temperature at the hole exit.  $\eta_f$  is a non-dimensional measure of the effectiveness of the coolant at the wall. When  $\eta_f = 0$  the wall is un-cooled, and when  $\eta_f = 1$  the wall is completely cooled, or equal to the coolant injection temperature.

Recall from p. 12  $\eta_f$  may be averaged over an area to give the area-averaged adiabatic effectiveness,  $\zeta$ :

$$\zeta = \frac{1}{(\xi_2 - \xi_1)(\gamma_2 - \gamma_1)} \int_{-\xi_1}^{\xi_2} \int_{-\gamma_1}^{\gamma_2} \eta_f \, dx \, dy \quad (17)$$

On a transpiration cooled wall  $T_{aw} = T_c$ , so  $\eta_f$  is unity along the entire surface. The rationale for using the temperature adiabatic effectiveness as opposed to the heat flux reduction commonly used in transpiration cooling is one based on the expected lateral conduction effects on the wall with full coverage film cooling. When much of the surface is not covered by coolant ( $P/d$  is large, on the order of 10 or greater) lateral and stream-wise conduction of heat along the surface is very important, as this is the chief method by which the coolant jet cools the entire surface.

As  $P/d$  shrinks, less of the total area is used by the wall, and more is used by the coolant holes themselves. Thus, conduction effects diminish as more area is taken up by coolant holes. Once transpiration cooling is achieved or closely approximated, the conduction effects are nil since the wall almost immediately takes on the temperature of the coolant at the wall. Additionally, the methods of cooling in the two cases are fundamentally different. In transpiration cooling, heat flux is reduced because the slow moving coolant thickens the viscous sub-layer above the wall, forcing conduction to take a larger role in the heat transfer. Film cooling works more by displacing the hot gas with a large amount of coolant, which is frequently cooler than the wall (due to conduction along the wall). This film replaces the heat transfer driving force to

one between the coolant and the wall. The further from the hole the jet remains attached to the wall, the further this conduction can take place. At very low blowing ratios, film cooling can take on elements of transpiration cooling by also thickening the sub-layer.

*Results of Transpiration Study.* A structured grid using Gridgen<sup>®</sup> V15.7 contained about 2.5 million cells. Average  $y^+$  values were on the order 0.01 over the entire wall. Enhanced wall treatments for pressure and thermal effects were used to ensure the best possible heat transfer discernment. No behind-the-wall phenomena or interactions were modeled (such as a plenum) since the problem of interest was the fluid mechanics portion of the film cooling problem. Ensuring uniformity of coolant properties is important to guarantee that all configurations are comparable. Fluent<sup>®</sup> 6.3 was used to solve the flow-field. The *realizable*  $k - \epsilon$  model was used with the default coefficients. The solution method was second order and converged to  $1 \times 10^{-6}$  residual for all equations but energy, which converged to  $1 \times 10^{-9}$ .

Eight rows of holes were modeled. The area-averaged adiabatic effectiveness  $\zeta$  was calculated from the area surround all of the holes to get an average coolant distribution over the area that would be transpiration-cooled by comparison. Table 1 shows how  $\zeta$  varies as  $P/d$  changes.  $\zeta$  is unity when transpiration cooling occurs, and drops as coolant wall coverage decreases. Thus the surface area that would be covered by transpiration cooling is the same area used to calculate  $\zeta$ .

To assess the utility of the transpiration models in Eq. 33 against the simulation results, a qualitative analysis is first employed. Equation 33 is based on a temperature difference between the free-stream wall temperature  $T_\infty$  and the temperature of the coolant at the porous liner. Putting this in terms of  $\eta$

$$\eta_t = 1 - \frac{1}{R} \quad (57)$$

$$\zeta = \frac{1}{A_t} \iint \eta_f dA \quad (58)$$

Recall the Rannie transpiration model:

$$R = \frac{T_\infty - T_c}{T_s - T_c} = \left[ 1 + \{1.18 Re_\infty^{0.1} - 1\} \left\{ 1 - e^{-37 F Re_\infty^{0.1}} \right\} \right] \left[ e^{37 F Re_\infty^{0.1} Pr_\infty} \right] \quad (33)$$

$R$  exhibits a dependence on free-stream Reynolds number ( $Re$ ) and the film mean Prandtl number ( $Pr$ ), which is usually defined as  $Pr_f = Pr^{1/3}$ .  $R$  was calculated along the surface for an ideal transpired surface and compared point by point to  $\eta$  over the entire surface. The error between  $R$  and  $\eta$  was averaged and plotted in Fig. 6. With 50% of the surface area covered with coolant holes that the error is effectively zero. However the Rannie model typically employs a 85% efficiency due to a slight over-prediction of performance. The error varies nearly linearly with  $S$ . The region of interest for most full-coverage film cooling surfaces is where  $5 < P/d < 10$ , which means  $0.0079 < S < 0.0314$  and  $0.22 < F < 0.89$ . Over this range  $\zeta/\eta_t$  varies nearly linearly.

A second order polynomial curve fit for valid for the entire range tested is

$$\frac{\zeta}{\eta_t} = -24.3792 S^2 + 4.4087 S + 0.0755 \quad (59)$$

as shown in Fig. 6. One would expect a closely linear relationship between  $S$  and  $\zeta/\eta_t$  since the coolant velocity varies linearly with coolant surface area. The departure from linearity simply shows there are non-linear flow effects which result in more reduction in effectiveness at higher velocities than a simple linear area-based calculation would predict.

Table 1: Results of  $\zeta$  and Error For P/d Values Tested in FCFC Study

$F_f$	0.01	0.05	0.10	0.25	0.50	0.75	1.00	1.25	1.50
$P/d$	1.1	2.4	3.4	5.3	7.5	9.2	10.6	11.8	13.0
$S$	0.6648	0.1391	0.0699	0.0280	0.0140	0.0093	0.0070	0.0056	0.0047
$\zeta$	0.8695	0.301	0.1913	0.1245	0.1018	0.0879	0.0779	0.0692	0.0619
$\zeta/\eta_t$	1.2029	0.4168	0.2652	0.1727	0.1413	0.122	0.1082	0.0961	0.0859

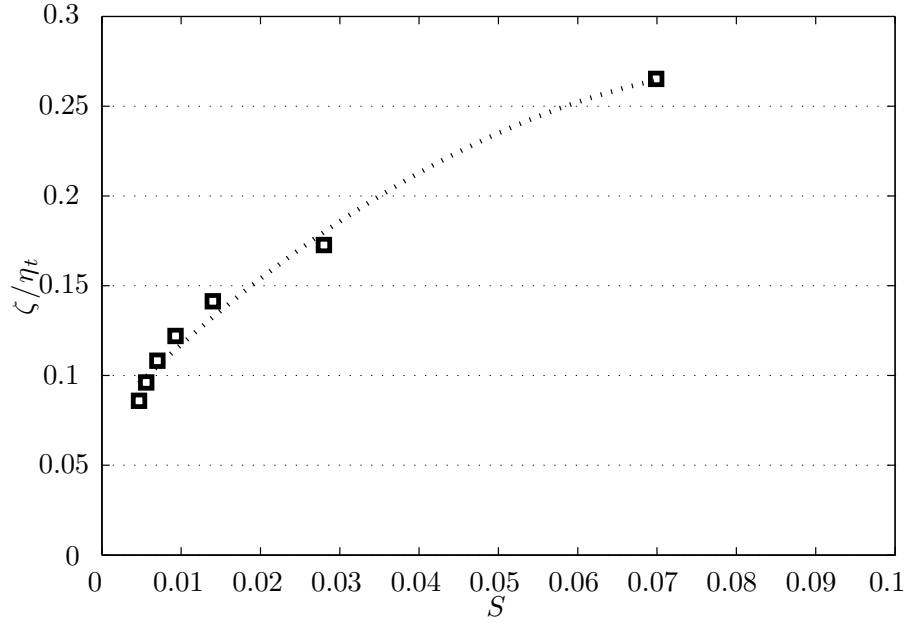


Figure 6: Correction factor for Rannie-predicted temperature and the area-averaged film cooling surface temperature  $\zeta$  vs area ratio  $S$ . Eq. 59 is also plotted over the data points.

### 3.2 Simulations of Curved Geometry

Understanding the effects of radial curvature (curvature perpendicular to the bulk flow) is important for several reasons. First, the impingement of the coolant jet with compound angle injection will increase heat transfer more than on a flat plate. Second, the jet shape downstream from the hole will be affected, resulting in a thinner, longer jet. This will impact the placement and design of the coolant holes. Third, if this cooling method is employed *en mass* inside a rocket combustion chamber, the applicability of flat plate data to the design of such a cooling system will be greatly increased as the differences between the two operating conditions is quantifiably understood.

*Comparing Internal Film Cooled Surfaces.* Internal flows are dynamically similar if the internal Reynolds numbers (based on diameter) are equal:

$$Re = Re_D \equiv \frac{\overline{u_\infty} D}{\nu_\infty} = \frac{\dot{m}'' D}{\mu} \quad (60)$$

where  $\dot{m}''$  is the mass flux,  $D$  is the internal diameter, and  $\mu$  is the viscosity. If the radius (or diameter) of the free-stream is the only difference between two flows, the ratio of  $Re$  is:

$$\frac{Re_1}{Re_2} = \frac{D_1}{D_2} \quad (61)$$

Similarly, for the coolant jet:

$$Re_j = \frac{\overline{u_j} D_j}{\nu_j} \quad (62)$$

The effectiveness of film cooled surfaces can be compared via velocity blowing ratio  $F$ :

$$F = \frac{\rho_j \overline{u_j}}{\rho_\infty \overline{u_\infty}} = \frac{\dot{m}_j''}{\dot{m}_\infty''} \quad (10)$$

If identical, incompressible fluids are used then density and viscosity are equal. Then  $F$  can be written:

$$F = \frac{Re_j}{Re_\infty} \frac{D_\infty}{D_j} \quad (63)$$

Therefore the blowing ratio as defined is independent of any change in free-stream diameter, so long as the mass fluxes remain unchanged.

The curvature number previously defined for concave and convex curvature on p. 28 is

$$Cr = \frac{\nu}{u_\infty R} \quad (37)$$

where  $\nu$  is the viscosity,  $u_\infty$  is the free-stream velocity, and  $R$  is the radius of stream-wise curvature, cannot be directly applied to radially curved flows since the curvature occurs in the direction *perpendicular* to the bulk flow.  $Cr$  is used for two-dimensional (2-D) flows, and curvature in the direction of interest would not appear in 2-D.

If a jet is compound injected onto a radially curved surface, the jet sees a concave wall ahead as it exits the coolant hole. The freestream air does not experience curvature in the stream-wise direction. Further, some studies mentioned in Sec. 2.5 [7, 49, 50] showed the momentum ratio tells which flow will dominate the cooling performance when a pressure gradient (or curved wall) affects the system. With these facts in mind, a new curvature parameter relating radial curvature to jet velocity is introduced:

$$C = \frac{D_j/D_\infty}{I} \quad (64)$$

The use of  $C$  is warranted based on previous curvature research and most strongly applies when compound injection of  $90^\circ$  is used. In this configuration, the jet, upon exiting the coolant hole, sees a concave wall in the jet direction. The momentum ratio determines how quickly the compound jet turns, and consequently how long the compound jet sees the curved wall ahead. Further, scaling  $I$  by the diameter ratio of the outer wall to the coolant hole allows direct comparison of a variety of wall curvatures. Note as  $D_\infty \rightarrow \infty$  the flat plate is approached, and  $C \rightarrow 0$ . This is similar to the diminished effect of  $Cr$  on flows with high  $Re$  or large radii of curvature,  $R_\infty$ .



Table 2: Radial Curvature Parameter  $C$  Values Used in  $\eta_f$  Simulations

		$F$				
		0.5	0.7	1.0	1.25	1.5
$\frac{D_\infty}{D_j}$	33.12	0.1250	0.0625	0.0303	0.0192	0.0133
	64.48	0.0625	0.0313	0.0156	0.0099	0.0069
	97.12	0.0417	0.0208	0.0103	0.0066	0.0046

The parameters simulated in this study encompass  $C$  values as shown in Table 2. These values were calculated based on blowing ratios of 0.5 to 1.5 and diameter ratios ( $D_\infty/D_j$ ) of 33.12 to 97.12.

*Grid Setup.* Solidworks<sup>®</sup> 2007.3 was used to design the test apparatus, so this model was easily exported into grid generation and Computational Fluid Dynamics (CFD) programs as an IGES file. GridGen<sup>®</sup> v15.4 and SolidMesh<sup>®</sup> 5.30 (from the Mississippi State University) were used to generate the grid used for CFD. The IGES file from Solidworks<sup>®</sup> was first imported into Gridgen<sup>®</sup>. Connectors were placed on all vertices for domain edges. The node spacing along each connector were chosen based on the very iterative process of a grid convergence study. Each grid contained between 2.5 and 2.8 million cells.

Gridgen<sup>®</sup> added unstructured domains to the model using the nodes spaced along the connectors. The only non-default setting used in this step was the domain along the pipe wall was generated with a boundary decay factor of one. This ensures connectors with close node-spacing propagate the spacing as far as possible into the domain, resulting in a higher density grid farther from each hole. This is important for capturing the temperature effects of coolant outside the immediate vicinity of the hole.

SolidMesh<sup>®</sup> filled in the volume of the gridded-model. Normal boundary layer growth was used on all of the walls (the pipe wall and the coolant hole walls), and the other domains were allowed to be rebuilt to accommodate the new structured boundary layer grid. The rebuilt domains consist of the coolant hole injection surfaces,

the mainstream in and out flow, and the periodic planes. The normal boundary layer growth placed the first grid point close to the wall at a wall  $y^+ < 1$  to keep plenty of grid points in the sub-layer, which yields more accurate boundary layer results. This new volume mesh was saved as a Fluent<sup>®</sup> case file.

*Fluent Setup.* Fluent<sup>®</sup> 6.3.21 predicted the adiabatic effectiveness of the film cooled sections. Several procedures were used to obtain the best possible results. Most of the settings were chosen following the advice of the Fluent<sup>®</sup> manual.

Fluent<sup>®</sup> read the case file and checked the grid. Smooth/swap operations (using the skewness option) ran several times, ending with a smoothing operation. The domains were swapped using the reverse Cuthill-McKee method. At this point the boundary conditions were applied to the grid, along with periodic adaptation. Starting with Fluent<sup>®</sup> 6.0, the use of periodic boundary conditions no longer carries the requirement that the grid be identical across both periodic planes. Fluent<sup>®</sup> linked the periodic planes using the non-conformal boundary routine. This means the 90° wide gridded model encompasses 360° of physical space, thus using 25% of the computational time. The grid was partitioned for parallel processing using the METIS algorithm [70], which attempts to minimize interface area between partitions for faster processing using multiple nodes.

The fluid inflow boundary conditions were set as mass-inflow, specifying mass flux and temperature. This is the same boundary condition setup used for the coolant channels. The pipe outflow used a pressure-outlet boundary condition. These conditions are appropriate for compressible flow problems, and allow one to easily set the blowing ratio via Eq. 10 (p. 11). At this point the grid was ready for computation.

The Fluent<sup>®</sup> manual specified input parameters for similar problems. Options for the pressure-based, Green-Gauss-node-based, and gradient-set solution method were set. Enhanced wall treatment, including thermal and pressure gradient effects was activated, as is appropriate for wall jet problems [71]. Table 3 shows the default closure coefficients for the *realizable*  $k-\epsilon$  turbulence model all of the simulations used.

The solutions used a second order discretization. Residual tolerances for continuity, x, y, and z momentum, energy, k, and  $\epsilon$  were all set to  $1 \times 10^{-6}$ .

*Turbulence Model.* All of the CFD runs used the *realizable*  $k - \epsilon$  turbulence model. There is a big difference between  $k - \epsilon$  and its *realizable* counterpart. A detailed derivation of the model is available by Shih [72]. Simply, the new model keeps the normal stresses from going below zero, a nonphysical (*un-realizable*) situation that sometimes arises in the original  $k - \epsilon$  model. The new model:

- resolves what is known as the wall-jet anomaly by solving the flow for Cartesian jets as well as axisymmetric ones;
- is free of a  $k$ -dependent singularity in the destruction term for turbulent dissipation,  $\epsilon$ ;
- performs better than  $k - \epsilon$  for free flows with jets and mixing, boundary layer flows, and separated flows;
- prevents the un-realizable condition whereby Reynolds stresses may be calculated as negative.

While the  $k - \omega$  model has been shown to perform well for wall-bounded flows and curved grids, the film cooling problem is essentially a jet in cross-flow, so the *realizable*  $k - \epsilon$  model is most appropriate. Several film cooling researchers [71, 73, 74] have shown  $k - \omega$  vastly over-predicts adiabatic effectiveness when compared to experiment, mostly due to its incorrect calculation of the jet spreading rate. At least one study [75] used the *realizable*  $k - \epsilon$  model to predict cooling performance on a stream-wise curved surface with excellent agreement to experiment. Like the study presented here, an unstructured mesh with prismatic boundary layer growth was used to predict performance. Thus proven most suitable for this type of problem, and in the absence of experimental data for this geometry, the *realizable*  $k - \epsilon$  was used.

*Grid Convergence.* A grid convergence study showed that a grid of  $\approx 3 \times 10^6$  cells would provide a grid-independent solution. the metric used to determine grid

Table 3: Closure Coefficients Used In The *Realizable*  $k - \epsilon$  Model

$C_{2,\epsilon}$	1.9
$Pr_{TKE}$	1.0
$Pr_{TDR}$	1.2
$Pr_\epsilon$	0.85
$Pr_{wall}$	0.85

convergence was span-wise averaged adiabatic effectiveness,  $\eta_{\overline{span}}$ . Convergence was determined by doubling the number of cells, mostly in the region near the hole, until less than a 1% change was observed in the metric.

### 3.3 Results of Radial Concave Curvature Simulations

The overall trends in each of the cases followed those previously discovered in film cooling studies: with increased  $F$ , cooling efficiency increased up to a certain point. After a distance downstream of the hole at which the jet began to exhibit blow-off behavior, the differences between the flat plate case and the curved wall cases began to grow. The curved wall kept the jet more attached, even as the jet width decreased due to wall cradling, causing span-wise averaged adiabatic effectiveness to slightly increase downstream.

*Adiabatic Effectiveness.* Figure 7(a) shows a contour plot of adiabatic efficiency of the flat plate case with  $90^\circ$  compound angle injection, while Fig. 7(b) shows the same for the case with the most curvature ( $D_\infty/D_j = 33.12$ ). At low  $F$ ,  $C$  becomes relatively large. The curvature effects are apparent in these figures. Notice how the flat plate jet spreads quickly as it travels downstream, while the curved wall jet contours are much longer and stretched out even 10 diameters from hole center. Jet elongation is an example of a cradling effect whereby the presence of a curved wall prevents the lateral spreading of the coolant jet, and through continuity more of the jet remains at the wall for a longer distance downstream.

Span-wise averaged adiabatic effectiveness,  $\eta_{\overline{span}}$ , is plotted for all four  $90^\circ$  compound angle injection wall configurations at  $F = 0.7$  in Fig. 8(a). The point of

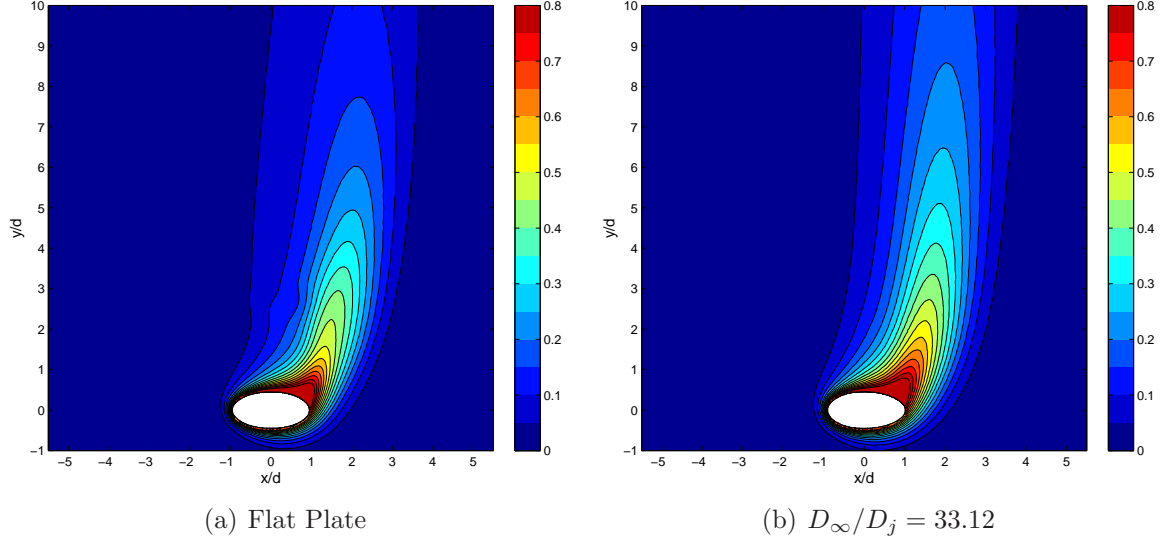


Figure 7: Contour plots of adiabatic effectiveness,  $F = 0.5$

maximum curvature in  $\eta_{\overline{span}}$ , which occurs around 1-2 hole diameters downstream of the hole, is shifted to the upper right as  $C$  increases. This shift is evidence of the stretching of the coolant jet and the improved attachment due to curvature which results in an overall *increase* in  $\eta$  out to 10 diameters and beyond. There are several reasons for this, two of which are the decreased surface area between the coolant jet and the free-stream flow which results in less overall mixing and the wall preventing the lateral spreading and mixing of the jet.

Figure 8 shows the same configuration for two simulated blowing ratios. As the wall curvature increases,  $D_\infty/D_j$  decreases, and  $\eta_{\overline{span}}$  increases as well. Fig. 9 shows the results of all runs at a variety of blowing ratios in terms of radial curvature parameter. As  $C$  decreases, the point of maximum curvature in  $\eta_{\overline{span}}$  moves further to the lower left without the downstream recovery in  $\eta$  generally seen at higher blowing ratios on flat plates.

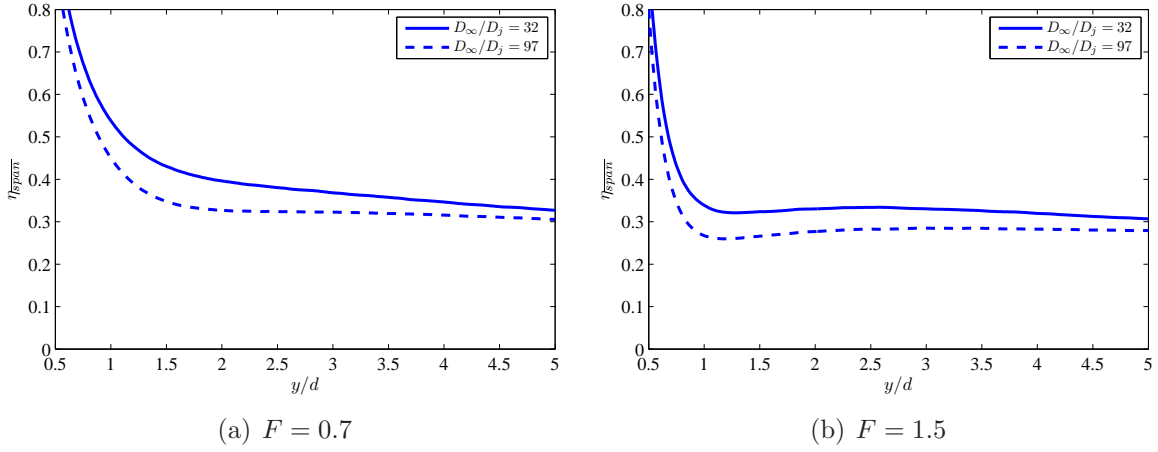


Figure 8: Simulation of span-wise averaged adiabatic effectiveness,  $\eta_{\overline{span}}$ , for  $90^\circ$  compound injection.

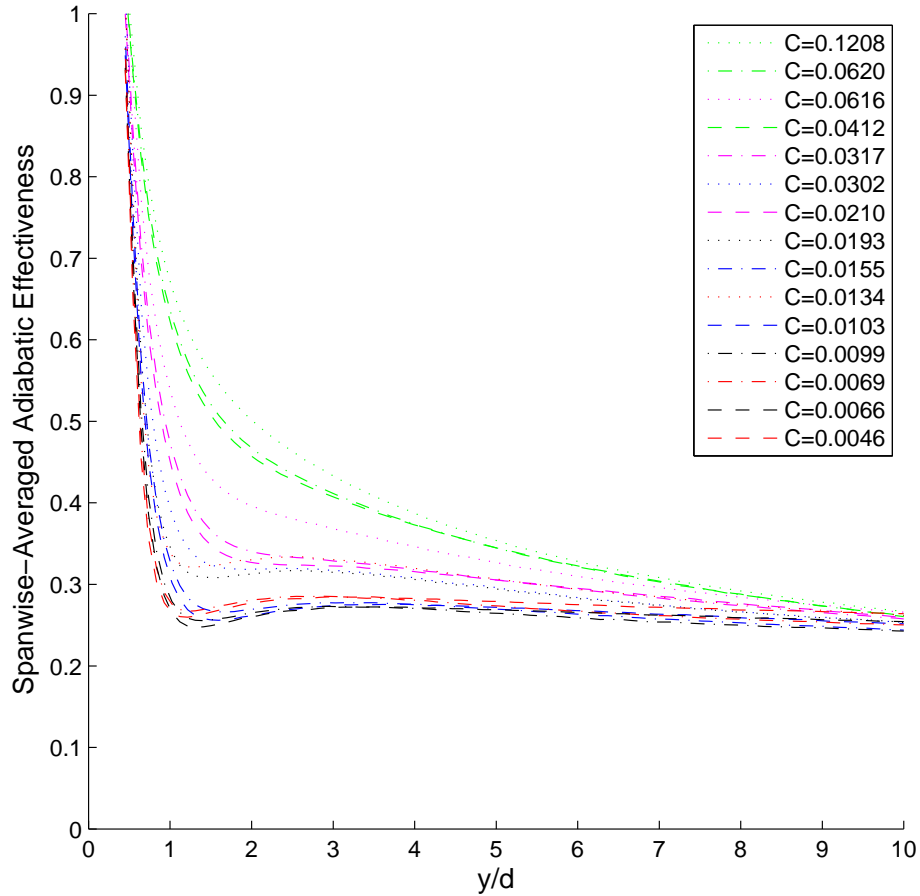


Figure 9: Span-wise averaged adiabatic effectiveness for  $90^\circ$  compound injection at a variety of  $C$  values

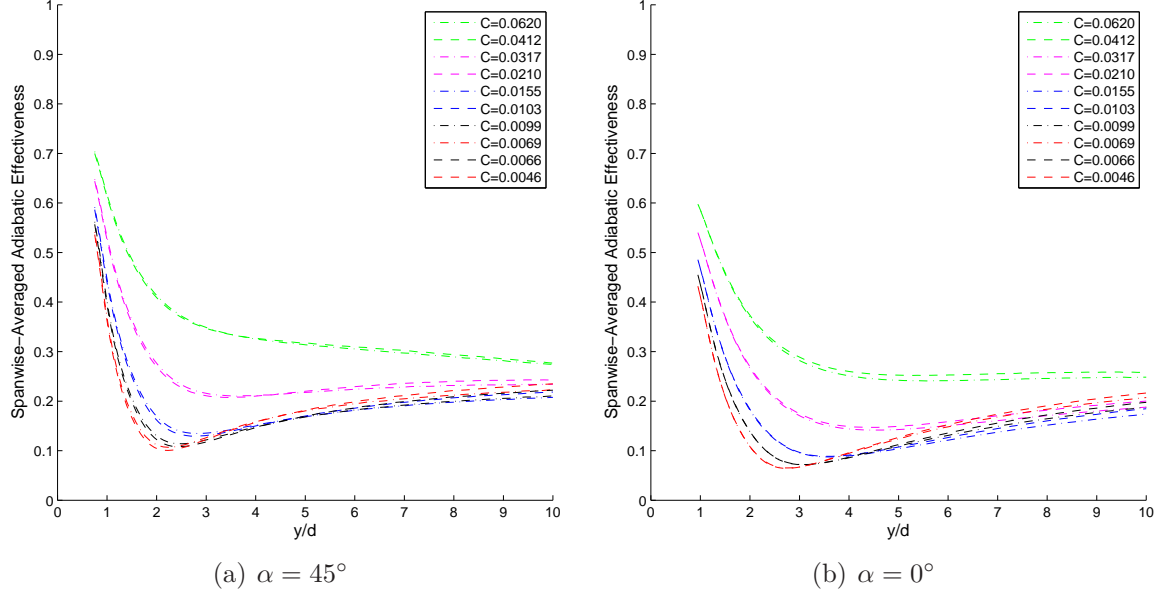


Figure 10: Simulation of span-wise averaged adiabatic effectiveness for different compound injection angles at a variety of  $C$  values.

*Compound Injection Angle.* High compound injection angle cases exhibit the most effects from radial curvature because the jet velocity component in the span-wise direction, the direction of curvature, is at it's highest. However, changes are still observed at lower compound angles, and even in configurations with no compound injection. Fig. 10(a) shows the cases with  $45^\circ$  compound injection angle. As  $C$  decreases (mostly from an increase in  $F$  in these tests) the difference between similarly-colored lines (which represent the same blowing ratio at different curvatures) becomes more pronounced. Nowhere is the difference due to curvature as pronounced as the  $90^\circ$  cases.

For the case of no compound injection (Fig. 10(b)), the jet velocity has no component in the transverse direction so the curvature effects seen earlier are no longer observed. Instead, as  $F$  increases the curves become closer for different wall diameters. This is because at low  $F$  the jet adheres closer to the wall and is slightly cradled from the radial curvature. As  $F$  increases, more of the jet is lifted off of the wall, and the impingement point (or reattachment region) seems unaffected by the radial curvature.

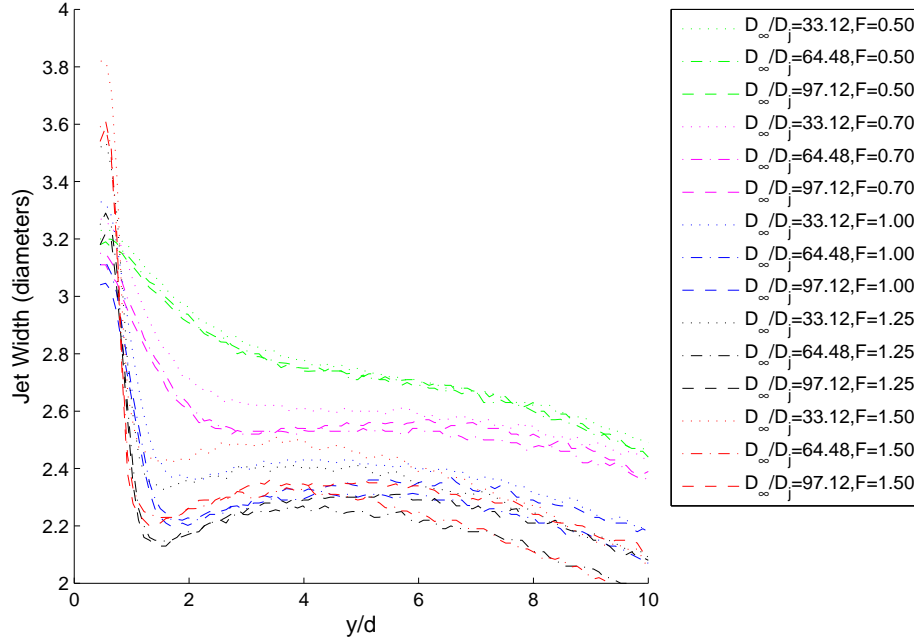


Figure 11: Comparison of jet widths for 90° compound injection at a variety of  $C$  values.

*Jet Geometry.* Another change in the behavior of the jet at the wall is found in the jet width. Span-wise averaging the adiabatic effectiveness is equivalent to integrating effectiveness over the width of the jet. So a wide jet with low effectiveness may yield the same average effectiveness as a thin jet with high effectiveness throughout. Figure 11 shows as the wall radius decreases the jet width decreases, especially at higher blowing ratios. Logically, if the jet affects less area but  $\eta_{\overline{span}}$  is higher (from Fig. 8) then adiabatic effectiveness must be higher.

More of the coolant is kept closer to the wall for a longer period, so mixing is decreased at low  $F$ . However, the benefits at higher  $F$  are still lost when compared to the flat plate. This is a drawback of the stretched jet; not as much of the surface benefits from the coolant. It is inefficiently distributed over a relatively smaller area. Thus, if higher blowing ratios are desired on radially curved wall, the hole pitch must be decreased for the same  $\eta$  for flat plate relations to be valid.



*Net Heat Flux Reduction.* It is difficult to directly compare the results of net heat flux reduction (NHFR) simulations since the variables of interest are inherently 2-D. The desired quantity is the heat flux reduction to the wall due to film cooling. Therefore the heat flux reduction must be averaged over the entire wall as in:

$$\overline{\Delta q_r} = \frac{1}{A} \iint \Delta q_r dA \quad (65)$$

The area-average is achieved by downstream-averaging the span-wise average of NHFR. Remember NHFR is defined as

$$\text{NHFR} = 1 - \frac{h_f}{h_o} \left( 1 - \frac{\eta_f}{\phi} \right) \quad (24)$$

However, as pointed out by Rutledge et al. [76], the span-wise average of NHFR is *not* simply the NHFR calculated with average  $h_f$  and  $h_o$ . Instead, a span-wise averaged form of Eq. 24 must be used:

$$\overline{\Delta q_{r,span}} = 1 - \frac{\int_{-\Delta x}^{\Delta x} h_f (\phi - \eta) dx}{\int_{-\Delta x}^{\Delta x} h_o \phi dx} \quad (66)$$

Applying the above equation for area averaging NHFR results in

$$\overline{\Delta q_{r,area}} = 1 - \frac{\int_{-\Delta x}^{\Delta x} \int_{-\Delta y}^{\Delta y} h_f (\phi - \eta) dx dy}{\int_{-\Delta x}^{\Delta x} \int_{-\Delta y}^{\Delta y} h_o \phi dx dy} \quad (67)$$

Equation 67 is used to obtain the area-averaged NHFR. The area of integration is a function of the pitch  $P$ , or distance between coolant holes in hole diameters. For this study, the area of integration is equal to the area shown in the contour plots beginning on p. 57. In other words  $-5.5 < x < 5.5$  (span-wise) and  $-1 < y < 10$  (downstream), where  $x$  and  $y$  are in hole diameters. The hole pitch for a perforated

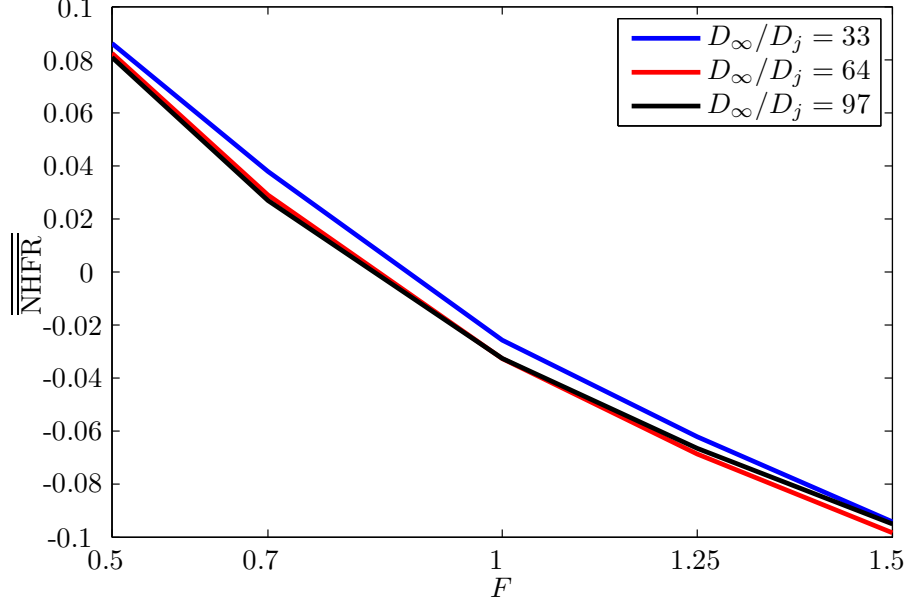


Figure 12: Comparison of NHFR for all three  $D_\infty/D_j$  values at the tested blowing ratios

plate can be determined using a numerical method [77] comparing desired performance in an ideal transpiration cooling scheme with expected performance from a perforated plate.

Figure 12 shows a total comparison of NHFR for all  $90^\circ$  compound injection cases. Area-averaged NHFR is plotted versus blowing ratio. The differences in NHFR are quite small, which is expected because the differences in  $\eta$  are also small. There appears to be a near constant elevation in NHFR as curvature increases, and interestingly the  $D_\infty/D_j = 97.12$  and  $D_\infty/D_j = 64.48$  cases are nearly identical. However, the  $D_\infty/D_j = 33.12$  performs slightly better than the other two at all blowing ratios. Figures 13-17 help to show why there is a performance increase.

The NHFR results of the computational study for  $F = 0.5$  and  $F = 0.7$  are shown for the  $90^\circ$  compound injection angle cases in Figs. 13 and 14. There are obvious differences between the different  $D_\infty/D_j$  values. First, the affected areas, or areas of highest NHFR occur over a thinner region at lower  $D_\infty/D_j$ . Second, the area of low NHFR directly downstream of the hole is slightly more pronounced at lower

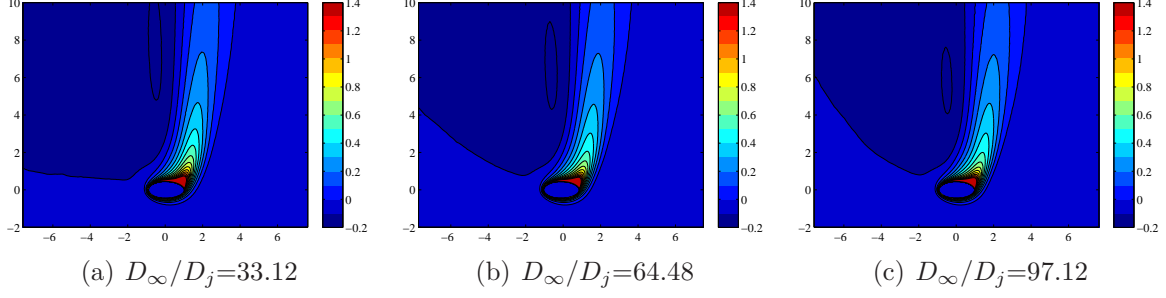


Figure 13: Contour plots of NHFR for the 90° compound injection angle cases at blowing ratio of  $F = 0.5$

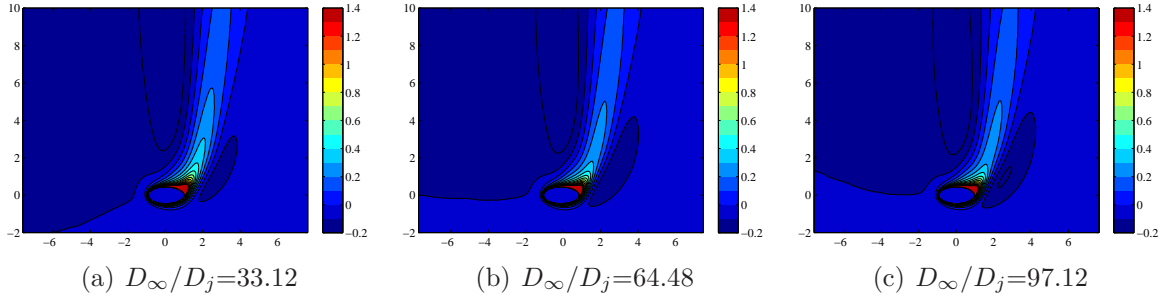


Figure 14: Contour plots of NHFR for the 90° compound injection angle cases at blowing ratio of  $F = 0.7$

$D_\infty/D_j$ . Third, the NHFR stays higher for longer downstream in the lowest  $D_\infty/D_j$  case than the others.

The NHFR results of the computational study for  $F = 1.0$ ,  $F = 1.25$ , and  $F = 1.50$  are shown for the 90° compound injection angle cases in Figs. 15, 16, and 17. The only difference between these figures and Figs. 13 and 14 is the blowing ratio is increased, crossing the  $I = 1$  threshold where jet behavior dominates free-stream behavior. As anticipated, the differences between the low  $D_\infty/D_j$  and higher values are more pronounced, as the jet now drives the film cooling behavior. The impingement of the jet on the wall in the direction of radial curvature helps to coat more of the wall downstream of the hole. Also there is less area of the coolant jet exposed to free-stream air which limits diffusion of the coolant.

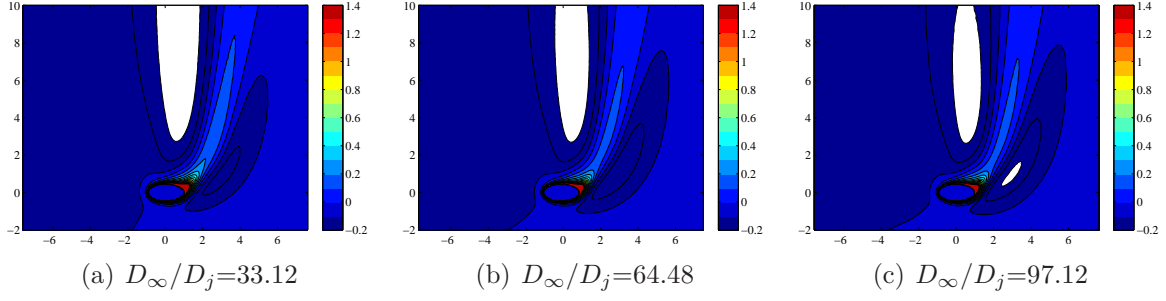


Figure 15: Contour plots of NHFR for the  $90^\circ$  compound injection angle cases at blowing ratio of  $F = 1.0$

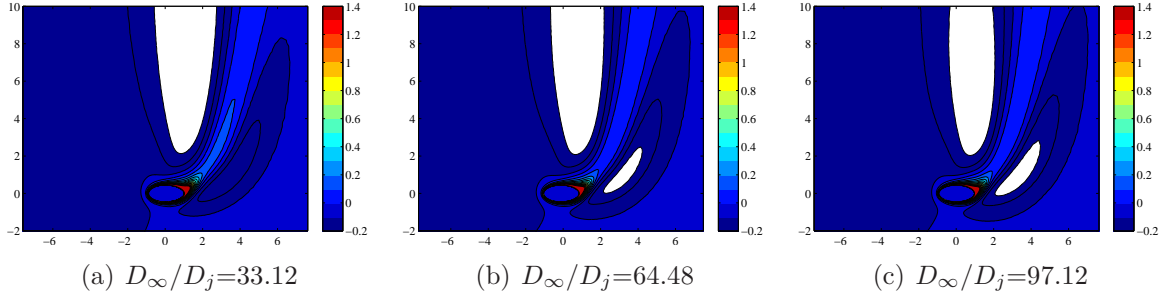


Figure 16: Contour plots of NHFR for the  $90^\circ$  compound injection angle cases at blowing ratio of  $F = 1.25$

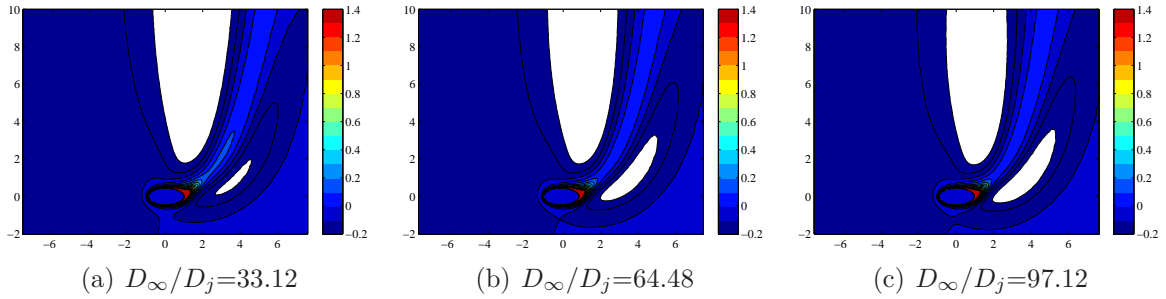


Figure 17: Contour plots of NHFR for the  $90^\circ$  compound injection angle cases at blowing ratio of  $F = 1.50$

### 3.4 *Summary*

The simulations discussed in this chapter showed three things: first, that the behavior of full-coverage film cooling (FCFC) approaches that of transpiration cooling as the hole pitch decreases for a constant coolant mass flow and varies quadratically as a function of coolant flow area; second, as radial curvature increases, so does span-wise averaged adiabatic effectiveness for a given blowing ratio up to and beyond 10 hole diameters; third, NHFR increases with increased radial curvature at all tested blowing ratios. The experiments to be presented verify these trends, though at different  $Re$  and turbulence intensity.

## IV. Experimental Method to Determine Effects of Radial Curvature

Many factors affecting film and transpiration cooling have been identified thus far. Their interactions are frequently coupled and complicate the prediction of cooling performance. Of the many factors impacting film cooling performance, free-stream turbulence, surface curvature, blowing ratio, and hole shape tend to have the most profound influence [5]. In many rocket combustion chambers, the free-stream turbulence is a result of the combustion process, and surface curvature may not be modified to accommodate cooling performance improvements because of weight constraints. Radial curvature usually cannot be changed at all, though the axial pressure gradient (or slope of combustion chamber contraction) may be adjusted with some freedom, provided the combustion chamber remains large enough to allow complete combustion.

### *4.1 Simultaneous Acquisition of $T_{aw}$ and $h$*

A transient method of recording surface temperature yielded the information necessary to determine the adiabatic effectiveness and net heat flux reduction (NHFR) for a variety of run conditions. The derivation of the technique is straightforward. A solid is assumed to have one-dimensional (1-D) conduction in the direction normal to the surface. Assuming isotropic thermal conductivity and uniform density and specific heat capacity, the heat equation is simply

$$\frac{\partial^2 T}{\partial z^2} = \frac{1}{\alpha} \frac{\partial T}{\partial t} \quad (68)$$

where  $T$  is the temperature anywhere in the solid,  $t$  is time,  $\alpha$  is the thermal diffuseness, and  $z$  is the distance into the solid from the surface. The boundary condition for flow parallel to the surface ( $z = 0$ ), assuming a constant free-stream temperature

and heat flux coefficient, is

$$-k \left. \frac{\partial T}{\partial z} \right|_{z=0} = h [T_{aw} - T(0, t)] \quad (69)$$

where  $k$  is the thermal conductivity and  $T_{aw}$  is the adiabatic wall temperature. The initial condition is

$$T(z, 0) = T_i \quad (70)$$

where  $T_i$  is the initial, *uniform* temperature throughout the solid at all points. Solving Eq. 68 in the method prescribed by Kays and Crawford [7], and recognizing the surface temperature is the only temperature of interest (in other words, evaluating at  $z = 0$ ), the solution is

$$\frac{T_s - T_i}{T_{aw} - T_i} = 1 - \exp\left(\frac{h^2 \alpha t}{k^2}\right) \operatorname{erfc}\left(\frac{h \sqrt{\alpha t}}{k}\right) \quad (71)$$

The non-dimensional temperature  $\frac{T_s - T_i}{T_{aw} - T_i}$  varies with non-dimensional time  $\frac{h^2 \alpha t}{k^2}$  in the prescribed fashion. Figure 18 shows how measurements of the independent variables (surface temperature  $T_s$  and times  $t$ ), with knowledge of certain constants ( $T_i$  and the material properties  $\alpha$  and  $k$ ), allow one to determine the dependent variables (adiabatic wall temperature  $T_{aw}$  and the local heat flux coefficient  $h$ ). These in turn allow one to directly calculate adiabatic effectiveness,  $\eta$ , and net heat flux reduction (NHFR) at each pixel. This solution is not novel and dates back to at least the 1950's. The method has been used several times, most recently by researchers at the Air Force Research Laboratory (AFRL) [78]. Their method used two temperature measurements via infrared (IR) camera at two times to determine  $T_{aw}$  and  $h$ .

The research presented here includes some improvements made to this technique, which are presented in Sec. 4.4 (p. 72). Details on the experimental method can be found in Sec. 4.5 (p. 76). What immediately follows is a detailed design of experiments (DOE) methodology.

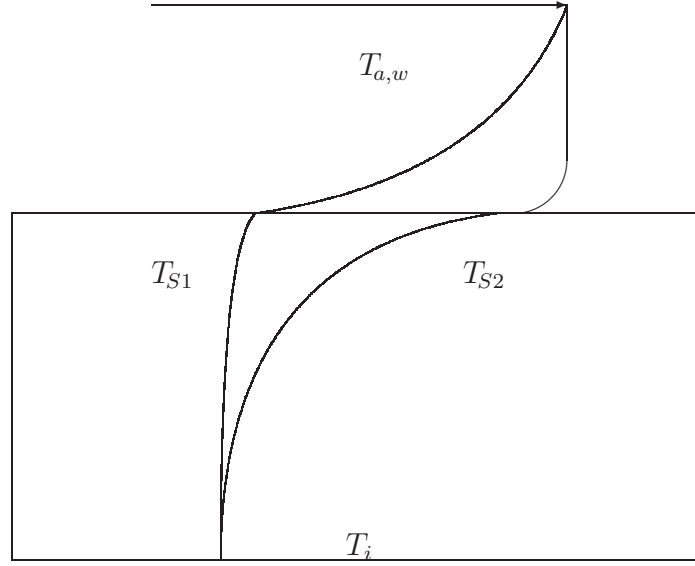


Figure 18: Transient heating process on a semi-infinite slab. Free-stream flow travels left to right and transfers heat downward to the surface through convection.  $T_{S1}$  and  $T_{S2}$  are the surface temperatures at times  $t_1$  and  $t_2$  and are the quantities measured in the transient technique.  $T_i$  is not only the initial temperature of the slab but also the temperature at a point sufficiently far from the surface at all times.

#### 4.2 *Design of Experiments Methodology*

In any experiment there are variables, measured as output, affected by changing one or more process variables. Response (output) variables in this investigation are measured quantities from the gas and wall. Key process variables are those variables which are intentionally changed to produce some change in the output variables. Control variables are those remaining constant between experiments, and their effects on response variables are considered nil. Noise variables (like turbulence in this case) can change response variables in ways not directly attributable to key process variables and introduce uncertainty and variability into the results; their effects should be minimized as much as possible to increase the validity of the results. Identifying each class of variables and investigating their interactions is part of the DOE system.



To solve Eq. 71 for the desired value of adiabatic effectiveness,  $\eta$ , requires measurements of the initial surface temperature,  $T_i$ , the surface temperature  $T_s$  at many times  $t$ , and knowledge of the thermal material properties of the test article.

*Response Variables.* Though the output of this research is displayed in terms of cooling effectiveness, response variables are those which will be measured and observed. They are wall temperature, time, and gas temperature and velocity (both in the coolant hole and free-stream). These variables will then be manipulated to produce the cooling effectiveness.

**Wall Temperature** - infrared (IR) thermography was used to measure the temperature of the wall directly. Normally the camera calibration would be used to obtain the actual wall temperature, taking into account humidity, emissivity of the surface, and air temperature. To increase the precision and accuracy of the measurements, a curve fit was generated from a set of calibration images which made use of direct thermocouple measurements. Details on the calibration and curve fit are in the appendix (p. 134).

**Time** - The clock on-board the IR camera measured the time. It was accurate to within  $\pm 0.5\text{ ms}$  and was recorded in the data files. There was an unknown error in the start-up time that was unavoidable given the experimental setup. A method for quantifying and removing this error is shown in Sec. 4.4 (p. 75).

*Key Process Variables.* The key process variables are those intentionally modified to stimulate changes in the output variables. Compound injection angle, axial pressure gradient, free-stream hot gas temperature and composition (through combustion), radial curvature, and blowing ratio will all be varied.

**Radial Curvature** - Radii of axial curvature are chosen based on the curvature ratios expected in rocket combustion chambers. To make manufacturing of the test articles simpler and cheaper, nominal sizes of schedule 40 pipe are chosen.

The ratio of hole diameter to wall diameter is determined by changing the hole size for coupons with the same radius. Five different wall to hole diameter ratios,  $D_\infty/D_j$  were used in this experiment.

**Compound Injection Angle** - Compound injection generally has a beneficial impact on film cooling effectiveness. The transverse component of injection velocity tends to coat more of the surface near the hole. Since the coolant decay is not strongly affected, more of the surface is coated by the same amount of coolant. Two compound injection angles were chosen,  $\alpha = 0^\circ$  and  $\alpha = 90^\circ$ .

**Pressure Gradient** - A favorable pressure gradient is what causes flow to accelerate, and is usually due to a contraction in the available flow area. Conflicting results are reported for the effect of pressure gradient on film cooling effectiveness. No experimental results appear available for strong favorable pressure gradient effects on transpiration cooling effectiveness. An axial pressure gradient is expected to have an effect analogous to wall curvature on cooling effectiveness, including a dependence on momentum ratio. At low blowing ratios ( $F < 1$ ) a strong favorable pressure gradient tends to decrease performance, and at higher blowing ratios ( $F > 1$ ) it increases performance [49]. To determine the magnitude of the pressure gradient tested, the common definition of the acceleration parameter is used (p. 27):

$$K = \left( \frac{\nu}{u^2} \right) \frac{du}{ds} \quad (36)$$

and for this experiment  $K = 2.1 \times 10^{-5}$ .

**Blowing Ratio** - Five blowing ratios were tested. The blowing ratio, or mass flux ratio, has a strong correlation to cooling effectiveness. Velocity measurements are necessary to determine at what blowing ratio the experiment is being run. Velocities are backed out of direct measurements of mass flow made by control-feedback devices, measurements of the cross-sectional area of the flow, and measurements of the temperature of the coolant and free-stream gasses. While the free-stream velocity is a control variable, the coolant velocity is

changed to achieve a desired blowing ratio. The blowing ratios at which the experiments were run were calculated from measurements of the gas temperatures and bulk mass flows, with knowledge of the molecular weights of both the coolant and free-stream gasses.

**Coolant Species** - Some of the experiments used  $CO_2$  as the coolant instead of air. This allowed the density ratio to go from 1.1 to 1.8. While this is not outside the range of density ratios already tested, it is a necessary configuration for determining if there are any other effects due to curvature at higher density ratios.

*Control Variables.* The control variables are those remaining constant between experiments, and their effects on the output variables are considered nil. These variables are usually ones outside the scope of investigation, ones with well understood effects on the response variables, or ones that may have an unknown but uninteresting effect. The control variables in this experiment are coolant temperature, fuel composition, injection angle (to the stream, not compound), and hole geometry (area and shape).

**Free-stream Hot Gas Conditions** - Discerning cooling effectiveness from un-cooled and cooled test runs is difficult if the temperature difference between the coolant and the hot free-stream gas is small. Furthermore, the amount of coolant dispersed to the free-stream may be a function of the coolant-free-stream temperature difference, as extreme temperature gradients yield velocity flow-field effects. The free-stream temperature and velocity were controlled by control-feedback devices which kept the temperature within  $0.1\text{ K}$  and Reynolds number ( $Re$ ) to  $31\,000 \pm 200$ .

**Injection Angle** - In general, cooling performance is enhanced by injecting the coolant at a shallow angle to the wall. Injection angle is often constrained by manufacturing and structural limits. Typically, it is no more shallow than  $60^\circ$  from surface normal at the hole location (commonly referred to as  $30^\circ$  from

downstream). While the formed platelet manufacturing process is surely capable of creating shallower injection angles, there is still the opportunity for pieces to break off in the presence of temperature and pressure fluctuations with very shallow angles. Therefore, the coolant will be injected at  $30^\circ$  from downstream.

**Hole Geometry** - Cylindrical holes were used in every coupon and each had a  $30^\circ$  injection angle and  $0^\circ$  and  $90^\circ$  compound injection angles. The coolant flowed from a plenum through a channel 10 hole diameters long, and exited at the surface of the coupon. The holes were not fanned.

*Noise Variables.* Noise variables introduce error into the measurement of the response variables. Great effort should be taken to minimize their effects during experimental design. Ironically, much of the noise comes from the experiment itself, since every measurement technique has some error associated with it. The anticipated sources of noise for this experiment are free-stream turbulence, coolant temperature drift, and testing method noise.

**Coolant Temperature** - Coolant temperature was not constant, though every effort was made to keep it constant. Unavoidably, the coolant temperature immediately before the hole exit is changing with time because the coolant is absorbing some heat from the adjacent wall. A method by which the temperature was corrected in every frame reduced the effect of a gradually wandering coolant temperature. This method is presented in Sec. 4.4 (p. 73).

**Turbulent Intensity** - Turbulence is necessary to rocket combustion because it assists in mixing the fuel and oxidizer. It also contributes to the combustion itself. A large amount of free-stream turbulence is expected in a combusting environment. In an ideal experiment the turbulence intensity should be kept as constant as possible. Since it can't be directly controlled, it is imperative to measure the turbulence intensity, though any unavoidable variations may lead to qualitative insights into the effects of turbulence on effectiveness. Turbulence intensity  $Tu$  was measured with hotwire anemometry as  $Tu \approx 26\%$ , a value

typical of combusting environments, and higher than any previously tested film cooling setups. See Sec. 4.3 (p. 70) and the appendix (p. 129) for information on the measured turbulence statistics.

### **4.3 Test Rig Design**

The test rig was designed with the intent it would be used to run combustion tests for future studies. Seven coupons were fabricated out of closed-cell, engineered polyurethane foam, the properties of which are available in the Appendix (p. 128). These articles were placed in a test stand capable of delivering free-stream fluid of differing temperature, composition, and pressure gradient. Blowing ratio was controlled through a mass flow controller which pressurized a plenum inside the test article.

A simple test setup was necessary to ensure minimal sources of error. Further, a modular design ensured more tests could be run to maximize the number of process variable investigations. Stainless steel was chosen as the rig material for its resistance to oxidation, high temperature limit, and high strength. Three large windows may be placed on the rig to allow laser and camera access while combusting, though these are unnecessary for non-combusting tests. The test rig as designed is shown in Fig. 19 (p. 68). All tests presented in this document were run using air as the free-stream fluid and air as the coolant, except for a set of tests which used  $CO_2$  as coolant to provide some high density ratio (DR) data points.

The Combustion Optimization and Analysis Laboratory (COAL) is a facility at the Air Force Institute of Technology (AFIT) originally designed for testing the Ultra Compact Combustor (UCC). Capable of delivering hot air and fuel, combustion in the test articles can be measured with one or more of several laser diagnostic systems, including Coherent Anti-Stokes Raman Spectroscopy (CARS) and Planar Laser-Induced Fluorescence (PLIF). Details on the construction and capabilities of the rig can be found in a thesis by Anderson [79] It is capable of delivering air at up to  $530\text{ K}$  at  $120\text{ g/s}$ . Fuel (in this case, kerosene) can be delivered at  $5.67\text{ ml/s}$ . Kerosene has a density of  $805\text{ kg/m}^3$ , so the maximum mass flow for kerosene is  $4.56\text{ g/s}$ . The



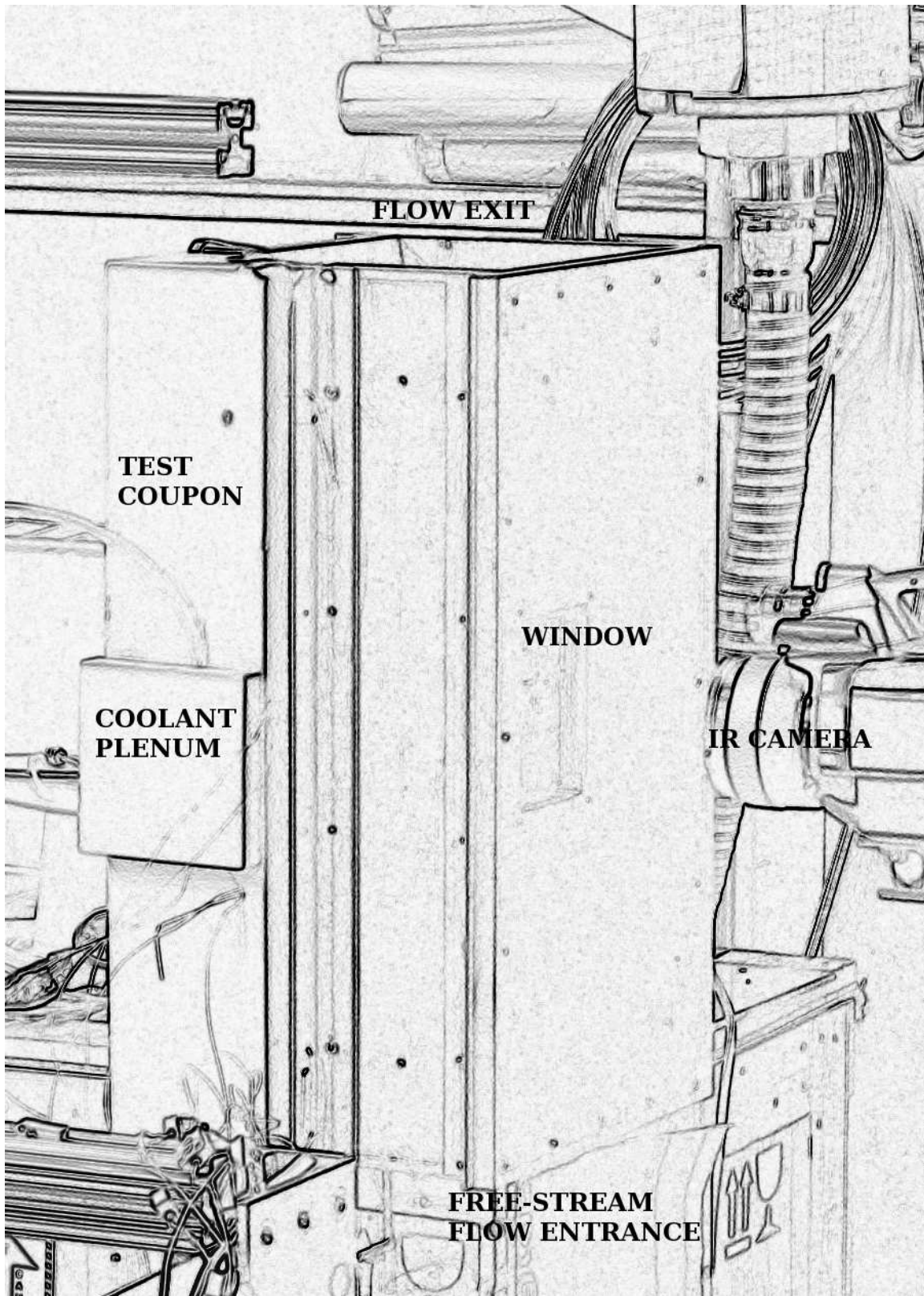


Figure 19: Physical testing apparatus. This test setup was used to gather all of the experimental data presented in this study.

stoichiometric oxidizer to fuel ratio  $(O/F) = 2.56$  for the oxygen/kerosene reaction, so the stoichiometric mass flow of air and kerosene into the combustor is  $60.2\text{ g/s}$ . More air than this and the combustion temperature will change, but the film coolant kerosene may ignite due to the presence of un-reacted oxygen in the free-stream. Less air than this and the combustion temperature will be lower and the free-stream composition more representative of the conditions inside real rockets. An ethylene pulse torch may be used to ignite the mixture.

Though no combustion experiments were run in the course of this effort, the rig is capable of combustion. The laser measurement systems in the COAL utilize a Neodymium-doped Yttrium Aluminum Garnet (Nd:YAG) laser. For diagnostics, the laser emits a beam of light with certain desirable characteristics, such as frequency, frequency spread, power, time duration, and repetition rate. Details on this particular laser system can be found in Anderson's thesis [79]. Using this laser, several optical measurement techniques, like those explained by Eckbreth [80], are possible. After some mixing studies, combustion studies should be performed to observe the performance impacts of film cooling on the overall specific impulse ( $I_{sp}$ ) of a theoretical rocket. More recommendations will be listed in Chap. VI.

*Test Article Production.* Obtaining the necessary data to fill out the design space listed in section 4.2 requires several test articles of different geometries. Two different radial curvatures were tested, one at  $102\text{ mm}$  (corresponding to the inner diameter of schedule 40,  $4\text{ in}$  pipe) and the other at  $154\text{ mm}$  (corresponding to the inner diameter of schedule 40  $6\text{ in}$  pipe). The ratio of diameters between the free-stream and coolant flows was simply designated  $D_\infty/D_j$ . Seven articles were built, one for each  $D_\infty/D_j$  to be tested; five of them were at a compound injection angle of  $90^\circ$  and two were at  $0^\circ$ . There were different coolant hole sizes in each coupon, resulting in different values for  $D_\infty/D_j$ , as listed in Table 4 (p. 78).

The test articles, or coupons, were made of Last-a-Foam, a closed-cell polyurethane foam with an engineered density of  $6\text{ lbm/ft}^3$ , some properties of which are listed in

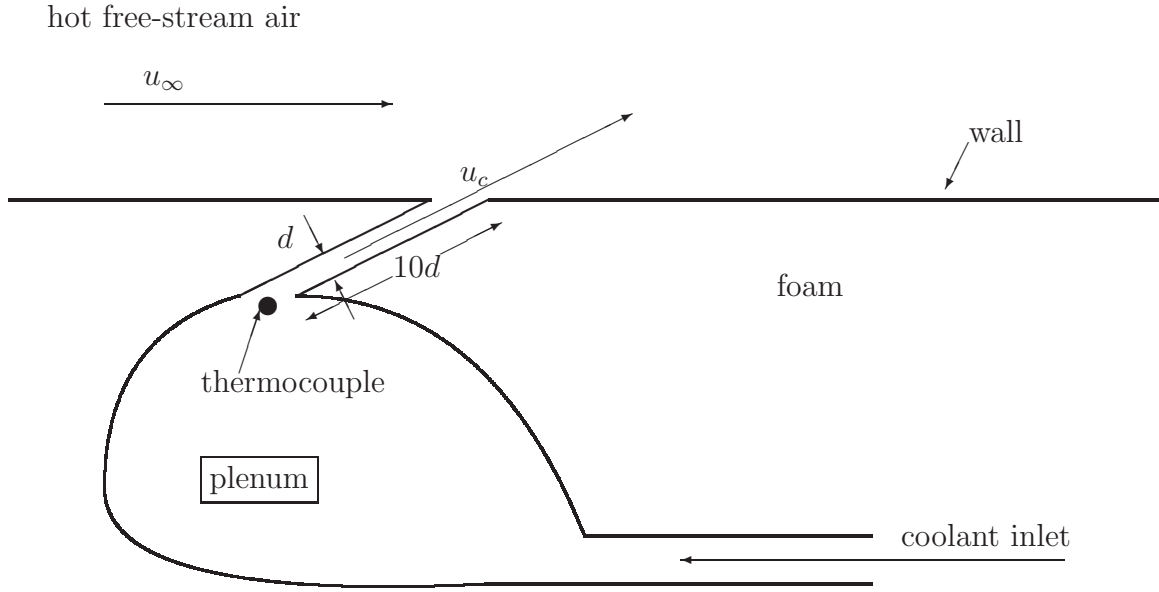


Figure 20: Conceptual drawing of plenum construction. The hole diameter is  $d$ .

the appendix (p. 128). Each coolant hole was drilled in the coupon at a precise angle ( $30^\circ$  injection,  $90^\circ$  compound injection at the surface) and to a depth of ten hole diameters. A plenum was then placed inside the coupon, conceptually shown in Fig. 20. Plastic tubing ( $3.2\text{ mm}$  inner diameter) supplied the coolant directly from the mass flow controller and was inserted into the plenum.

Several K-type thermocouples were needed for this experiment, each made by the author from the same spool of 38-gauge wire. They were calibrated according to the procedure in the appendix (p. 134). The welded beads were pressed flat for surface temperature application, and left spherical for gas measurements. Two thermocouples were installed on each coupon: one to measure the coolant temperature, and one to measure the surface temperature. Each coupon was allowed to reach a steady state, uniform temperature before testing began.

*Pressure Gradient Induction Method.* A favorable pressure gradient is what causes flow to accelerate, and is usually due to a contraction in the available flow



area. To induce a stream-wise favorable pressure gradient, a wedge was mounted to the flat wall opposite the curved test section, as in Fig 5 (p. 27). The dimensionless pressure gradient parameter  $K$  (Eq. 36, p. 27) induced by this wedge was calculated as  $2.1 \times 10^{-5}$ . The free-stream gas velocity at the hole location was the same regardless of the presence of the wedge. In other words, the free-stream total mass flow was lower with the wedge in than without. This means that for a given blowing ratio, the coolant velocity was the same in either condition.

Inducing the pressure gradient in this manner had a large effect on the free-stream turbulence. When the wedge was not present, the turbulent intensity was  $Tu \approx 0.26$ . When the wedge was present,  $Tu \approx 0.11$ . The integral length scale,  $\Lambda_l$ , likewise was greatly reduced in the presence of the wedge, dropping from  $\Lambda_l \approx 56 \text{ mm}$  to  $\Lambda_l \approx 38 \text{ mm}$ . Among the reasons for this change in turbulent character are the reduced total flow rate and the presence of a strong favorable pressure gradient, both due to the wedge.  $\Lambda_l \approx 56 \text{ mm}$  is expected since the opening through which the flow passes at the entrance to the test section has a diameter of  $50.4 \text{ mm}$ . The change in  $\Lambda_l$  is nearly equal to the change in area due to the wedge, so it is likely the length scales were compressed as the flow was compressed traveling past the wedge. More turbulence statistics are available in the appendix (p. 129).

*Density Ratio Induction Method.* A few studies of the effect of density ratio (DR) have already been accomplished up to about  $DR = 2$ . It is important to investigate this regime, and higher values of DR if possible, for radially curved environments since rockets operate well past this value. To induce a DR without large temperature differences, carbon dioxide ( $CO_2$ ) was used as a coolant for some tests. This means the coolant velocity was lower than when air was used, since the molecular mass of  $CO_2$ ,  $\mathcal{M}_{CO_2} \approx 44 \text{ kg/kmol}$ , while  $\mathcal{M}_{air} \approx 28 \text{ kg/kmol}$ . Further, there is a specific heat capacity difference between the two fluids;  $c_{p,CO_2} = 846 \text{ J/kg/K}$  and  $c_{p,air} = 1003 \text{ J/kg/K}$  at  $300 \text{ K}$ . The DR for the tests with  $CO_2$  over the DR for the tests with air is 1.57, while the ratio of their specific heat capacities,

$c_{p,CO_2}/c_{p,air} = 0.843$ . For transpiration cooling models, Simpson [57] showed the specific heat capacity ratio affects cooling by  $(c_{p,CO_2}/c_{p,air})^{0.6} = 0.902$ , or close to unity. Therefore, the differences in  $\eta$  which arose due to  $CO_2$  as the coolant were attributed to the DR and not the difference in specific heat capacity.

#### 4.4 Improvements to the Transient Technique

Three major improvements to the technique described in Sec. 4.1 (p. 60) came out of this research. First, a multipoint non-linear least squares correlation was used to determine  $T_{aw}$  and  $h$  instead of just two points. Second, a method for correcting the unavoidable coolant temperature increase which accompanies transient heat transfer tests was implemented. Third, any error in the start time for the transient process was removed through statistical analysis of the data.

*Non-Linear Least Squares Correlation.* The accuracy with which  $T_{aw}$  and  $h$  are determined is dependent upon not just the accuracy of the temperature and time measurements, but also the non-dimensional time at which the temperatures are recorded. Recall:

$$\frac{T_S - T_i}{T_{aw} - T_i} = 1 - \exp\left(-\frac{h^2 \alpha t}{k^2}\right) \operatorname{erfc}\left(\frac{h \sqrt{\alpha t}}{k}\right) \quad (71)$$

The independent variables are  $T_S$  and  $t$ , and the dependent variables are  $T_{aw}$  and  $h$ . The non-dimensional time is defined as  $\frac{h^2 \alpha t}{k^2}$ .

Consider Fig. 21: if the temperatures are taken only at the far right side of the graph, when  $\frac{h^2 \alpha t}{k^2}$  is large and  $\frac{T_S - T_i}{T_{aw} - T_i}$  is nearing unity, then a very small change in  $T_S$  or  $T_i$  can have a huge impact on the calculated value of  $h$  because the slope is very near zero. Using two points even a  $\pm 1 K$  error when temperatures are taken at  $\frac{h^2 \alpha t}{k^2} = 0.1$  and 0.8 can change the calculated value of  $h$  by up to 150%!

Using a multipoint correlation, however, the curve fit error, which is really the source of the problematic divergence in  $h$ , can be reduced by  $1/\sqrt{n}$ , where  $n$  is the number of points used in the correlation. By choosing wisely the time interval over

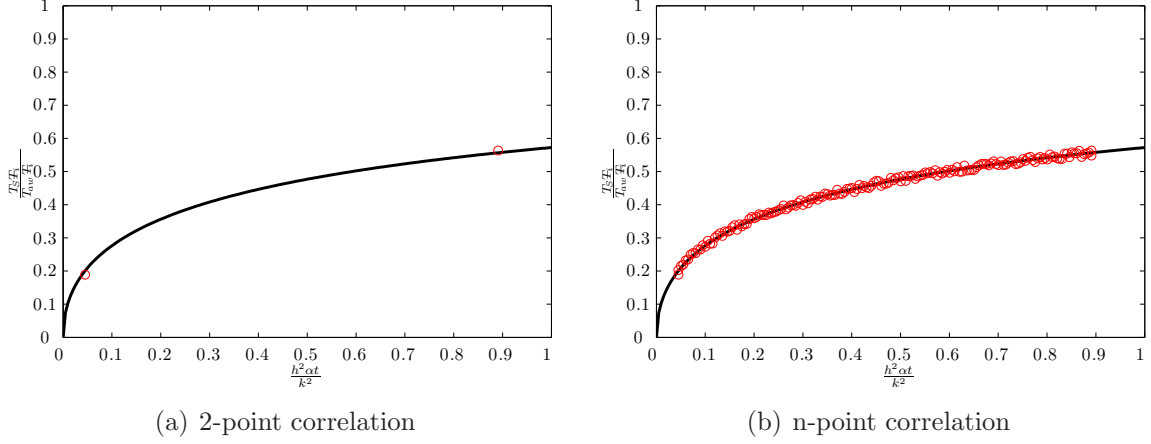


Figure 21: Comparison of 2-point and  $n$ -point correlations. The 2-point correlation results in a wide range of possible  $h$ -values with only a modest error in surface temperature.

which the data is recorded, one can limit the slope errors (errors in  $h$ ) by ensuring the data are over a relatively high-slope domain. The errors in measurement for this experiment are in Table 5, Sec. 4.6 (p. 79).

*Coolant Temperature Drift Correction.* The experimental technique which uses Eq. 71 is transient, which means the temperatures at all points of measurable interest are rising, including the coolant temperature. Consider one is measuring surface temperatures which are assumed to be affected by a *constant*  $T_{aw}$  and *constant*  $h$ . If either parameter is varying, the assumptions used in deriving the model by which these quantities are solved are no longer valid, and the model must be scrapped. In this case, the coolant temperature immediately before the hole exit is changing with time because the coolant is absorbing some heat from the adjacent wall. This has the effect, when used in the curve fit, of *lowering* the calculated  $h$  and *raising* the calculated  $T_{aw}$ . The erroneous values arise because as the temperature of the wall under the coolant approaches what should be the adiabatic wall temperature, instead the adiabatic wall temperature slowly creeps up, and the curve quickly moves toward wrong solutions of  $h$  and  $T_{aw}$ .

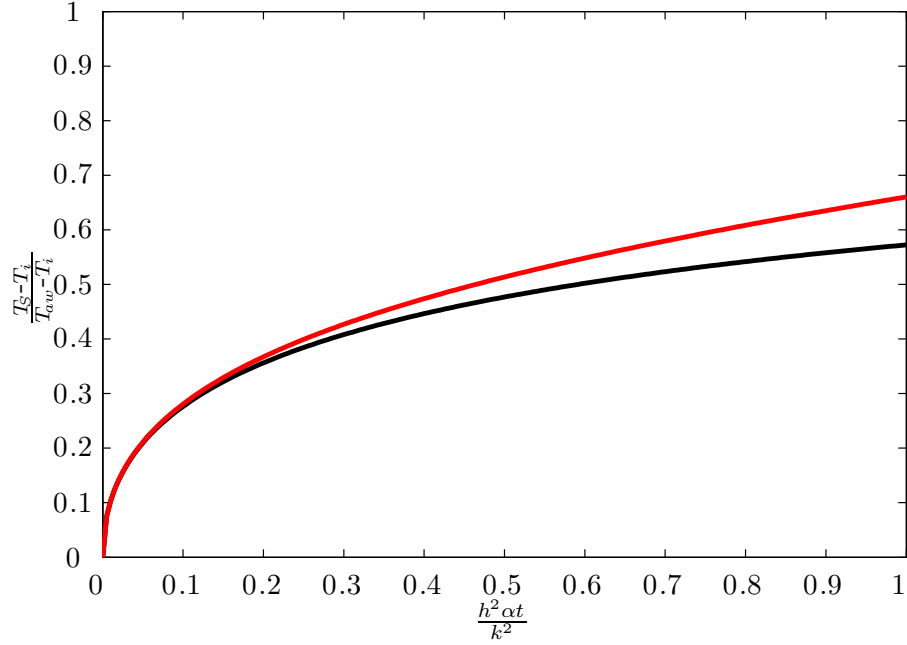


Figure 22: Coolant temperature drift effect. The red line shows the uncorrected data; this curved will yield artificially (and unrealistically) low values of  $h$  and high values of  $T_{aw}$ . The black curve is corrected by the proposed method and yields correct results.

To correct this anomaly, the slope of  $T_S$  over time must be corrected (lowered) as in Fig. 22. This ensures the boundary condition required to use Eq. 71 is correctly applied. At each time step, the coolant temperature can be observed on the IR camera by looking for the coldest point on the image, which occurs always inside the hole at the farthest upstream location. Plotting this pixel's temperature, and the temperature of the pixels around it, allows one to correct the temperatures at all other parts of the image. The surface temperatures affected by the jet are then linearly re-scaled so the coldest jet temperatures are at the initial coolant temperature. This method is a conduction correction which allows one to properly apply the temperature boundary condition, thus negating effects of conduction through the solid and into the coolant jet.

Proper application of the boundary conditions ensures the adiabatic wall temperatures remains constant for the test duration. Thus the quality of results is improved, and no new model is required.

*Delayed Start Correction.* The calculation of  $h$  and  $T_{aw}$  requires not only the error in time  $t$  be low, but also the start time  $t_o$  be known to great accuracy. Given the unavoidable uncertainty in when the transient process actually starts due to accelerating flow or coupon placement, a robust method was required to determine the absolute start time for the transient process.

To find the time error, start again with

$$\frac{T_S - T_i}{T_{aw} - T_i} = 1 - \exp\left(\frac{h^2 \alpha t}{k^2}\right) \operatorname{erfc}\left(\frac{h \sqrt{\alpha t}}{k}\right) \quad (71)$$

A modified form is proposed for the surface region upstream of the hole:

$$\frac{T_S - T_i}{T_\infty - T_i} = 1 - \exp\left(\frac{h^2 \alpha (t + \tau)}{k^2}\right) \operatorname{erfc}\left(\frac{h \sqrt{\alpha (t + \tau)}}{k}\right) \quad (72)$$

A dependent variable,  $T_{aw}$ , has been made into a constant, and a new independent variable,  $\tau$ , has been introduced. Since this region is upstream of the coolant hole,  $T_{aw} = T_\infty$ .

The new term  $\tau$  is the time between when the test article begins the transient heating process and when  $t_o$  is recorded. Eq. 72 makes use of the knowledge of  $T_{aw}$  in the region upstream of the coolant hole where flow is unaffected by the coolant jet. Here  $T_{aw} = T_\infty$ , so Eq. 71 could yield  $h$  directly. In this region then, Eq. 72 will yield not only  $h$  but also quantify the time error, or magnitude of the delayed start. Curve fitting to solve for  $\tau$  is inherently statistical, so a statistical approach is used to group  $\tau$  calculated for each point. Since every point experiences the same start time and delay,  $\tau$  is determined by looking at the probability density, like the one in Fig 23 of  $\tau$  calculated for each point. The peak of this distribution is the most likely time error for the entire surface.

This method removes a source of error: the uncertainty in  $t_o$ . It is repeatable for every case and yields a nearly Gaussian distribution with a strong, narrow peak for each case.

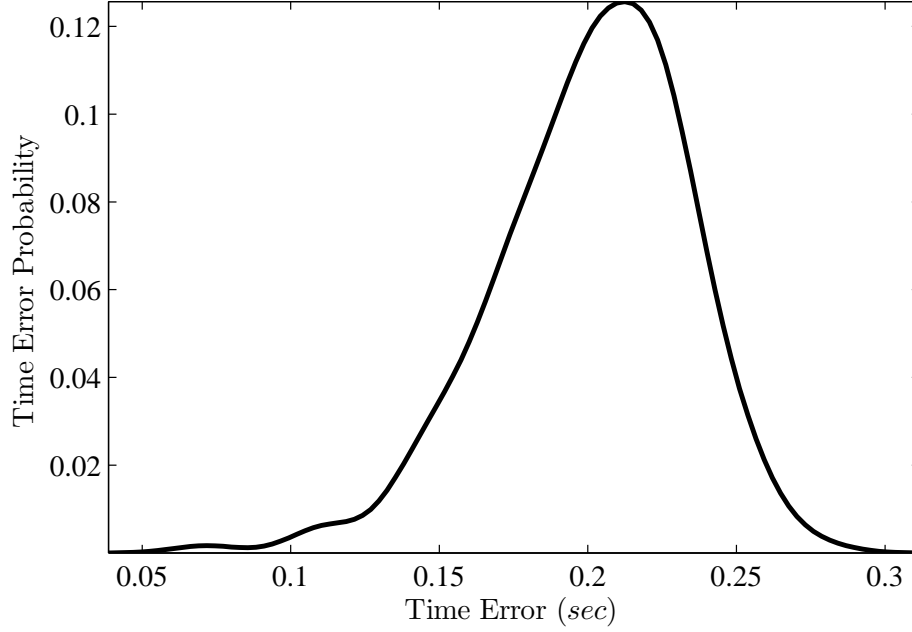


Figure 23: Example of time error histogram. This figure shows an example of the probability density for the delay in start time for pixels upstream of the hole, where  $T_{aw}$  is known and  $h$  is not known. The distributions for each experiment are nearly Gaussian and the peak is used for  $\tau$ .

#### 4.5 *Experimental Procedure*

As explained in the section on response variables (p. 63), it was necessary to measure surface temperature over time. The specific method by which this was accomplished is laid out here. Figure 19 (p. 68) shows the actual test apparatus used in these experiments.

In the beginning of each experiment, there were no test articles (coupons) in the test rig. The air was turned on to a preset velocity, which was controlled by a control-feedback mass flow controller system. This system uses a differential pressure flow meter for readings and a needle valve for control. The air was then heated until the temperature inside the test rig reached  $343\text{ K}$ . Once the bulk temperature reached steady state, the flow velocity was adjusted so  $Re = 31\,000$ . The mass flow rate was actively maintained by the flow controller.

When the desired coupon was found to be at a steady state temperature (by the agreement of temperature between internal and external thermocouple readings) the coolant was turned on. The coolant was verified to be at the same temperature as the coupon (usually about  $296\text{ K}$ , but varied throughout the day), so no transient heating or cooling had yet occurred. Measurements of the surface and plenum thermocouples were taken. The coupon was then quickly placed in the free-stream flow. Measurements of surface temperature were taken 30 times a second by an IR camera. The specific attributes of this camera, including the calibration method, can be found in the appendix (p. 134).

When ten seconds had expired, the coupon was removed and placed on a table to again reach steady state. A tabletop fan blew on the coupons to help decrease the amount of time it took for the coupon to reach steady state temperature. In general, the coupon reached steady state cool temperature in at most 20 minutes. The coupon was then ready for another test.

Table 4 shows which configurations were tested using the transient method. The  $h_o$  tests were required to calculate NHFR (Eq. 24, p. 13) and were required for each free-stream configuration, as no blowing occurred during these tests. Overall, 119 tests were completed.

The data collected needed some processing to yield useful information. Initially it contained about 300 frames (30 frames per second  $\times$  10 seconds) of surface temperatures. Several steps were taken to extract  $\eta$  from this data.

The surface had to be “unfolded” so there would be a flat surface for marking distance from the hole. This would allow direct comparison between configurations using units of hole diameters along the wall. Once the surface was flat, the recorded temperatures were corrected to thermocouple values as explained in the appendix (p. 134). With the IR camera temperatures and thermocouple temperatures thus brought into sync, the temperatures at each frame were corrected for coolant temperature drift via linear interpolation between the coolant temperature at each time

Table 4: Matrix Of Tests To Be Performed

		$D_\infty/D_j$						
		$\alpha = 90^\circ$			$\alpha = 0^\circ$			
		97.0	64.4	48.5	32.2	16.1	64.4	97.0
$F$	0.50							
	0.70							
	1.00							
	1.25							
	1.50							
	$h_o$							
	0.50							
	0.70							
	1.00							
	1.25							
	1.50							
	$h_o$							
	0.50							
	0.70							
	1.00							
	1.25							
	1.50							
	$h_o$							
$dP/dx$	0.50							
	0.70							
	1.00							
	1.25							
	1.50							
	$h_o$							
High $DR$	0.50							
	0.70							
	1.00							
	1.25							
	1.50							

step and the free-stream temperature. These fully corrected temperatures were used to calculate the time delay error by using the region upstream of the hole where there was no coolant present. Once the time error was known,  $T_{aw}$  and  $h$  were determined at each pixel using the non-linear least squares curve fit method. With these two quantities in hand,  $\eta$  and NHFR were easily calculated.

#### 4.6 Analysis of Experimental Uncertainty

Using the method of Kline and McClintock [81], the uncertainty in a calculated value is based on the uncertainty of measured values :

$$w_R = \left[ \sum_{i=1}^n \left( \frac{\partial R}{\partial x_i} w_i \right)^2 \right]^{1/2} \quad (73)$$



Table 5: Absolute Errors of Measured Quantities

Parameter	units	value $\pm$	$w_i$
thermal conductivity	$W/(m^2 \cdot K)$	$0.030\pm$	0.0005
thermal diffusivity	$m^2/s \times 10^{-9}$	$210.\pm$	4
time	$s$	$t\pm$	0.1005
temperatures	$K$	$T\pm$	0.205

where  $R$  is the calculated value,  $x_i$ 's are measured values required for the calculation of  $R$ , and  $w_i$ 's are the measurement uncertainties of  $n$  number of quantities  $x_i$  (in the units of  $x_i$ ). Values for  $w_i$  for this experiment are contained in Table 5.

The experimental technique presented in Sec. 4.1 does not measure one variable, but two, which means there are two measurement uncertainties to determine. Recall once more Eq. 71:

$$\frac{T_S - T_i}{T_{aw} - T_i} = 1 - \exp\left(\frac{h^2 \alpha t}{k^2}\right) \operatorname{erfc}\left(\frac{h\sqrt{\alpha t}}{k}\right) \quad (71)$$

To make the measurement uncertainty calculations a little easier, two new terms are introduced. The first

$$\theta \equiv \frac{T_S - T_i}{T_{aw} - T_i} \quad (74)$$

is the non-dimensional temperature already discussed. The second

$$\phi \equiv \frac{h\sqrt{\alpha t}}{k} \quad (75)$$

is the non-dimensional time already discussed. Now Eq. 71 is simply

$$\theta = 1 - \exp(\phi^2) \operatorname{erfc}(\phi) \quad (76)$$

with the new notations  $\theta$  and  $\phi$ .

It is important to note there is only one equation to determine the measurement uncertainties associated with Eq. 71. Yet two quantities,  $w_{T_{aw}}$  and  $w_h$ , are needed.

Since neither the heat flux coefficient nor the adiabatic wall temperature are directly measured, there is no uncertainty in their measurement. So the uncertainties due to measurement of each are easily obtained by holding one unknown error as zero, say  $w_h$  initially, and solving for the calculated uncertainty in the other, in this case  $w_{T_{aw}}$ .

Equation 76 may be differentiated as

$$\frac{\partial \theta}{\partial \phi} = 2\phi(\theta - 1) + \frac{2}{\sqrt{\pi}} \quad (77)$$

Though not always mathematically true, in this case

$$\frac{\partial \phi}{\partial \theta} = \left( \frac{\partial \theta}{\partial \phi} \right)^{-1} \quad (78)$$

which can be verified numerically.

The derivatives of  $h$  are

$$\frac{\partial h}{\partial \phi} = \frac{h}{\phi} \quad (79)$$

$$\frac{\partial h}{\partial t} = \frac{-h}{2t} \quad (80)$$

$$\frac{\partial h}{\partial k} = \frac{h}{k} \quad (81)$$

$$\frac{\partial h}{\partial \alpha} = \frac{-h}{2\alpha} \quad (82)$$

The derivatives of  $T_{aw}$  are

$$\frac{\partial T_{aw}}{\partial T_S} = \frac{1}{\theta} \quad (83)$$

$$\frac{\partial T_{aw}}{\partial T_i} = 1 - \frac{1}{\theta} \quad (84)$$

$$\frac{\partial T_{aw}}{\partial \theta} = \frac{T_i - T_S}{\theta^2} \quad (85)$$

The derivatives of  $\theta$  are

$$\frac{\partial\theta}{\partial T_S} = \frac{\theta}{T_S - T_i} \quad (86)$$

$$\frac{\partial\theta}{\partial T_i} = \frac{\theta - 1}{T_S - T_i} \quad (87)$$

$$\frac{\partial\theta}{\partial T_{aw}} = \frac{T_i - T_S}{T_{aw}^2} \quad (88)$$

$$\frac{\partial\theta}{\partial\phi} = 2\phi(\theta - 1) + \frac{2}{\sqrt{\pi}} \quad (89)$$

The derivatives of  $\phi$  are

$$\frac{\partial\phi}{\partial h} = \frac{\phi}{h} \quad (90)$$

$$\frac{\partial\phi}{\partial t} = \frac{\phi}{2t} \quad (91)$$

$$\frac{\partial\phi}{\partial k} = \frac{-\phi}{k} \quad (92)$$

$$\frac{\partial\phi}{\partial\alpha} = \frac{\phi}{2\alpha} \quad (93)$$

$$\frac{\partial\phi}{\partial\theta} = \left(\frac{\partial\theta}{\partial\phi}\right)^{-1} \quad (94)$$

Now the measurement uncertainty in  $h$  may be written as

$$w_h = \left\{ \left(\frac{\partial h}{\partial t} w_t\right)^2 + \left(\frac{\partial h}{\partial k} w_k\right)^2 + \left(\frac{\partial h}{\partial\alpha} w_\alpha\right)^2 + \left(\frac{\partial h}{\partial\phi} \frac{\partial\phi}{\partial\theta}\right)^2 \left[ \left(\frac{\partial\theta}{\partial T_S} w_{T_S}\right)^2 + \left(\frac{\partial\theta}{\partial T_i} w_{T_i}\right)^2 \right] \right\}^{1/2} \quad (95)$$

The uncertainty in  $h$  based on this equation varies inversely with the adiabatic effectiveness, and is between 3% and 16% for the data generated in this work.

The measurement uncertainty in  $T_{aw}$  may be written as

$$w_{T_{aw}} = \left\{ \left( \frac{\partial T_{aw}}{\partial T_s} w_{T_s} \right)^2 + \left( \frac{\partial T_{aw}}{\partial T_i} w_{T_i} \right)^2 + \left( \frac{\partial T_{aw}}{\partial \theta} \frac{\partial \theta}{\partial \phi} \right)^2 \left[ \left( \frac{\partial \phi}{\partial t} w_t \right)^2 + \left( \frac{\partial \phi}{\partial \alpha} w_\alpha \right)^2 + \left( \frac{\partial \phi}{\partial k} w_k \right)^2 \right] \right\}^{1/2} \quad (96)$$

The uncertainty in  $T_{aw}$  based on this equation varies inversely heat transfer coefficient, and is between  $0.6\text{ K}$  and  $1.2\text{ K}$  for the data generated in this work.

The data of interest is in terms of  $\eta$ , the adiabatic effectiveness, and net heat flux reduction (NHFR). Performing the same uncertainty analysis on these variables yields the uncertainty in these variables. Recall the definition of  $\eta$  ( $\eta_f$ ) is

$$\eta = \frac{T_\infty - T_{aw}}{T_\infty - T_c} \quad (15)$$

Therefore the uncertainty in  $\eta$  is

$$w_\eta = \left| \frac{w_{T_{aw}}}{T_c - T_\infty} \right| \quad (97)$$

Recall the definition of NHFR is

$$\text{NHFR} = 1 - \frac{h_f}{h_o} \left( 1 - \frac{\eta_f}{\phi} \right) \quad (24)$$

where  $\phi$  is a defined quantity with no uncertainty. The uncertainty in NHFR is

$$w_{\text{NHFR}} = \left[ \left( \frac{\text{NHFR} - 1}{h_f} w_{h_f} \right)^2 + \left( \frac{1 - \text{NHFR}}{h_o} w_{h_o} \right)^2 + \left( \frac{h_f}{h_o \phi} w_\eta \right)^2 \right]^{1/2} \quad (98)$$

The uncertainty in  $\eta$  for these experiments vary from 0.009 to 0.020. The uncertainty in NHFR for these experiments vary from 0.04 to 0.15, when  $\phi = 0.7$ .

There is another error in the transient technique due to two-dimensional (2-D) conduction which has not yet been explored in the literature. Heat transfer normal to the surface and *only* normal to the surface is a critical assumption for the solution contained in Eq. 71. In the method used here, this implies each pixel is modeled as a rectangular prism of sufficient depth to be assumed a semi-infinite slab, and is isolated adiabatically from each adjacent pixel. Since each pixel can experience different  $h$ 's and have different  $T_{aw}$ 's, there will exist temperature profiles into and normal to the surface at any time  $t$  which may be different for each pixel. This temperature difference will induce a real heat flux between pixels not accounted for by the model. This heat flux will vary with depth into the solid.

The effects of lateral conduction appear in the measurements of surface temperature. Figure 24 illustrates the following scenario: suppose pixel  $A$  which, adiabatically, would be cold is adjacent to pixel  $B$  which, adiabatically, would be warmer, or  $T_{aw\ A} < T_{aw\ B}$ . Let  $l_y$  denote the span-wise distance between two pixels and  $z$  denote the distance normal to and into the surface. Without placing any limits on the relative measures of  $h$ , there will be a temperature difference  $\partial T/\partial y$  which will cause heat to flow from pixel  $B$  to pixel  $A$ . This will have the effect of raising the apparent  $T_{aw\ A}$  and  $h_A$ , while doing the opposite to the same quantities at pixel  $B$ . This apparent effect is due to the presence of heat transferred into pixel  $A$  from pixel  $B$  which is unaccounted for in the 1-D model.

To quantify this error, the simplifying assumption is first made that temperature gradients  $\partial T/\partial x_i$  will be much greater in the span-wise direction than the stream-wise. This is justified based on observation of contour plots of adiabatic effectiveness. The heat flux is proportional to the temperature gradient by

$$\dot{q}_{x_i}'' = k \frac{\partial T}{\partial x_i} \quad (99)$$

where  $x_i$  is the direction of the heat flux  $\dot{q}_{x_i}''$ ,  $\partial T/\partial x_i$  is the temperature gradient, and  $k$  is the bulk, isotropic thermal conductivity.

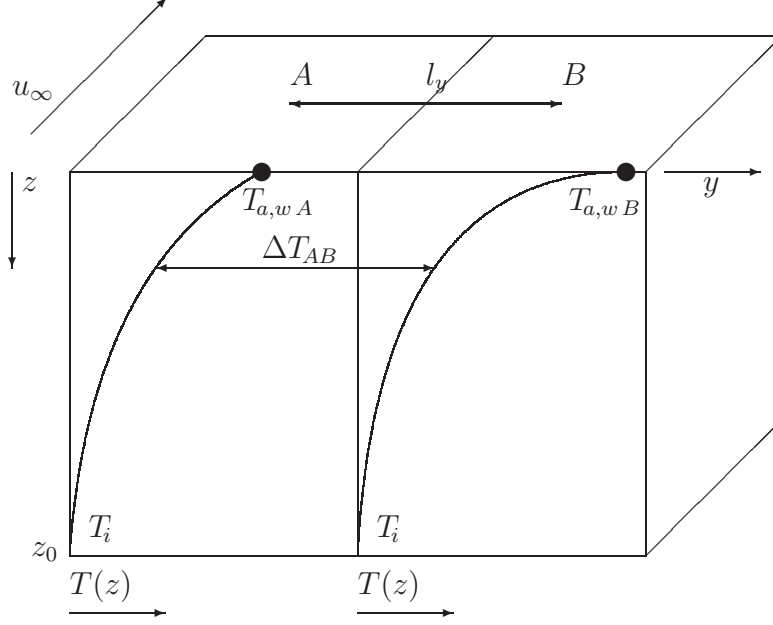


Figure 24: Adjacent pixels undergoing transient convective heating.

Heat transfer into the surface from the free-stream is assumed to be 1-D, so we must find the heat transfer *not* normal to the surface to get the error due to lateral conduction. For the following derivation,  $z$  is the direction normal to and into the surface, and  $y$  is the direction of lateral, or span-wise, conduction. The heat transfer *into* pixel  $A$  from pixel  $B$  is

$$\begin{aligned}
 \dot{q}_y'' &= \lim_{l_z \rightarrow \infty} \frac{k}{l_z} \int_{z=0}^{l_z} \frac{\partial T_{AB}}{\partial y} dz \\
 &\approx \frac{k}{z_0} \int_{z=0}^{z_0} \frac{T_B(z) - T_A(z)}{l_y} dz \\
 &= \frac{k}{z_0 l_y} \int_{z=0}^{z_0} [T_B(x) - T_A(x)] dz
 \end{aligned} \tag{100}$$

where  $l_y$  is the distance between pixel centers in the span-wise direction and is a constant.  $z_0$  is the depth at which the lateral heat flux is effectively zero. Recognizing

$$\overline{\Delta T_{AB}} = \frac{\int_{z=0}^{z_0} [T_B(x) - T_A(x)] dz}{z_0} \quad (101)$$

brings out  $z_0$  as the depth at which  $[T_B(x) - T_A(x)] \approx 0$ , which means  $\dot{q}'' \approx 0$ . The value for  $z_0$  should be chosen so there is little change in  $\overline{\Delta T_{AB}}$  if a larger value is used. The heat transfer into the surface from the free-stream fluid is

$$\dot{q}_x'' = h_A (T_{a,w A} - T_{S,A}) \quad (102)$$

The magnitude of heat transfer into pixel  $A$  due to lateral conduction relative to the heat transfer from the free-stream fluid can be found by dividing Eq. 100 by Eq. 102 to obtain

$$\begin{aligned} \left( \frac{\dot{q}_y''}{\dot{q}_x''} \right)_A &= \frac{\frac{k}{l_x l_y} \int_{x=0}^{\infty} [T_B(x) - T_A(x)] dx}{h (T_{a,w A} - T_{S,A})} \\ &= \frac{\overline{\Delta T_{AB}}}{Bi_{l_y} (T_{a,w A} - T_{S,A})} \end{aligned} \quad (103)$$

The Biot number ( $Bi$ ) is defined as  $hl_y/k$  and is a measure of the relative heat transfer rates of conduction and convection to a surface. For this experiment,  $l_y = 0.2 \text{ mm}$ .

Quantifying the result of Eq. 103 is difficult by solely experimental means, if not impossible. This difficulty arises from the lack of knowledge of the adiabatic  $T(x)$  at every pixel and time, something which cannot be measured via the transient method since lateral conduction presumably distorts the measured surface temperature  $T_S$  which is required for the calculation of  $T(x)$ . However, some qualitative measures can be taken to minimize the lateral conduction error based on this analysis. Note first: the regions of highest span-wise temperature gradients tend to have high heat flux coefficients. Second, as  $h$  grows, so do  $Bi$  and  $l_x$ . Third, at small time  $t$  the tempera-

ture difference ( $T_{a,wA} - T_{S,A}$ ) will be largest. Therefore, to minimize the contribution of lateral conduction:

- $Bi \gg 1$  is desired everywhere;
- regions with low  $T_{aw}$  should have proportionally higher  $h$  values to limit the conduction error;
- data should be taken at the smallest possible  $t$ .



## V. Inert Gas Experiment Results

As explained in Chap. IV, the completed experiments focused on three effects on cooling effectiveness: radial curvature, strong favorable stream-wise pressure gradient, and high density ratio . The results presented here explain these effects and provide insight on possible interactions between the different phenomena. Blowing ratio effects for each configuration are also presented. Compound angle injection ( $\alpha = 90^\circ$ ) results are presented first, followed by the stream-wise injection ( $\alpha = 0^\circ$ ) results.

Recall from p. 12 adiabatic effectiveness for film cooling is defined as

$$\eta_f = \frac{T_\infty - T_{aw}}{T_\infty - T_c} \quad (15)$$

where  $T_\infty$  is the free-stream temperature,  $T_{aw}$  is the adiabatic wall temperature, and  $T_c$  is the coolant inlet temperature.  $\eta_f$  is a non-dimensional measure of the effectiveness of the coolant at the wall. When  $\eta_f = 0$  the adiabatic wall is un-cooled, and when  $\eta_f = 1$  the adiabatic wall is completely cooled, or equal to the coolant injection temperature. The results to follow are concerned solely with film cooling, not transpiration cooling, so  $\eta_f$  is simply called  $\eta$ .

In each case the span-wise averaged adiabatic effectiveness,  $\eta_{\overline{span}}$ , defined as

$$\eta_{\overline{span}}(y) = \frac{1}{\xi_2 - \xi_1} \int_{-\xi_1}^{\xi_2} \eta_f \, dx \quad (16)$$

was generated based on eight hole diameters in the span-wise direction, or  $\xi_2 - \xi_1 = 8$  hole diameters.

The area averaged adiabatic effectiveness,  $\zeta$ , defined as

$$\zeta = \frac{1}{(\xi_2 - \xi_1)(\gamma_2 - \gamma_1)} \int_{-\xi_1}^{\xi_2} \int_{-\gamma_1}^{\gamma_2} \eta_f \, dx \, dy \quad (17)$$

was calculated using eight hole diameters in the span-wise direction and from one to ten hole diameters downstream of the hole center ( $\xi_2 - \xi_1 = 8$  hole diameters and  $\gamma_2 - \gamma_1 = 9$  hole diameters).

The plots of  $\eta_{\overline{span}}$  vs.  $y/d$ , distance downstream of the hole in units of hole diameters, use continuous lines instead of discrete data points. The data are not continuous, but there are so many points it would appear the data are continuous if discrete points were used. Each plot of  $\eta_{\overline{span}}$  use a color scheme in which red is the minimum value and purple is the maximum value, following the common color order. For the plots comparing different curvatures at the same blowing ratio, red would represent the lowest value of  $D_\infty/D_j$  (extreme wall curvature), while purple the highest value (very little curvature). Similarly, if the same curvature is compared at different blowing ratios  $F$ , red represents the lowest blowing ratio, and purple the highest.

### 5.1 Curvature Effects

In Chap. III, simulation results on the effect of radial curvature on adiabatic effectiveness were based on a very low free-stream turbulence intensity. The data here were obtained in an environment with much higher free-stream turbulence. Consequently, no useful comparison with the bulk of the data in Chap. III is possible. However, many qualitative and quantitative comparisons can be made between different experimentally tested configurations. These comparisons yield data about the relative magnitudes of the effects of radial curvature.

*Radial Curvature Effects on  $\eta$ .* In Chap. III the simulation results showed as radial curvature increases ( $D_\infty/D_j$  decreases), span-wise averaged adiabatic effectiveness  $\eta_{\overline{span}}$  increased up to and beyond ten hole diameters downstream. Figure 25 displays the area averaged adiabatic effectiveness,  $\zeta$ , for all the tested curvatures.  $\zeta$  tends to increase as curvature increases up to  $D_\infty/D_j = 32$ . If curvature increases to  $D_\infty/D_j = 16$  there is a decrease in  $\zeta$ .

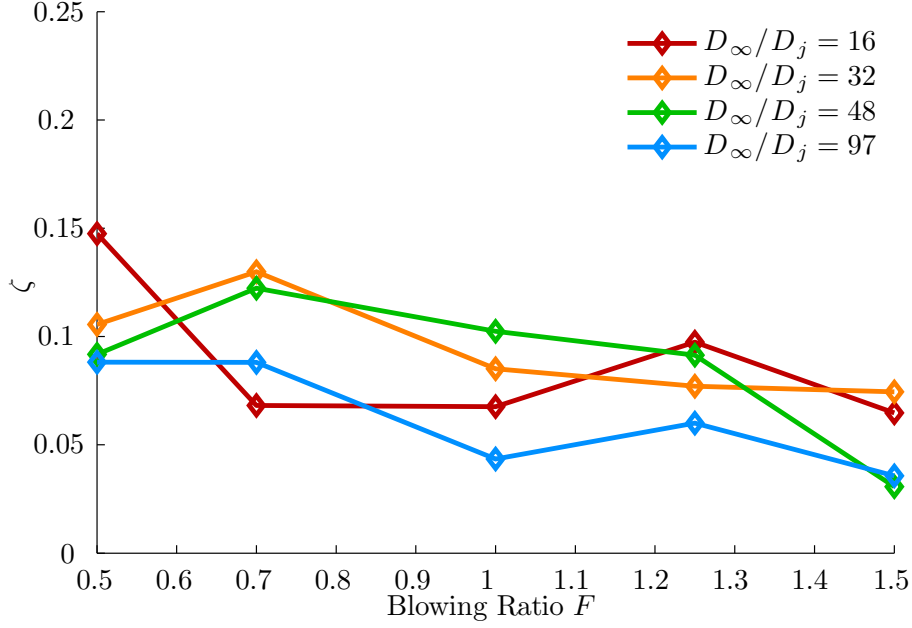


Figure 25: Area averaged adiabatic effectiveness vs. blowing ratio.

Simulation data only covers the cases  $D_\infty/D_j = [32, 64, 96]$ . The additional case of  $D_\infty/D_j = 16$  is one of extreme curvature, which is why it was added to the parameter space. For each of the figures provided in this chapter the colors go from red to purple with increasing  $D_\infty/D_j$ , or with increasing  $F$ , as the case may be. In Fig. 25 notice at  $F = 0.5$  and  $F = 1.5$  the trend is a higher curvature (lower  $D_\infty/D_j$ ) generally yields better performance. However toward the middle of the graph,  $F = 0.7$  and  $F = 1.0$ , the highest curvature (lowest  $D_\infty/D_j$ ) has quite poor performance.

At the low blowing ratio, more of the surface is covered in coolant because of the cradling effect observed in the simulations. As  $F$  increases, the highest curvature case ( $D_\infty/D_j = 16$ ) begins to disrupt the coolant flow and cause it to dissipate more rapidly than the other curvature cases. This may be due to the coolant traveling faster and encountering a faster sloping wall before the free-stream has time to turn the direction of the bulk of the coolant.

In Fig. 25 as  $F$  increases past unity, performance increases for the highest curvature case, the red line. Obviously more coolant is enough to overcome the *extra*

mixing caused by very high curvature. Finally, at the highest blowing ratio,  $F = 1.5$ , performance begins to drop again as mixing again begins to dominate ability of the coolant to adhere to the wall.

Looking at the cases  $D_\infty/D_j = [32, 64, 96]$  it is evident they follow the general trend of  $\zeta$  found in flat plate studies: with increasing  $F$  past about 0.5,  $\zeta$  tends to decrease. There is a slight tendency for the orange line,  $D_\infty/D_j = 32$  to exhibit some of the negative effects of steep curvature around  $F = 1.0$ , similar to but lower magnitude than the  $D_\infty/D_j = 16$  data.

The interaction between curvature and blowing ratio can be quantified by assuming a relation similar to Eq. 64 (p. 46):

$$C = \frac{D_j/D_\infty}{I} \quad (64)$$

Instead of using the momentum ratio,  $I$ , the blowing ratio is used for a first comparison, as is more common in the literature. In terms of  $F$

$$C = \frac{D_j/D_\infty}{I} \quad (64)$$

$$I = F^2/DR \quad (13)$$

$$C = \frac{D_j}{D_\infty} \frac{DR}{F^2} \quad (104)$$

The simulations showed a relationship between  $\eta_{\overline{span}}$  and  $C$ , but this relationship was not quantified. With experimental results in hand, it is now possible to obtain this relationship. Equation 104 gives the expected form, and for this first set of results  $DR \approx 1$ , resulting in

$$\zeta = a \left( \frac{D_\infty}{D_j} \right)^c F^f \quad (105)$$

where  $a$ ,  $c$ , and  $f$  are curve fit parameters to be calculated based on the data. Using a non-linear least squares fit, the coefficients  $a$ ,  $c$ , and  $f$  are solved for. The resulting equation is plotted over the data in Fig. 26 and the coefficients given again in Table 6

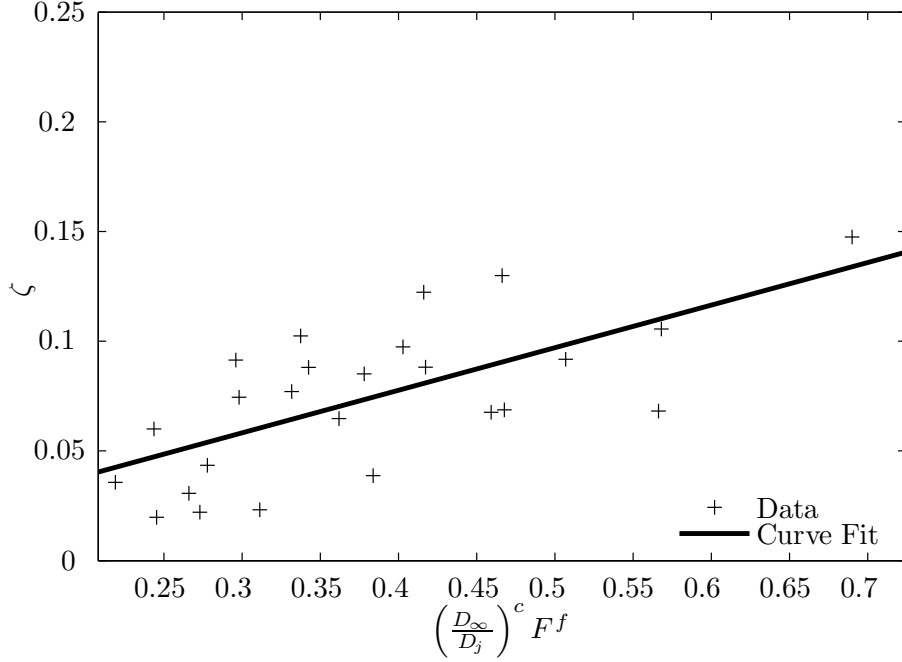


Figure 26: Area averaged adiabatic effectiveness vs. new curvature parameter,  $\alpha = 90^\circ$ . The coefficients for the  $90^\circ$  compound injection case are given in Eq. 106.

(p. 121):

$$\zeta = 0.19 \left( \frac{D_\infty}{D_j} \right)^{-0.28} F^{-0.59} \quad (106)$$

The relationship between  $c$  and  $f$  is close to what is expected from Eq. 104,  $c \approx f/2$ . Since the density ratio  $DR = 1.17$ ,  $DR^{f/2} \approx 1$ . Equation 106 may be rewritten as

$$\zeta \approx \frac{0.2}{\left( I \frac{D_\infty}{D_j} \right)^{0.3}} \quad (107)$$

which has the same form of Eq. 64, improved by a new coefficient and exponent. Again, this form is inspired by the formula for stream-wise curvature (p. 28):

$$Cr = \frac{\nu}{u_\infty R} \quad (37)$$

Since the density ratio  $DR$  is used in other solutions given in this chapter, blowing ratio  $F$  will continue to be used as the argument for Eq. 105 as momentum ratio  $I$  can be easily calculated from this knowledge.

Equation 107 may be used if the flow meets the following conditions:

- high free-stream turbulence ( $Tu \approx 0.26$ )
- density ratio  $DR \approx 1$
- zero pressure gradient
- 90° compound injection and 30° normal injection

A more detailed look at  $\eta_{\overline{span}}$  is given in Fig. 27, which shows  $\eta_{\overline{span}}$  for each curvature compared at the same blowing ratio. At the lowest blowing ratio,  $F = 0.5$  (Fig. 27(a)), the highest curvature case performs better than the lower curvatures even right out of the hole. This increase in performance continues downstream. As  $F$  increases to 0.7 (Fig. 27(b)), we see the first indication of a performance loss due to strong curvature as evidenced by a loss in performance of the red line. However,  $D_\infty/D_j = 32$ , the orange line, is still doing well all the way to 10 hole diameters downstream. Thus, the higher blowing ratio is enough to cause a detriment for the highest curvature, but a benefit is seen for the next highest curvature.

In Fig. 27(c), the blowing ratio has increased to the point where  $D_\infty/D_j = 16$  and  $D_\infty/D_j = 32$  are both performing worse than the next highest curvature, though by the next blowing ratio, the effects of high curvature on performance are starting to reverse. At  $F = 1.25$  (Fig. 27(d)) the high curvature is starting to have a beneficial effect as the mixing characteristic of high blowing ratio is stopped short by the presence of a wall. In other words, the high curvature which was increasing the mixing at low blowing ratios is also serving as an arrest for mixing at some value of  $F$ . By  $F = 1.5$  (Fig. 27(e)), the benefit of curvature to  $\eta_{\overline{span}}$  is making itself evident.

The simulations in Chap. III did not predict  $\eta_{\overline{span}}$  would be *negatively* affected by increased curvature at all. Possible reasons for this include the higher free-stream

turbulence in the experiments, limited range of curvature values, or simply a limit in simulation fidelity. Film cooling is difficult to model in high turbulence environments, so it is likely a combination of these reasons accounts for the difference.

*Blowing Ratio Effects.* The trend put forth in Sec. 5.1 may be visualized in another manner: by comparison of  $\eta_{\overline{span}}$  at different blowing ratios at the same curvature. The information contained in Fig. 28 is displayed in Fig. 27, but now each plot contains different blowing ratios at the same curvature. This arrangement makes it easier to see the effects of blowing ratio on  $\eta_{\overline{span}}$  and which blowing ratios result in performance gain or loss.

The benefits of curvature are not as apparent in Fig. 28(d) since this is the lowest curvature case. The negative effect is not present either. The curves are very close together, something which would be expected in a flat plate case. Figs. 28(a)-28(c) show how the blowing ratio with the best performance changes with curvature. Clearly, the higher the radial curvature (the lower  $D_\infty/D_j$ ) the lower the blowing ratio necessary for peak cooling effectiveness. This rule applies until a large value of  $D_\infty/D_j$  is reached so curvature effects become negligible.

One may ask, why are  $\eta$  and  $\zeta$  for the  $D_\infty/D_j = 64$  case (presented in the appendix, p. 151) so low compared to the rest of the curvatures? I believe the coupon used to generate the  $90^\circ$   $D_\infty/D_j = 64$  data is faulty because the coolant line was found to be leaking after the experiments were completed. The coupon used to get this data was the first one made. It was used for all of the experimental troubleshooting and may have been damaged in the process. However, in case this hypothesis is wrong I am including the data in the appendix so future investigators have access to it. At every blowing ratio tested, this coupon performed much worse than any other. Its performance is *out of family*, and therefore not considered valid. There is nothing wrong with the  $0^\circ$  compound injection case where  $D_\infty/D_j = 64$ , just the  $90^\circ$  one.

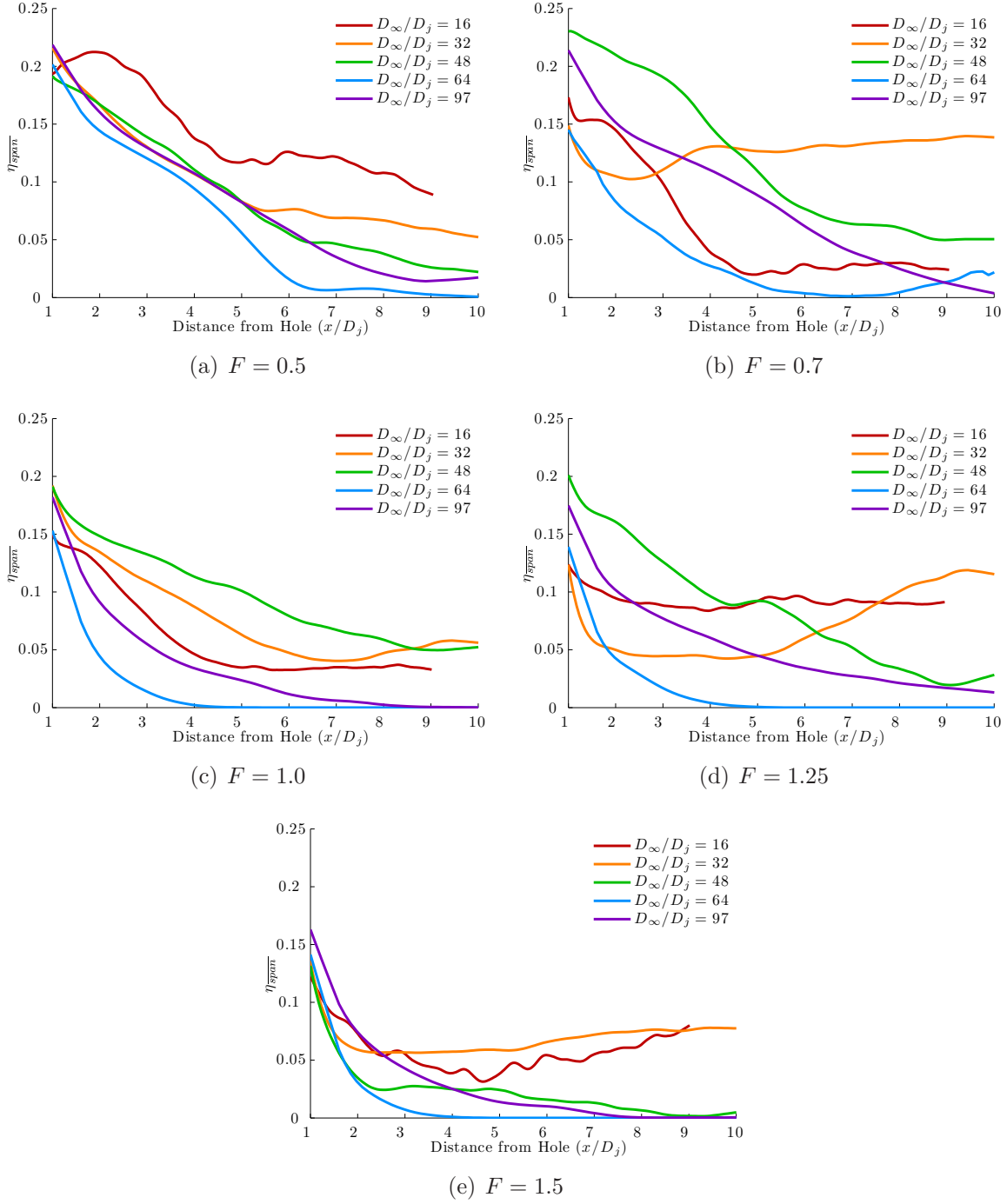


Figure 27: Effect of varying radial curvature at a range of blowing ratios,  $F$ . Each colored line represents a different curvature ratio  $D_\infty/D_j$ .



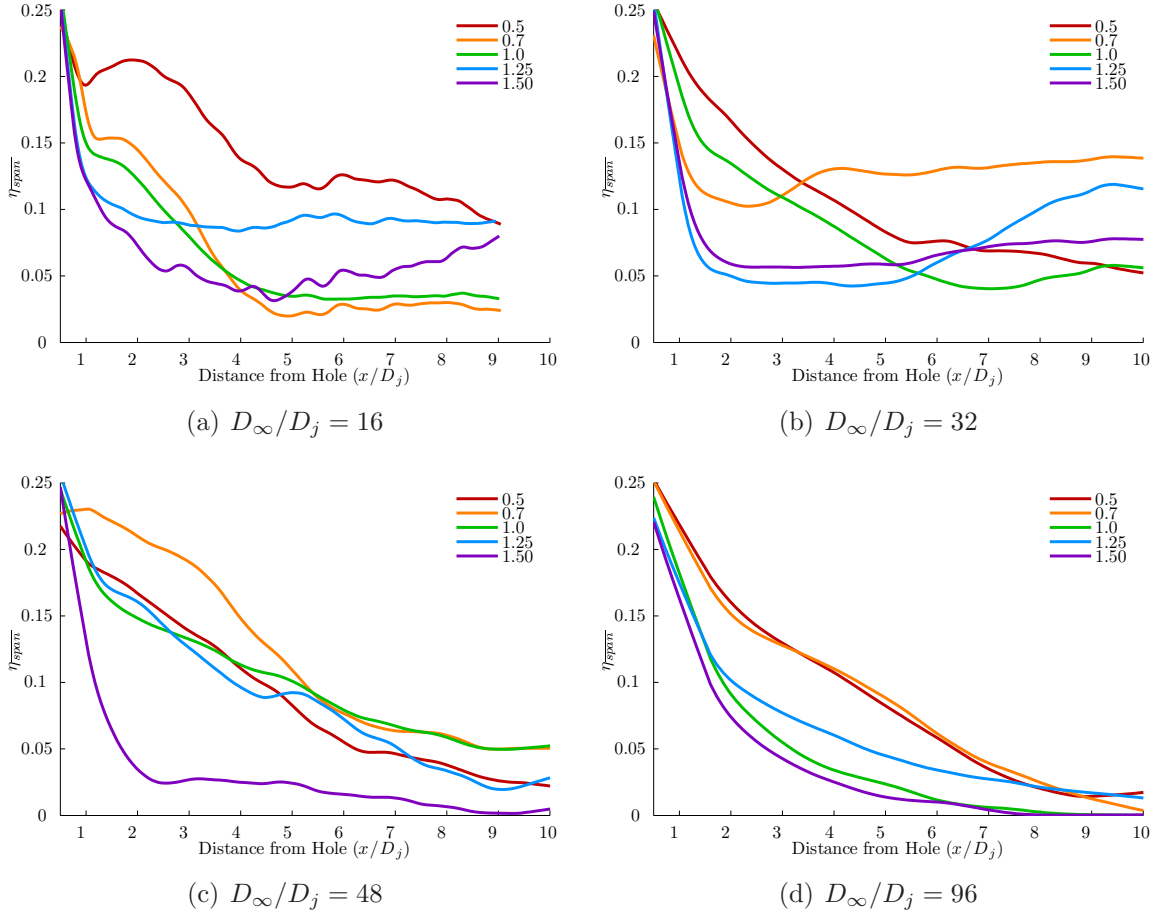


Figure 28: Effect of varying blowing ratio  $F$  at different curvature ratios. Each colored line represents a different blowing ratio.

## 5.2 *Stream-wise Pressure Gradient Effects*

Recall a favorable pressure gradient is what causes flow to accelerate, and is usually due to a contraction in the available flow area. As noted in Sec. 2.5, Dellimore [49] showed pressure gradient effects are dependent on the velocity ratio. In summary, the presence of a favorable pressure gradient will be beneficial at high blowing ratios, but detrimental at low blowing ratios. By their admission, free-stream turbulence has an effect on how the pressure gradient changes adiabatic effectiveness. It appears from the data gathered in this study free-stream turbulence has a great effect since no case was observed to have reduced performance due to the pressure gradient.

*Stream-wise Pressure Gradient Effects on  $\eta$ .* Equation 105 was again employed to determine how pressure gradient affects the area averaged adiabatic effectiveness,  $\zeta$ . Judging by the coefficients of the new curve fit parameters in

$$\zeta = 0.25 \left( \frac{D_\infty}{D_j} \right)^{-0.24} F^{-0.46} \quad (108)$$

it appears the favorable pressure gradient had a beneficial effect on  $\zeta$  overall when compared to the zero pressure gradient case. This curve is plotted over the data in Fig. 29.

The increase in  $a$ ,  $c$  and  $f$  are evidence of an increase in performance. The ratio  $f/c$  is still very close to two, which indicates the pressure gradient does not change the interaction between curvature and blowing ratio, but simply elevates performance overall.

*Blowing Ratio Dependence.* Figure 30 shows how  $\zeta$  changes with blowing ratio in the presence of a favorable pressure gradient. It is clear the performance detriment which plagued the extremely high curvature case ( $D_\infty/D_j = 16$ ) is no longer as potent, especially when compared to Fig. 25.

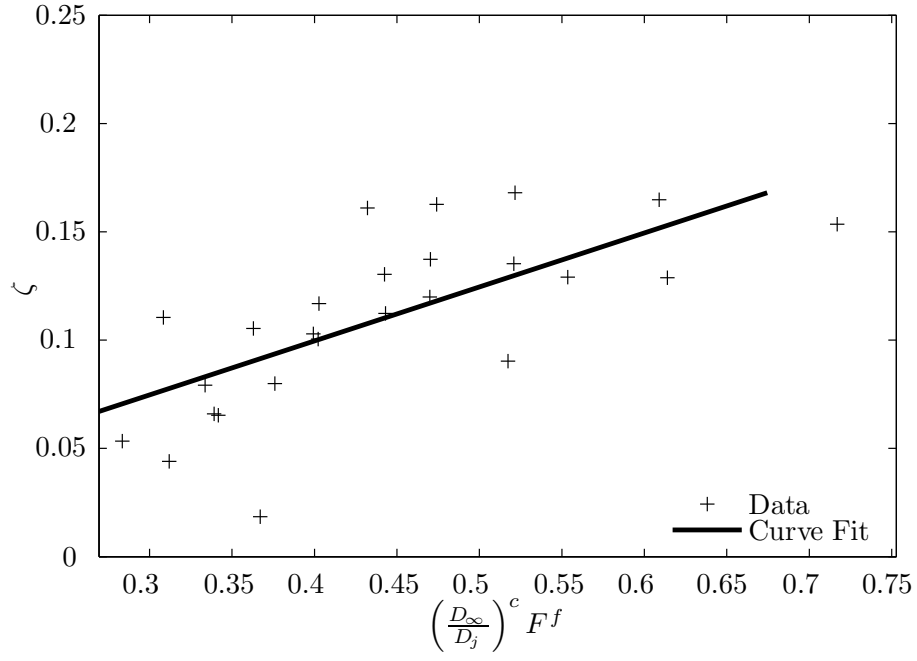


Figure 29: Area averaged adiabatic effectiveness vs. new curvature parameter with strong favorable pressure gradient, as given by Eq. 108. The coefficients for the 90° compound injection case are given in Table 6 (p. 121).

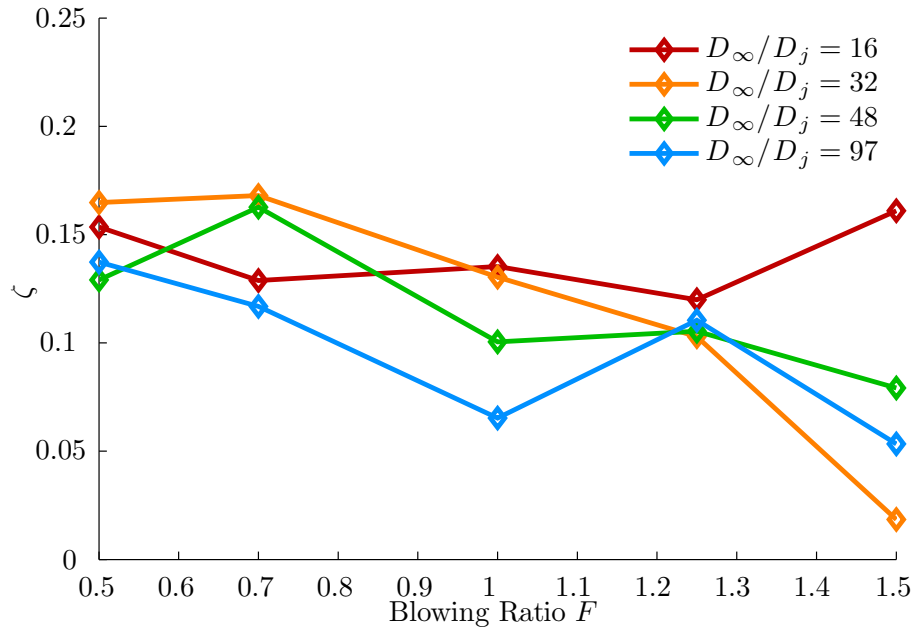


Figure 30: Area-averaged adiabatic effectiveness vs. blowing ratio with strong pressure gradient.

Figure 31 shows  $\eta_{\overline{span}}$  with a strong favorable pressure gradient varies with a similar character as those data gathered without the pressure gradient. However, the magnitude of  $\eta_{\overline{span}}$  is greater in every case. This makes sense based on Dellimore's research: the pressure gradient helps force the jet closer to the wall where separation would have normally occurred.

Figure 31 compares different blowing ratios for the same coupon with the strong favorable pressure gradient. The same general trend observed for the zero pressure gradient case is again seen here: the lowest blowing ratios have better performance than the highest blowing ratios in every case. Additionally, the effectiveness is higher for all blowing ratios at the lower curvatures, indicating more coolant remains at the wall.

Individual comparisons of pressure gradient for the  $\alpha = 90^\circ$  case at each blowing ratio and curvature can be found in the appendix (p. 137).

### 5.3 *Density Ratio Effects*

The experiments discussed thus far were all run with a density ratio,  $DR$ , of 1.17. Experiments with  $DR = 1.76$  were necessary to get results which would be more applicable to rocket conditions. Rockets experience  $DR$  of much higher magnitudes ( $\gg 2$ ), though the tested range gives an indication of the magnitude of effect  $DR$  has on  $\zeta$ .

*High Density Ratio Effects on  $\eta$ .* Equation 105 was used to relate  $\zeta$  to  $F$  with a high density ratio. The coefficients of the new curve fit parameters result in

$$\zeta = 0.16 \left( \frac{D_\infty}{D_j} \right)^{-0.12} F^{0.01} \quad (109)$$

The high density ratio seems to be better for  $\zeta$  overall than even the addition of a favorable pressure gradient. This curve is plotted over the data in Fig. 32.

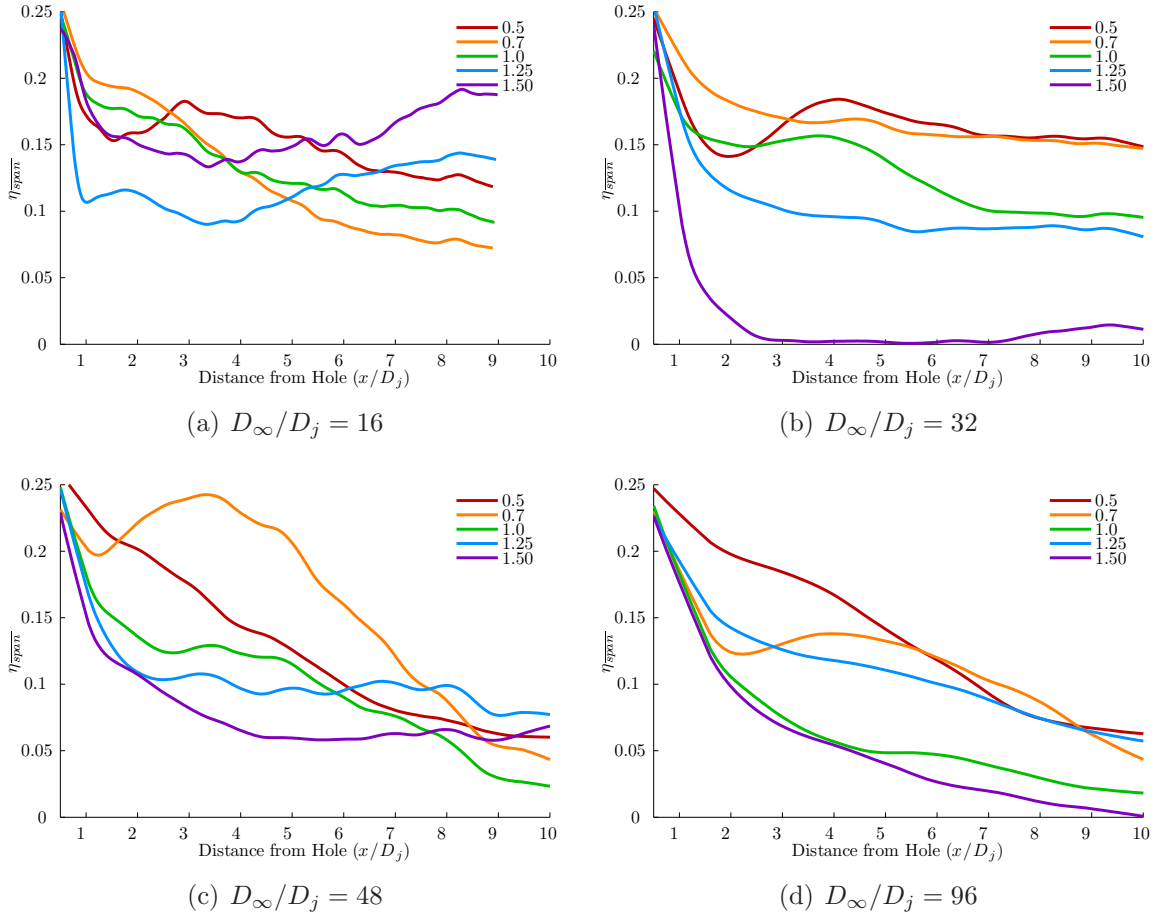


Figure 31: Effect of varying blowing ratio  $F$  at different curvature ratios with a strong favorable stream-wise pressure gradient. Each colored line represents a different blowing ratio. Pressure gradient magnitude  $K = 2.1 \times 10^{-5}$ .

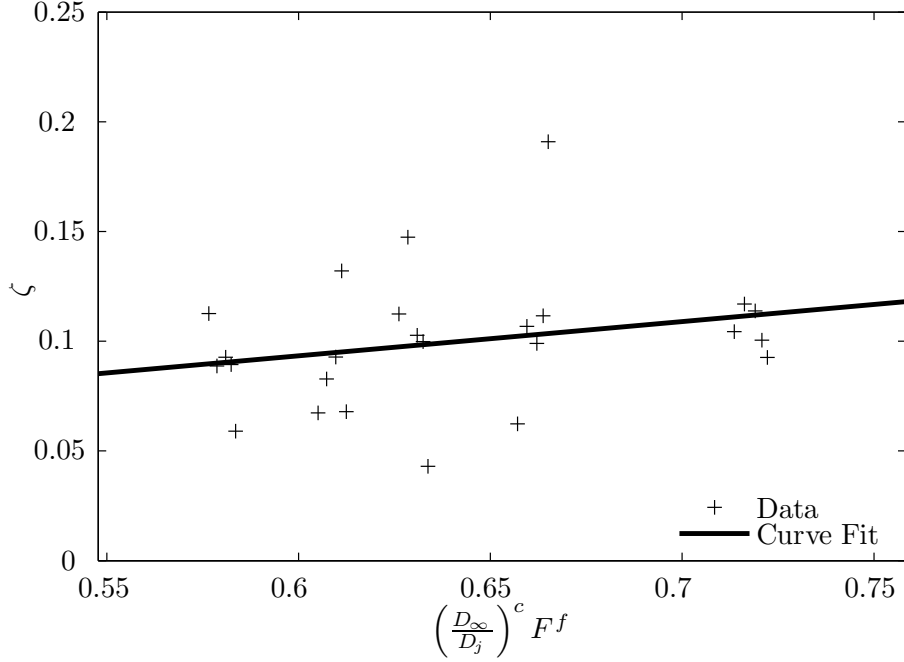


Figure 32: Area averaged adiabatic effectiveness vs. new curvature parameter with high density ratio, as given by Eq. 109. The coefficients for the 90° compound injection case are given in Table 6 (p. 121).

While the addition of a pressure gradient did not change the ratio  $f/c$ , the change in coolant density clearly does. The curvature also affects  $\zeta$  less at higher  $DR$ . Eq. 109 confirms these two changes, which are not as surprising as they may seem at first glance. First, previous studies have shown the density ratio is better modeled by the momentum ratio. In other words, the same blowing ratio with two different coolant densities will result in different coolant velocities. The near independence of  $\zeta$  on  $F$  may simply be due the coolant velocity being lower. The lower coolant velocity has a more constant performance over the range of blowing ratios.

Figure 33 illustrates the linearity  $\zeta$  displays over the range of blowing ratios. The peak performance, once around  $F = 0.5$  to  $0.7$  now lies around  $F = 1.0$ . This effect is consistent with previous research. The velocity of the coolant at  $F = 1.0$  is lower than the low  $DR$  cases, so there is less mixing. Previous studies claim the momentum ratio  $I$  is a better measure of performance between density ratios, but

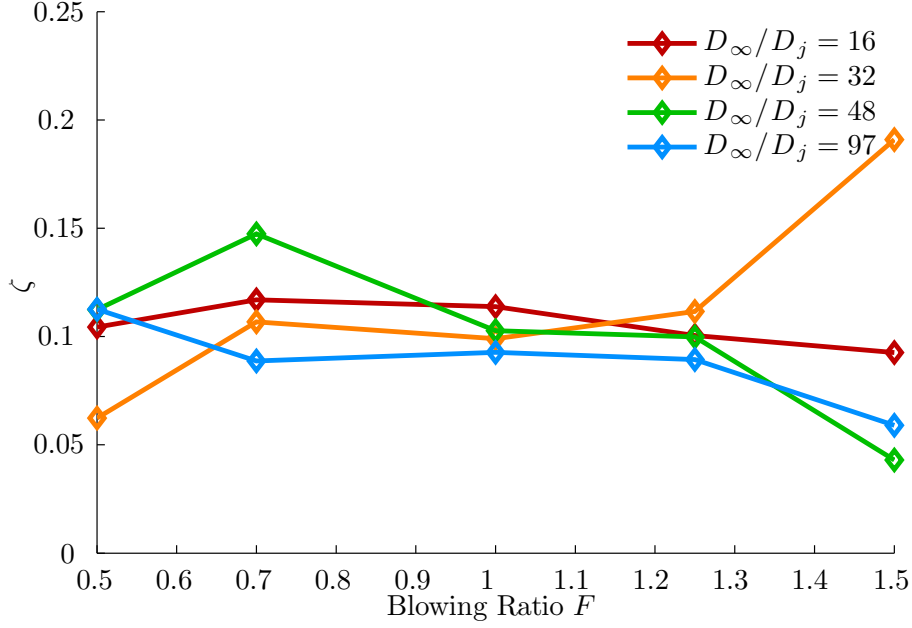


Figure 33: Area-averaged adiabatic effectiveness vs. blowing ratio with high density ratio.

the curve fit in Eq. 109 does not imply the same trend. Replacing  $F$  with  $\sqrt{I DR}$ , according to the definition, would not give a better indicator of the effect of  $DR$  on  $\zeta$ .

The exponent of curvature  $c$  has dropped by almost a factor of 3. This indicates a reduced dependence of  $\zeta$  on curvature. Curvature is still beneficial overall, though just not as beneficial as at lower  $DR$ .

Figure 34 compares different blowing ratios for the same coupon with a high density ratio. These figures help the reader to see the similar profiles at all blowing ratios with the high density ratio. The trend of the highest curvature having lower performance at low blowing ratios is still present. Further, the lines of  $\eta_{span}$  are closer together across the range of blowing ratios when compared to the lower density ratio figures. Performance is also slightly better across all blowing ratios, which may be attributed to the denser coolant resisting performance degradation in the presence of strong turbulence better than the low  $DR$  cases.

Individual comparisons of density ratio for the  $\alpha = 90^\circ$  cases at each blowing ratio and curvature can be found in App. A.6 (p. 142).

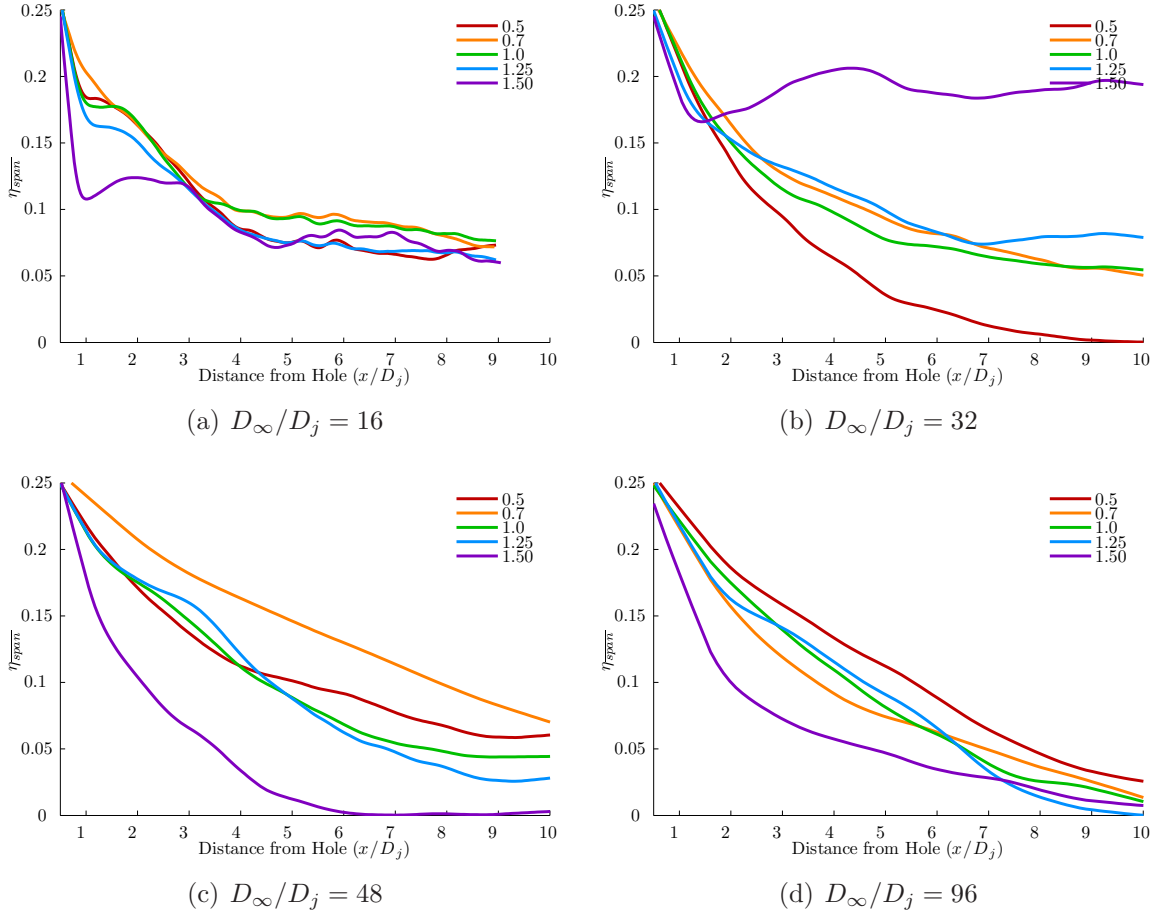


Figure 34: Effect of varying blowing ratio  $F$  at different curvature ratios with a high density ratio. Each colored line represents a different blowing ratio. Density ratio  $DR = 1.76$ .



#### 5.4 Interactions Between Variables

It is important to determine if any other interactions between the tested variables exist. A Buckingham- $\pi$  approach is taken with all of the tested configurations for the 90° compound injection angle geometry. In general, the Buckingham- $\pi$  approach will yield a minimum set of non-dimensional parameters which, taken together, will describe the entire space of tested configurations. The minimum number of non-dimensional parameters will be equal to the number of variables minus the number of physical dimensions. These parameters will generally consist of a product of dimensional values raised to exponents which will result in a non-dimensional number. The experiments performed here were performed using non-dimensional numbers. Therefore the required number of parameters required to describe the system is equal to the number of experimental variables: blowing ratio, curvature ratio, pressure gradient magnitude, and density ratio.

To discover any interactions between radial curvature, pressure gradient and density ratio, the general Buckingham- $\pi$  form is proposed:

$$\zeta = a \left( \frac{D_\infty}{D_j} \right)^c F^f (1 - K)^k DR^d \quad (110)$$

where  $K$  is the dimensionless pressure gradient as given in Eq. 36 (p. 36). The form  $(1 - K)$  is chosen as a term because  $K$  can be zero or negative for favorable pressure gradients, but not very close to one for air. This choice should ensure a more stable curve fit and relevant data points where  $K = 0$ . If the data from Figs. 26, 29, and 32 are plotted together, the resulting data set allows one to calculate a curve fit for all the data which takes into account the effects of curvature, pressure gradient and density ratio. This data set is shown in Fig. 35, and the resulting coefficients are given in Table 6 (p. 121) and this equation:

$$\zeta = 0.19 \left( \frac{D_\infty}{D_j} \right)^{-0.21} F^{-0.33} (1 - K)^{4.2} DR^{0.10} \quad (111)$$

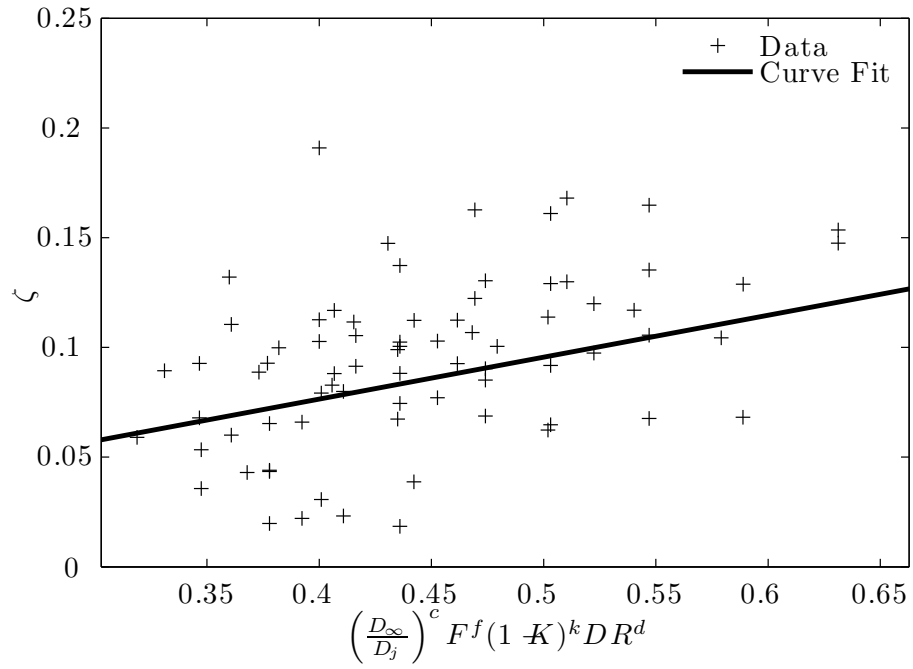


Figure 35: Area-averaged adiabatic effectiveness vs. new curvature parameter including all tested phenomena. The coefficients for the 90° compound injection case are given in Table 6 (p. 121).

### 5.5 Zero Compound Injection Angle Results

The results to follow are for the cases where there is no compound injection, in other words the only angle between the coolant and free-stream flow is  $30^\circ$  normal to the surface in the free-stream direction. It seems obvious that if no component of the coolant velocity is in the curvature direction, the effect of wall curvature on the coolant jet should be much smaller. There is some spreading of the coolant jet as it exits the coolant hole which has a velocity component in the direction of curvature. This velocity component is small, so the effect of curvature on the jet is expected to be small as well. The experimental data support this expectation.

Span-wise averaging the adiabatic effectiveness over a different length changes the magnitude, but not the shape, of  $\eta_{\overline{span}}$ . The compound injection angle  $\alpha = 0^\circ$  cases were span-wise averaged over a different range than the  $\alpha = 90^\circ$  data. This is acceptable because no direct comparisons were made between the two angles. In each case the span-wise averaged adiabatic effectiveness,  $\eta_{\overline{span}}$ , defined as

$$\eta_{\overline{span}}(y) = \frac{1}{\xi_2 - \xi_1} \int_{-\xi_1}^{\xi_2} \eta_f dx \quad (16)$$

was generated based on four hole diameters in the span-wise direction, or  $\xi_2 - \xi_1 = 4$ .

The area averaged adiabatic effectiveness,  $\zeta$ , defined as

$$\zeta = \frac{1}{(\xi_2 - \xi_1)(\gamma_2 - \gamma_1)} \int_{-\xi_1}^{\xi_2} \int_{-\gamma_1}^{\gamma_2} \eta_f dx dy \quad (17)$$

was calculated using four hole diameters in the span-wise direction and from one to ten hole diameters downstream of the hole center ( $\xi_2 - \xi_1 = 4$  and  $\gamma_2 - \gamma_1 = 9$ ).

The change in the area used for span-wise averaging has the effect of doubling the magnitude of  $\eta_{\overline{span}}$  and  $\zeta$  when compared to the results already shown. The change was made to give more realistic values of  $\eta_{\overline{span}}$  in the following plots.

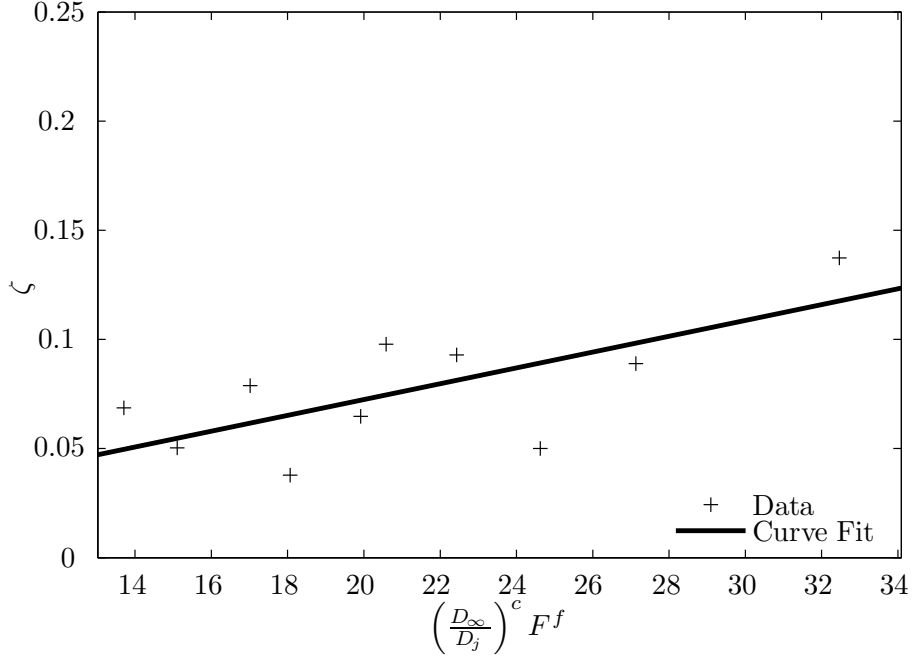


Figure 36: Area-averaged adiabatic effectiveness vs. new curvature parameter as given by Eq. 112. The coefficients for the  $0^\circ$  compound injection case are given in Table 6 (p. 121).

*Curvature Effects.* Span-wise, or radial, curvature has much less of an effect on coolant without compound injection. The overall performance is In Fig. 36 this curve fit is plotted over the data:

$$\zeta = 0.004 \left( \frac{D_\infty}{D_j} \right)^{0.68} F^{-0.53} \quad (112)$$

The coefficient  $c$  is now positive when compared to the  $\alpha = 90^\circ$  cases, suggesting an increase in radial curvature in this hole configuration has a detrimental effect on  $\zeta$ . This effect was not predicted in the simulations, likely another result of increased turbulence in the experiments. The jet is thinned due to the encroaching wall, as predicted by the simulations, but since the free-stream turbulence increases the rate at which the jet dissipates into the free-stream, the longer jet which exists in the higher curvature case is no longer present as far downstream. The combination of a

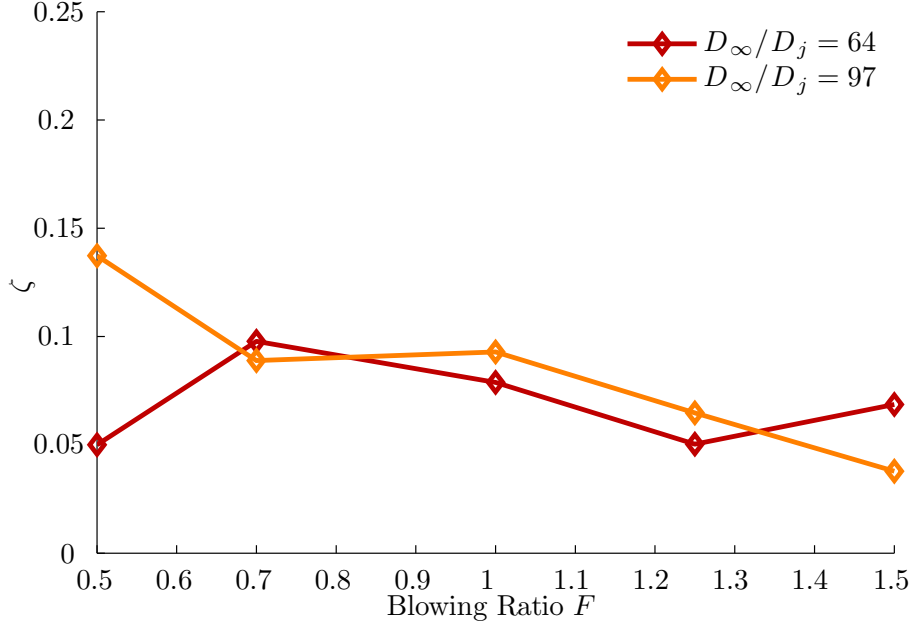


Figure 37: Area-averaged adiabatic effectiveness vs. blowing ratio,  $\alpha = 0^\circ$  .

thinner jet and a high dissipation results in worse performance for the high curvature case.

Figure 37 displays a reduced dependence of  $\zeta$  on curvature in the  $0^\circ$  compound injection case, as shown by the closeness of the curves at the middle blowing ratios ( $F=0.7$  to  $1.25$ ). Again at the lowest blowing ratio it seems the higher curvature has a performance reduction, possibly due to increased mixing. Further, the highest blowing ratio shows an increase in performance with increased curvature, possibly due to the wall catching some of the spreading jet better than the low curvature case.

Comparisons of the curvature effect on  $\eta_{\overline{span}}$  at each blowing ratio are shown in Fig. 38. At each of the displayed blowing ratios the curves of  $\eta_{\overline{span}}$  display very similar shapes. This similarity, in conjunction with the close magnitudes of  $\zeta$  just discussed, further illustrates the diminished effect of curvature on  $\zeta$ . The small value of coefficient  $a = 0.004$  in Eq. 112 is more evidence of reduced impact of curvature. Figure 39 gives a comparison of  $\eta_{\overline{span}}$  at both curvatures for different blowing ratios. These plots show the  $0^\circ$  compound injection case still has worse performance when

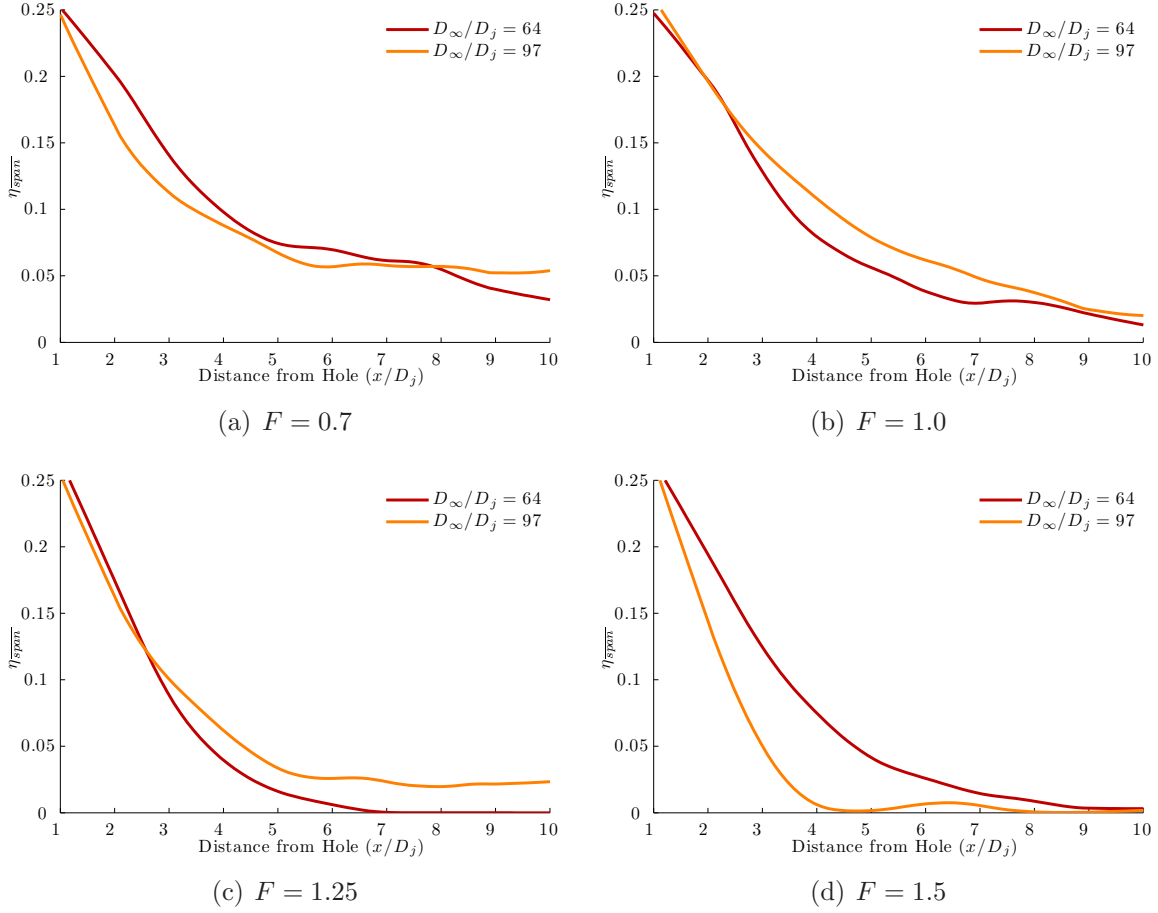


Figure 38: Effect of varying radial curvature at a range of blowing ratios,  $F$ , with no compound injection. Each colored line represents a different curvature ratio  $D_\infty/D_j$ .

compared to the  $90^\circ$  cases, which is expected based on flat plate data. Curvature appears to have no effect on this trend.

*Stream-wise Pressure Gradient Effects.* As with the  $90^\circ$  compound injection cases, a strong favorable stream-wise pressure gradient has a beneficial effect on  $\zeta$  overall, as the curve fit in Fig. 40 suggests. This is obvious by the increase in  $a$  over the non-pressure gradient cases. The pressure gradient pushes the coolant closer to the wall, which increases effectiveness. Furthermore, the effect of curvature on  $\zeta$  is reduced, though the fact  $c$  is positive still highlights the turbulent mixing which makes curvature detrimental in this configuration. The effect of blowing ratio on  $\zeta$  is nearly unchanged. The coefficients are listed in Table 6 (p. 121).

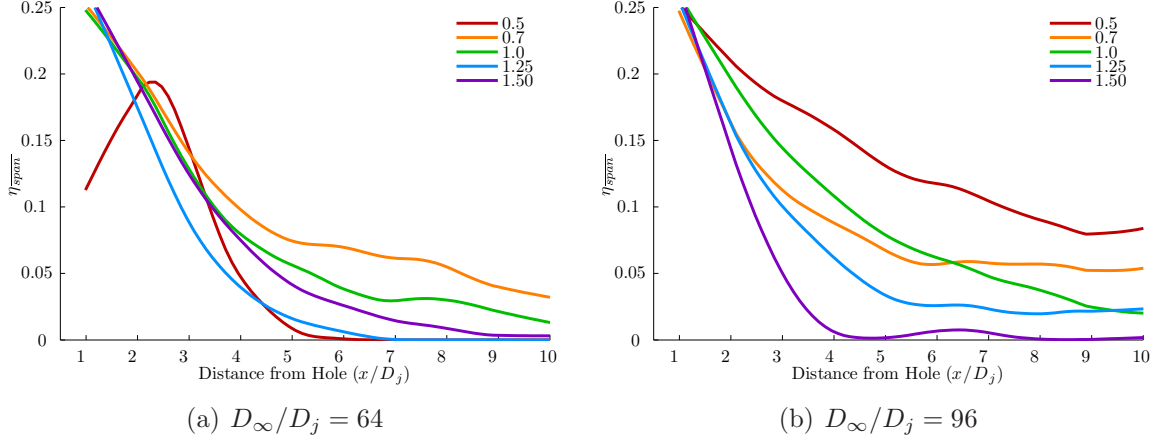


Figure 39: Effect of varying blowing ratio  $F$  at different curvature ratios with no compound injection. Each colored line represents a different blowing ratio.

We again employ the familiar form of Eq. 105 to determine the performance  $\zeta$  as a function of  $F$  and  $D_\infty/D_j$  for the zero compound injection case with a strong favorable stream-wise pressure gradient:

$$\zeta = .02 \left( \frac{D_\infty}{D_j} \right)^{0.37} F^{-0.40} \quad (113)$$

This curve is plotted over the data in Fig. 40. The parameter  $a$  has increased five-fold over the zero pressure gradient case, indicating  $\zeta$  is affected more by the curvature and blowing ratio than without the pressure gradient.

Figure 41 shows a change from the  $90^\circ$  cases. There is a blatant concave-down shape to the data which is not apparent in either Figs. 30 or 25. This signals a return to the trend explained in Sec. 2.5 (p. 26) in which higher blowing ratios experience a performance benefit over lower blowing ratios in the presence of a favorable pressure gradient. The data does not exactly correspond to theory, which says lower blowing ratios are penalized and higher ones are rewarded by the pressure gradient. There is some unknown interplay between the pressure gradient and the blowing ratio which is influenced most likely by the high free-stream turbulence. Further study of the effect of high free-stream turbulence on pressure gradient interaction is necessary before one

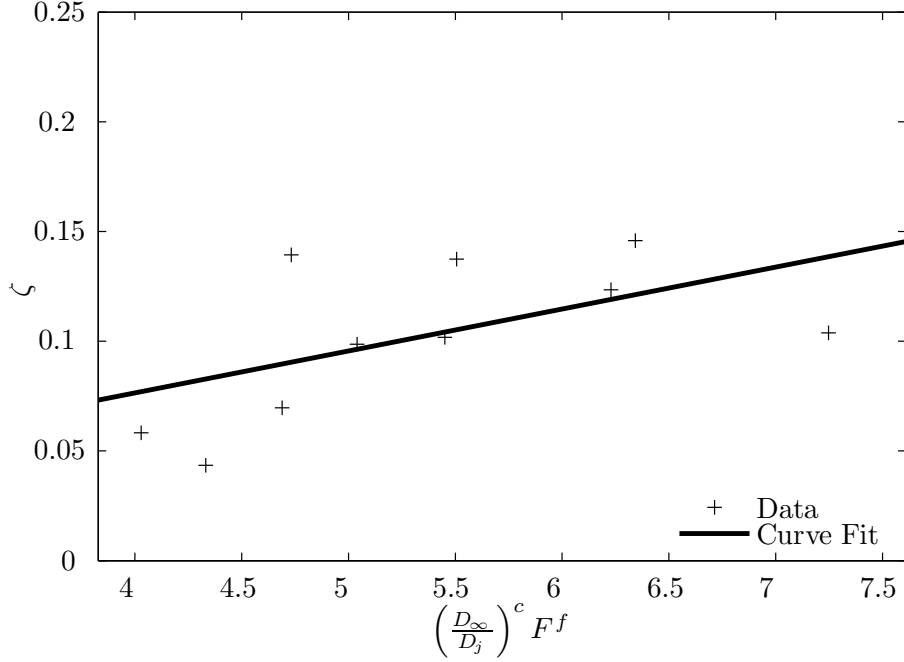


Figure 40: Area-averaged adiabatic effectiveness with strong favorable pressure gradient vs. new curvature parameter as given by Eq. 113. The coefficients for the  $0^\circ$  compound injection case are given in Table 6 (p. 121).

can make definitive conclusions regarding the pressure gradient theory presented in Sec. 2.5.

Figure 42 gives a comparison of  $\eta_{\overline{span}}$  at each curvature for different blowing ratios. Overall  $\eta_{\overline{span}}$  is higher than the zero pressure gradient case. There is less decay downstream of the hole with the pressure gradient, especially at the lower blowing ratios ( $F=0.5$  to  $1.0$ ). Performance is still better overall with less curvature. The high curvature, high blowing ratio cases (the blue and purple lines in Fig. 42(a)) decay to zero quickly, while the same lines in Fig. 42(b) have slightly better performance. The higher curvature is not good for  $\eta_{\overline{span}}$  at these blowing ratios, though the performance is low for both curvatures anyway.

Individual comparisons of pressure gradient for the  $\alpha = 0^\circ$  cases at each blowing ratio and curvature can be found in the appendix (p. 147).



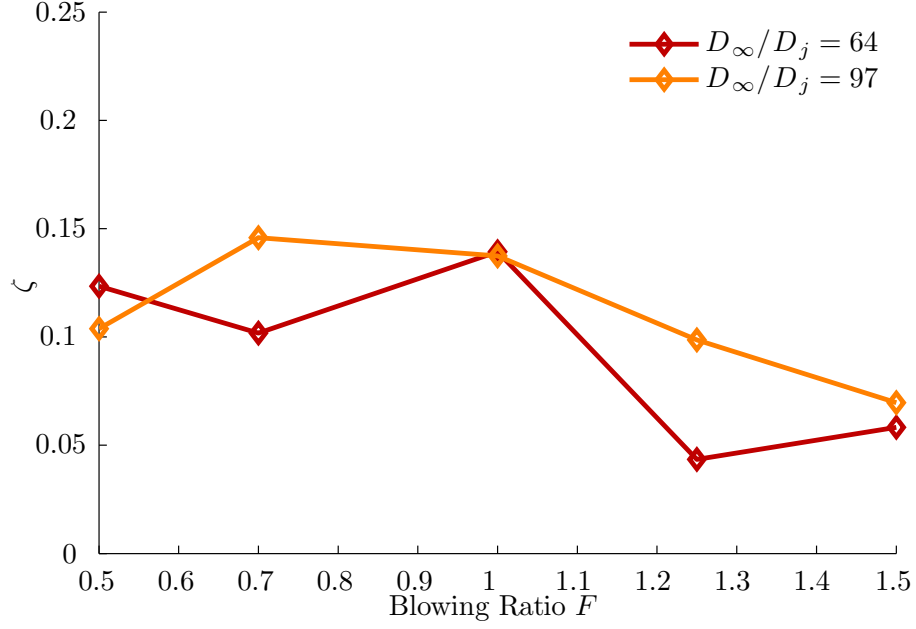


Figure 41: Area-averaged adiabatic effectiveness vs. blowing ratio with strong pressure gradient,  $\alpha = 0^\circ$ .

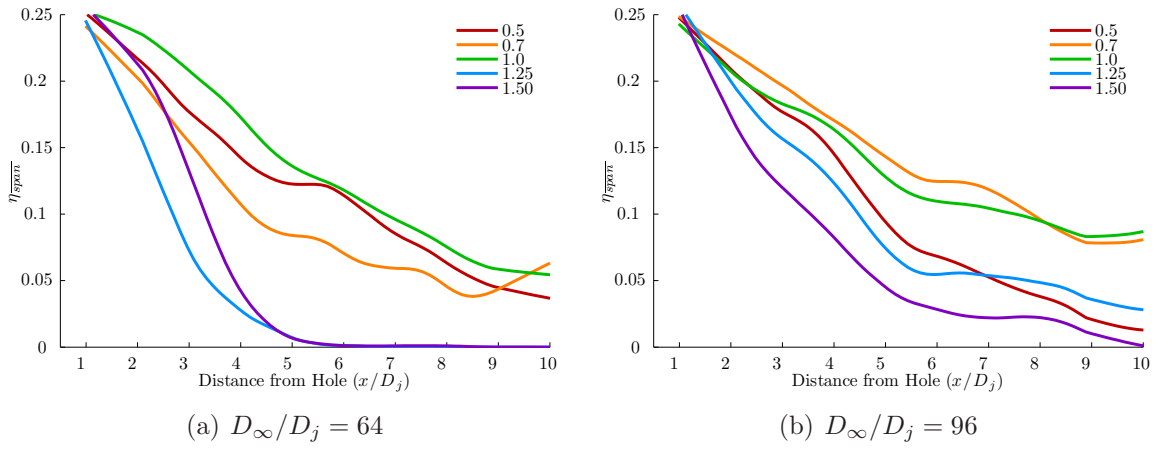


Figure 42: Effect of varying blowing ratio  $F$  at different curvature ratios with a strong favorable stream-wise pressure gradient and no compound injection. Each colored line represents a different blowing ratio. Pressure gradient  $K = 2.1 \times 10^{-5}$ .

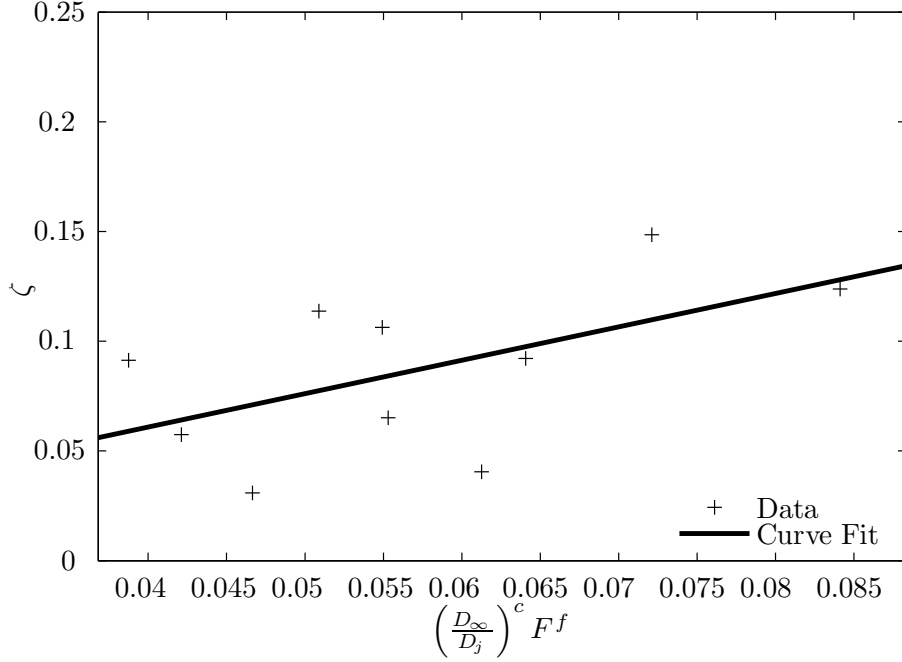


Figure 43: Area-averaged adiabatic effectiveness with high density ratio vs. new curvature parameter, as given by Eq. 114. The coefficients for the  $0^\circ$  compound injection case are given in Table 6 (p. 121).

*High Density Ratio Effects.* Performance is clearly affected by density ratio in a similar manner to the  $\alpha = 90^\circ$  cases. While a high  $DR$  made the the  $\alpha = 90^\circ$  cases insensitive to changes in curvature and the trend appears here as well. It is less obvious given the relative independence from curvature effects the  $\alpha = 0^\circ$  cases have already exhibited. The higher  $DR$  seems to improve performance overall when compared to the low  $DR$  cases.

When Eq. 105 is applied to the data, the result is

$$\zeta = 1.52 \left( \frac{D_\infty}{D_j} \right)^{-0.67} F^{-0.46} \quad (114)$$

This curve is plotted over the data in Fig. 43.

Figure 25 displays  $\zeta$  over the range of blowing ratios. It is interesting to note the response of  $\zeta$  to  $F$  is completely inverted with high density ratio (when compared to the favorable pressure gradient case, which had a concave down shape). This may

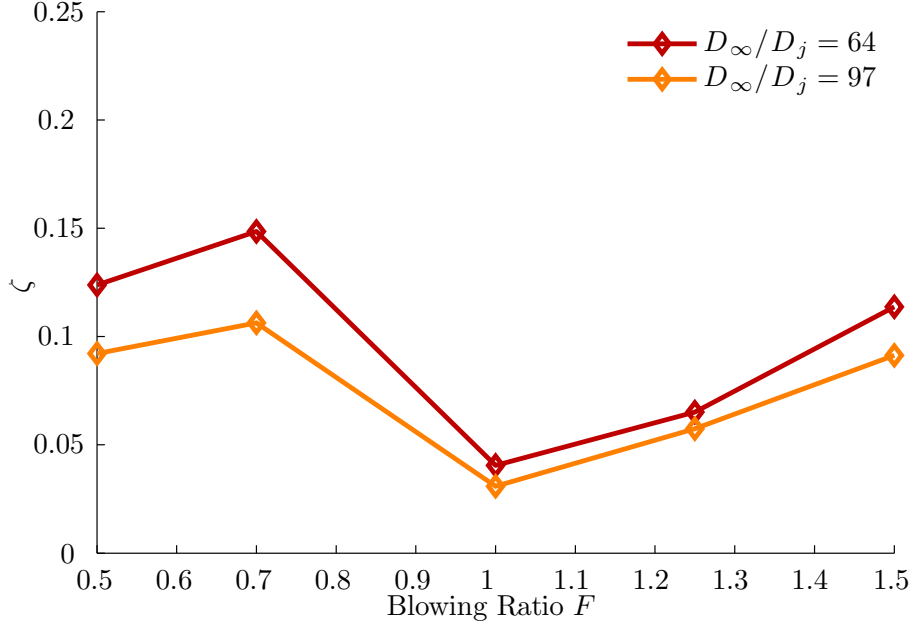


Figure 44: Area-averaged adiabatic effectiveness vs. blowing ratio with high density ratio,  $\alpha = 0^\circ$  .

be due to a changing expansion rate of the jet caused by the density gradient, which has been observed in previous density ratio studies. [5] In other words, for  $\alpha = 0^\circ$  , the plot of  $\zeta$  with high density ratio is concave down with a minimum around  $F = 1.0$ , while the plot of  $\zeta$  with strong pressure gradient is concave up with a maximum around  $F = 0.7$ . One should not anticipate the effects to cancel each other out should the two phenomena be tested simultaneously, since there may be other effects at play. This figure again shows the diminished effect of curvature when there is no compound injection, since the red and orange curves are very close and trend together.

Individual comparisons of density ratio for the  $\alpha = 0^\circ$  cases at each blowing ratio and curvature can be found in the appendix (p. 149).

## 5.6 Heat Flux Reduction Effects

Since the transient technique yields both adiabatic wall temperature and heat flux coefficient along the surface, the net heat flux reduction (NHFR) is directly available. Recall from p. 13, NHFR is defined as

$$\text{NHFR} = 1 - \frac{h_f}{h_o} \left( 1 - \frac{\eta_f}{\phi} \right) \quad (24)$$

where  $\phi$  is the overall effectiveness, defined on p. 13 as

$$\phi = \frac{T_\infty - T_S}{T_\infty - T_c} \quad (23)$$

Gas turbine film cooling researchers generally assume  $\phi = 0.6$  based on typical system operating temperatures. [5] Rockets can operate at a wide range of wall temperatures and coolant temperatures when compared to gas turbines, so  $\phi$  could theoretically vary from 0.5 to 0.8, depending on the physical configuration and where in the rocket film cooling is employed. A likely value for  $\phi$  in the throat region is  $\phi = 0.7$ . The following NHFR results assume this value for  $\phi$ .

Recall further the area-averaged NHFR is defined by Rutledge [76] as

$$\overline{\Delta q_{r,area}} = 1 - \frac{\int_{-\Delta x}^{\Delta x} \int_{-\Delta y}^{\Delta y} h_f (\phi - \eta) dx dy}{\int_{-\Delta x}^{\Delta x} \int_{-\Delta y}^{\Delta y} h_o \phi dx dy} \quad (67)$$

This form is preferred to area-averaging NHFR directly. This form tends to increase the expected area-averaged NHFR by 0.1% to 0.5% over area-averaging NHFR directly for this data. Though NHFR is averaged over an area, the final result is not divided by any area as the area terms in the numerator and denominator of the second term in Eq. 67 cancel each other.

Figure 45 shows the area-averaged NHFR vs. blowing ratio for varying curvature ratios with 90° compound injection. Increasing the curvature ratio appears to improve NHFR at higher blowing ratios ( $F \geq 1$ ), but has little effect at lower blowing ratios, as shown in Fig. 45. This relationship holds even though there is a negative effect on  $\eta$  due to extremely high curvature from blowing ratios between 0.7 and 1. These two facts imply the heat flux is also lower in regions of low  $\eta$  when the low value of  $\eta$  is caused by curvature, which is verified by looking at the raw data.

Though the magnitudes of NHFR are quite higher in the experimental results, a qualitative comparison may be made with the computational results given in Fig. 12 (p. 56). The general trend is a nearly linear decrease in NHFR with increasing blowing ratio, where NHFR transitions from beneficial to detrimental somewhere between  $F = 0.7$  and  $F = 1.0$ . The differences between simulation and experiment are obvious. First, the magnitude of NHFR is greater in the experimental results when compared to the computational at all curvatures. Further, there is a definite improvement in NHFR due to increasing curvature which was present in the computational data, but not as pronounced as in the experimental data. This change in magnitude and curvature effect may signal a free-stream turbulence dependence on NHFR, or may represent a limitation of two-equation turbulence models in predicting heat transfer coefficients.

There is no discernible difference in NHFR due to increasing curvature without compound injection as Fig. 46 clearly shows. Further, the character of NHFR vs. blowing ratio with no compound injection follows the 90° compound injection jets since NHFR decreases nearly linearly with increasing blowing ratio.

NHFR is affected greatly with the presence of a strong favorable stream-wise pressure gradient, as shown in Fig. 47. The magnitude of NHFR at low blowing ratios is increased over the no pressure gradient case. Further, Fig. 30 (p. 97) shows the adiabatic effectiveness is also increased over the no pressure gradient case. These facts imply the heat flux is not as affected by the pressure gradient as the adiabatic

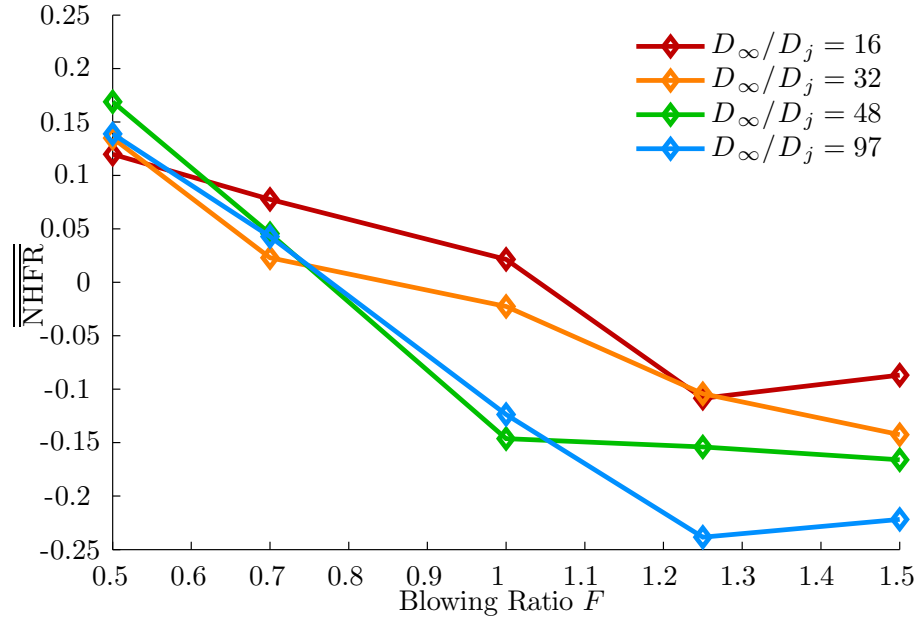


Figure 45: Area-averaged NHFR vs. blowing ratio,  $\alpha = 90^\circ$

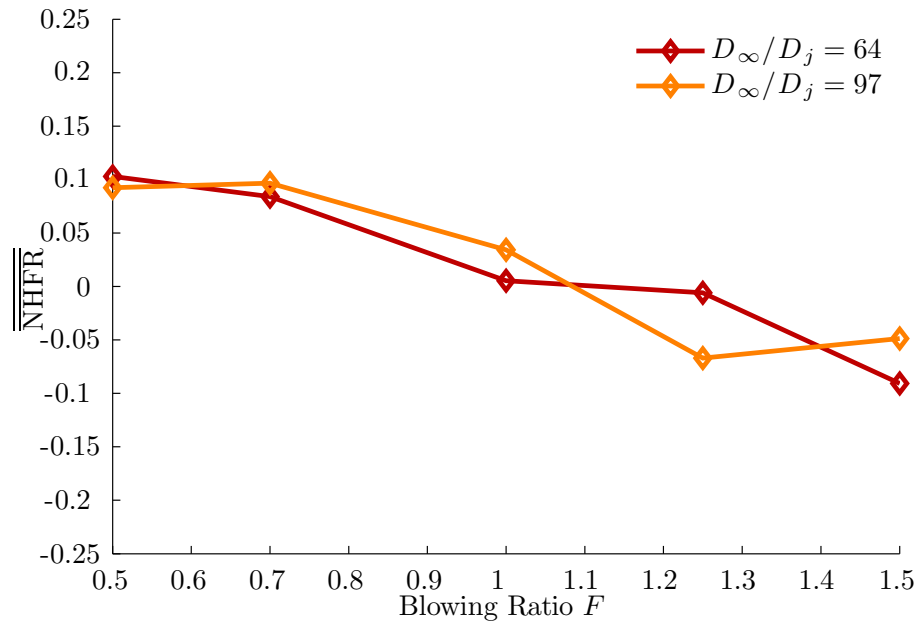


Figure 46: Area-averaged NHFR vs. blowing ratio,  $\alpha = 0^\circ$

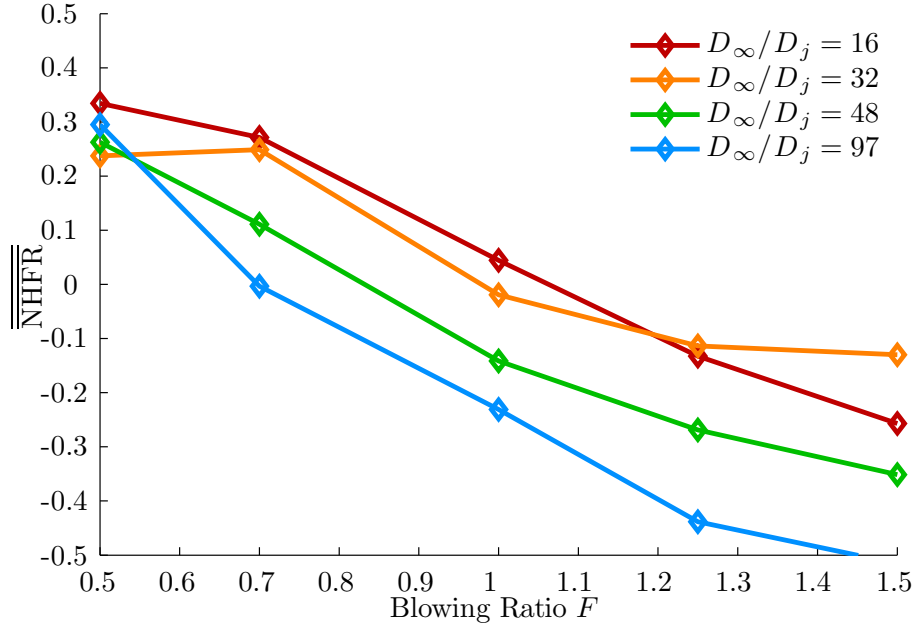


Figure 47: Area-averaged NHFR vs. blowing ratio with strong favorable stream-wise pressure gradient

effectiveness, which yields a higher NHFR overall. Increasing curvature improves NHFR performance, just like the no pressure gradient case. Similarly, the performance at all curvatures is similar at low blowing ratios, just like the no pressure gradient case.

If the density ratio is increased from 1.1 to 1.8 the resulting NHFR is shown in Fig. 48. As in the adiabatic effectiveness data, the blowing ratio at which performance begins to strongly degrade has been increased by the higher density flow. At the higher blowing ratios, the higher curvature is performing better than lower curvatures, as with the lower density ratio tests. Interestingly, the highest two curvatures never experience negative NHFR, which implies even higher increases in density ratio could make NHFR more beneficial at even higher blowing ratios. At every blowing ratio and curvature, NHFR is increased when compared to the lower density ratio cases.

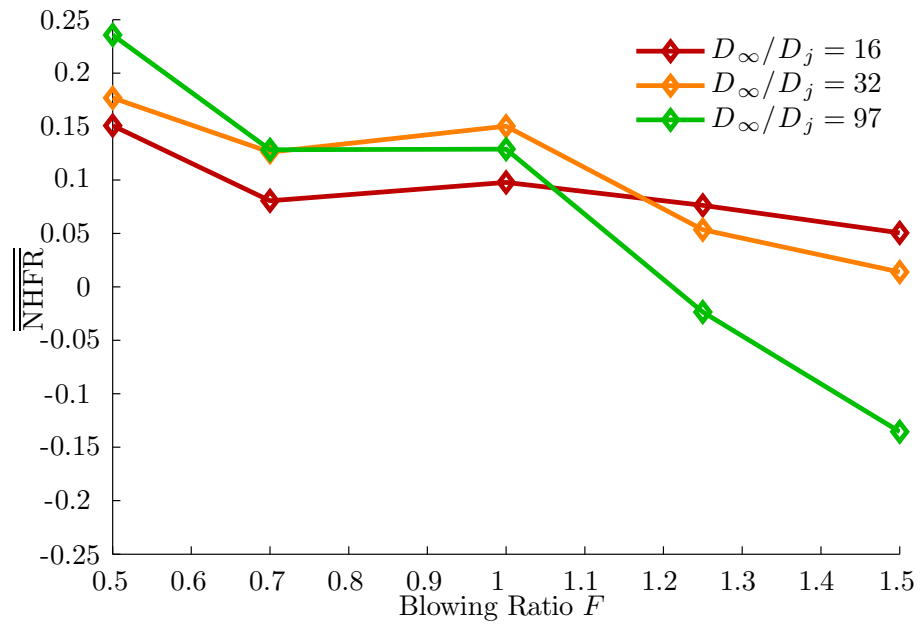


Figure 48: Area-averaged NHFR vs. blowing ratio with high density ratio



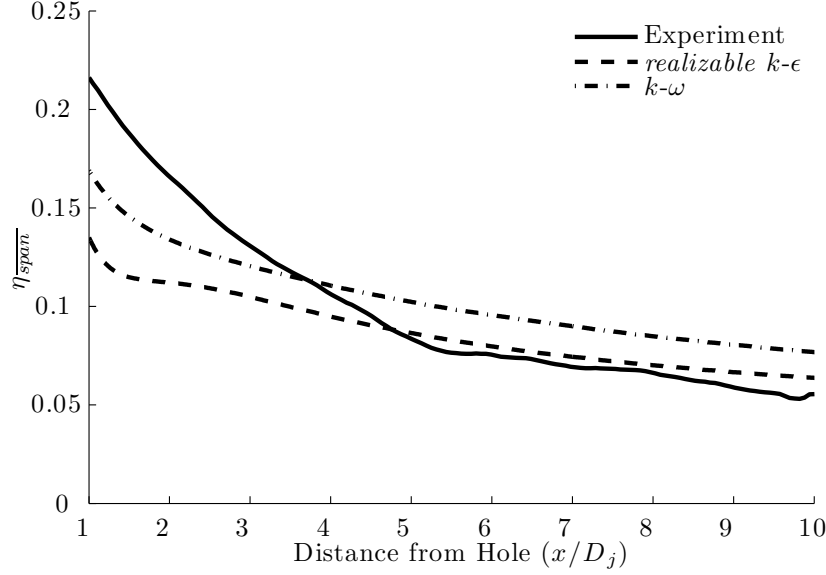


Figure 49: Comparison of experimental data to simulation.

### 5.7 Comparison to Simulation

Two simulations were run at experimental conditions:  $Tu = 0.26$  and  $\Lambda = 0.056 \text{ mm}$ . Other parameters for the simulations were zero pressure gradient,  $DR \approx 1$ ,  $F = 0.5$ , and  $D_\infty/D_j = 32$ . The same grids and solver parameters as explained in Sec. 3.2 (p. 47) were used. One simulation used the  $k - \omega$  model for turbulence while the other used the *realizable*  $k - \epsilon$ . The experimental data were compared to these simulations to determine whether the  $k - \omega$  model, typically used for curvature modeling, was more suitable for future Computational Fluid Dynamics (CFD) studies than the *realizable*  $k - \epsilon$  model, which is frequently used in film cooling studies because of its superior jet-modeling fidelity (see Sec. 3.2, p. 49).

Figure 49 shows the results of this simulation. It is clear both models under-predict the cooling effectiveness immediately downstream of the hole, which signals a possible limitation for two-equation turbulence models under these test conditions. Further downstream past 5 hole diameters from the hole center, the *realizable*  $k - \epsilon$  model yields  $\eta_{span}$  results much closer to the experiment than the  $k - \omega$  model. The data confirm the previous research mentioned in Sec. 3.2.

## 5.8 Summary

The data showed there is a relationship between radial curvature and area averaged adiabatic effectiveness. The empirical relationships determined in this chapter may be used to predict the performance on the surface of a radially cooled wall, provided high turbulence is expected. The coefficients for these empirical relationships are presented again in Table 6, and apply to the now familiar form for predicting the area averaged adiabatic effectiveness,  $\zeta$ :

$$\zeta = a \left( \frac{D_\infty}{D_j} \right)^c F^f \quad (105)$$

Again, the high pressure gradient coefficients are valid when the dimensionless pressure gradient  $K = 2.1 \times 10^{-5}$ . The high density ratio coefficients work when  $DR = 1.76$ .

When the compound injection angle  $\alpha = 90^\circ$ , increased curvature has a generally beneficial effect of  $\zeta$ , and is influenced by the blowing ratio. After a certain curvature is reached, adiabatic effectiveness tends to decrease when compared to less curved cases at low blowing ratios. Inducing a strong stream-wise favorable pressure gradient is beneficial to  $\zeta$ , increasing performance at all blowing ratios. Increasing the density ratio generally improves performance as well, though both curvature and blowing ratio have limited effects on  $\zeta$  in this configuration.

Increasing curvature when  $\alpha = 0^\circ$  has an opposite and smaller effect on  $\zeta$  than when  $\alpha = 90^\circ$ . In other words, increasing radial curvature is detrimental to  $\zeta$ . As with the  $\alpha = 90^\circ$  case, inducing a strong stream-wise favorable pressure gradient is beneficial to  $\zeta$  at all blowing ratios when  $\alpha = 0^\circ$ . Increasing the density ratio improves performance, again due to the lower velocity required to maintain the blowing ratio.

Increasing radial curvature with compound injection has a beneficial effect on net heat flux reduction (NHFR) at all blowing ratios, with increasing benefit when blowing ratio is greater than 1. Without compound injection there is no benefit or detriment to NHFR. Imposing a strong favorable stream-wise pressure gradient

Table 6: Summary of Fit Coefficients for Experimental Data

	$\alpha$	$a$	$c$	$f$	$sse$
Curvature Study	90°	0.1941	-0.2806	-0.5871	0.0154
Pressure Gradient Study	90°	0.2491	-0.2352	-0.4607	0.0194
Density Ratio Study	90°	0.1556	-0.1190	0.0110	0.0203
Curvature Study	0°	0.0036	0.6815	-0.5333	0.0042
Pressure Gradient Study	0°	0.0191	0.3737	-0.3964	0.0076
Density Ratio Study	0°	1.5222	-0.6715	-0.4575	0.0092

improves NHFR at low blowing ratios when compared to the no pressure gradient case, while the already low NHFR at higher blowing ratios is made even worse with the pressure gradient.

## VI. Conclusions and Future Work

Radial curvature changes the relationship between adiabatic effectiveness and blowing ratio. This change was predicted in simulation, and several experiments were run to confirm it. In addition, the effects of favorable pressure gradients and high density ratios were experimentally investigated with this rocket-specific geometry. In running these experiments, some improvements were made to the technique by which adiabatic wall temperature and heat flux are simultaneously acquired. These achievements add to the body of knowledge regarding discrete film cooling in rocket chambers and fulfill the goals enumerated in Sec. 1.2 (p. 5).

This study presented several new ideas and data regarding effusion cooling. The Rannie transpiration cooling model in Eq. 33 (p. 24) was shown to predict the coolant distribution of a full-coverage film cooled plate. A correction based on the hole spacing was required. This result shows separate experiments are not necessary to predict full-coverage film cooling performance since transpiration cooling models will provide this information.

Simulations of radially curved walls showed the effects of radial curvature on film cooling adiabatic effectiveness,  $\eta_f$ , and net heat flux reduction (NHFR) are greatest when the film is injected at a 90° compound injection angle. The anticipated change in  $\eta_f$  and NHFR is a general increase in performance when the wall radius of curvature decreases relative to the hole diameter, or when decreases. Jets with less compound injection, like 45°, or no compound injection are unaffected by increasing radial curvature.

Using these simulation results as a guideline, experiments revealed the trend for  $\eta_f$  to increase with increasing radial curvature is only valid up to a certain curvature. The results showed an increase in  $\eta_f$  up to  $D_\infty/D_j = 32$ . This improvement occurs because the span-wise component of jet velocity encounters a wall which helps the free-stream flow turn the coolant, resulting in a wide swath of coolant which stays attached to the wall for longer. A decrease in  $\eta_f$  when curvature increased to  $D_\infty/D_j = 16$  was observed, especially at low blowing ratios. This detriment is due to the wall arresting

the lateral spread of the coolant enough to offset the benefits of a faster turning jet. NHFR was found to increase with increasing curvature up to  $D_\infty/D_j = 16$ , which implies the heat flux coefficient decreases as  $D_\infty/D_j$  decreases, enough to counteract the decrease in  $\eta_f$  encountered at the lowest  $D_\infty/D_j$ .

More experiments showed a strong, favorable, stream-wise pressure gradient has a beneficial effect at all curvatures and at all blowing ratios. This result seems to conflict with Dellimore [49], who said favorable pressure gradients are beneficial at high blowing ratios, but detrimental at low ones. There are two distinct differences between these results and Dellimore's: the free-stream turbulence intensity in these experiments was 26%, much higher than any previously tested film cooling experiments; and the pressure gradient severity was  $2.1 \times 10^{-5}$ , also much higher than previous experiments. These test conditions are similar to those encountered in liquid-fueled rockets. Increasing the density ratio (DR) from 1.2 to 1.8 did not change curvature's effect on  $\eta_f$ . Higher DR did increase  $\eta_f$  at the higher blowing ratios.

These conclusions are based on data gathered using a technique whereby adiabatic wall temperature and heat flux coefficient are acquired simultaneously, in a method similar to Ou's [78]. To increase the accuracy of this technique, three improvements were made. First, the two-point solutions typically generated by this method were replaced with a 300-point non-linear least squares correlation, which reduced the curve fit uncertainty by at least one order of magnitude. Second, temperature data from the un-cooled region upstream of the hole was used to decrease the uncertainty in the start time, which reduced the uncertainty in heat flux coefficient from 10% to 1% due to time errors alone. Third, the constant adiabatic wall temperature boundary condition was correctly applied to the model, which for the first time accounted for coolant temperature drift.

### ***6.1 Summary of Work Accomplished***

The following work added considerably to the understanding of discrete film cooling in rockets:

- Simulated the variation of hole pitch and size of normally injected discrete film cooling jets to determine the utility of a transpiration cooling model to predict cooling effectiveness (p. 42);
- Determined the effect of radial wall curvature on adiabatic effectiveness at both  $0^\circ$  and  $90^\circ$  compound injection angles (p. 88);
- Determined the effect of a strong stream-wise favorable pressure gradient in the presence of radial wall curvature on adiabatic effectiveness at both  $0^\circ$  and  $90^\circ$  compound injection angles (p. 96);
- Determined the effect of a high density ratio in the presence of radial wall curvature on adiabatic effectiveness at both  $0^\circ$  and  $90^\circ$  compound injection angles (p. 98).

Several improvements were also made to the technique explained in Sec. 4.1 (p. 60):

- Used a multi-point, non-linear least squares fit on data rather than a two-point solver (p. 72);
- Correctly applied the constant adiabatic wall temperature boundary condition (p. 73);
- Showed a way to identify the appropriate start time and quantify its uncertainty (p. 75);
- Provided analysis on thermal property effects for suitable material choice and time-scale choice for test setup, and provided analysis for the lateral conduction error when using this technique (p. 83).

## ***6.2 Transient Technique Lessons Learned***

Not all of the data gathered in the course of this experiment can be plotted. Some very useful knowledge, usually serendipitous, was gained by testing and retesting the method over a period of time. Here I will put down some of the qualitative lessons I learned while performing these experiments.

- Low turbulence would result in data points (temperature over time) which more smoothly fit the solution curve, which would allow for a better and faster curve fit when solving for  $T_{aw}$  and  $h$ .
- Higher heat flux coefficient  $h$  would provide more observations of the non-dimensional transient curve (like in Fig. 21, p. 73) for the same amount of testing time. Increasing  $h$  would also lower the error due to lateral conduction as shown in Sec. 4.6 (p. 78). Since higher Reynolds number ( $Re$ ) need to be tested to discover its effect on cooling effectiveness,  $h$  would naturally increase and provide both of these benefits.
- A larger hole would result in lower error due to conduction since the surface area-volume ratio would decrease. This benefit can be easily obtained by simply scaling up the test article size for a given curvature, within the limits of the testing apparatus. A change in the hole diameter  $D_j$  means the coolant channel wall area changes by  $\pi L D_j$  and the coolant volume by  $\pi L D_j^2/4$ , where  $L$  is the length of the coolant channel. The heat transfer to the fluid from the wall varies with channel wall area, but the coolant temperature change varies with coolant volume. Therefore the error due to coolant temperature drift in the transient method will decrease proportional to  $4/D_j$ .
- The ideal material for use with this technique is one with low thermal conductivity, low density, and low specific heat capacity (for more on this, see Sec. 4.6, p. 78). This combination of properties drives the thermal response of the material to much higher temperatures in much shorter times, which means conduction effects will be much less disruptive for a test of given duration, which maintains the validity of the one-dimensional (1-D) assumption vital to Eq. 71 (p. 61).
- It is critical the temperature be recorded at certain values of non-dimensional time ( $0.05 \leq h\sqrt{\alpha t}/k \leq 0.3$ ) to minimize the error in heat flux coefficient  $h$ . If

the temperature is not measured during these times, the uncertainty in  $h$  will be much higher than 20%.

- Since this study did not seek to optimize simulation techniques, only the *realizable*  $k - \epsilon$  turbulence model was used for the simulations presented in Chap. III. However, one case was run to compare this model to the  $k - \omega$  model and experimental results (p. 119). It seems both models under-predicted  $\eta_f$  immediately downstream of the hole, which implies a more advanced turbulence-modeling technique may be required for cases involving coolant jets with very high curvature or very high free-stream turbulence.

### 6.3 Future Work in Film Cooling/Curvature

Much more work can begin where this work ends:

- For the results presented in Section 3.1 (p. 42), another study of a similar geometry should be carried out, this time with a reservoir model and conducting walls. Heat flux comparisons can then be made, including a reduction in Stanton number ( $St$ ) or NHFR. Landis [17] showed transpiration cooling performance is nearly independent of the material and thermal properties of the porous medium when the pore size is sufficiently small. It is not known at what  $P/d$  material choice becomes important to heat flux reduction for full coverage film cooling. One should be able to obtain a general relation for Stanton number reduction, like in Eq. 39 (p. 29), based on hole pattern geometry.
- Computational Fluid Dynamics (CFD) simulations should continue for a range of test cases. For the case presented, it seems the  $k - \omega$  turbulence model over-predicted span-wise averaged adiabatic effectiveness away from the hole. The *realizable*  $k - \epsilon$  model under-predicted span-wise averaged adiabatic effectiveness near the hole. Further CFD should be performed at the same high turbulence levels associated with these experiments to see if other turbulence modeling techniques like Large Eddy Simulation (LES) or Direct Numerical Simulation



(DNS) do a better job of predicting effectiveness. Since rocket combustion chambers experience such a high turbulence intensity, it would be helpful to know which tools work best for film cooling predictions in this environment.

- Repeating each experiment at different turbulence intensities would answer the question of whether the changes in adiabatic effectiveness due to the presence of a strong favorable stream-wise pressure gradient were in part due to the change in turbulence characteristics, as shown by the hotwire tests presented in the appendix (p. 129). Turbulence has been shown to have a strong effect on coolant dissipation.
- Reynolds number has been shown to have an effect on transpiration cooling and film cooling. Of course the change in effectiveness due to Reynolds number in the presence of curvature has not been investigated. Any interactions between wall curvature and Reynolds number should be determined.
- If the coolant is fuel and the free-stream contains combustion products as in a rocket, then it is important to determine how quickly the coolant mixes with the free-stream to minimize the performance loss from using fuel as coolant instead of burning it. To measure the mixing, Planar Laser-Induced Fluorescence (PLIF) can be used to observe the species concentration of a coolant gas. In conjunction with Particle Image Velocimetry (PIV), the information gained from PLIF can be used to calculate the performance gain/loss from using fuel as coolant.

## Appendix A.

### A.1 Properties of Polyurethane foam

Polyurethane is a polymer chain joined by urethane, which is any of a group of organic compounds sharing the general structure  $-NH(CO)O-$ . Some relevant properties of this material are listed in Tab. 7. The parameter  $k \cdot \rho \cdot c$  is one which should be made as small as possible in transient tests in order to minimize testing time, which in turn minimizes the error due to conduction.

Table 7: Properties of Polyurethane Foam

Parameter	units	value
thermal conductivity	$W/(m \cdot K) \times 10^{-3}$	30.0
specific heat capacity	$J/(kg \cdot K) \times 10^3$	1.49
density	$kg/m^3$	96.1
thermal diffusivity	$m^2/s \times 10^{-9}$	210.
$k \cdot \rho \cdot c$	$(W^2 \cdot s)/(m^4 \cdot K^2)$	430.

Table 8: Turbulence Statistical Properties from Hotwire Tests

Case	variance	skewness	kurtosis	$\bar{u}$	$Tu$	$tke$	$\Lambda_l$
No Wedge 8 <i>cm</i>	0.4238	0.2976	3.3298	2.3130	0.2814	0.2119	0.0682
No Wedge 9.25 <i>cm</i>	0.3604	0.2318	3.0148	2.2811	0.2632	0.1802	0.0557
No Wedge 10.5 <i>cm</i>	0.3503	0.4509	3.4373	2.3162	0.2555	0.1751	0.0509
Wedge 8 <i>cm</i>	0.0513	0.0764	4.0654	2.1638	0.1047	0.0257	0.0361
Wedge 9.25 <i>cm</i>	0.0566	0.1133	3.3885	2.1384	0.1112	0.0283	0.0381
Wedge 10.5 <i>cm</i>	0.0550	0.1955	3.7985	2.1061	0.1113	0.0275	0.0310

### A.2 Hotwire Anemometry Measurements of Turbulent Intensity

Data from a 1-D hotwire anemometry probe was used to calculate turbulent statistics for the experiments. The probe was placed 3 *cm* upstream of the hole. Three data points were taken in the free-stream flow at 8, 9.25, and 10.5 *cm* away from the coupon surface at the hole location at a rate of 10 *kHz*. The data for the point 9.25 *cm* from to the wall for the zero pressure gradient case and for the pressure gradient case are shown in Figs. 50 and 51. Plots of power spectral density are shown in Figs. 52-57.

An autocorrelation was performed on the hotwire data, and the integral time scales were determined by integrating the autocorrelation up to the first crossing of the time axis. The length scales were then obtained by multiplying the bulk velocity by the time scale. Some other turbulence statistics are listed in Tab. 8.

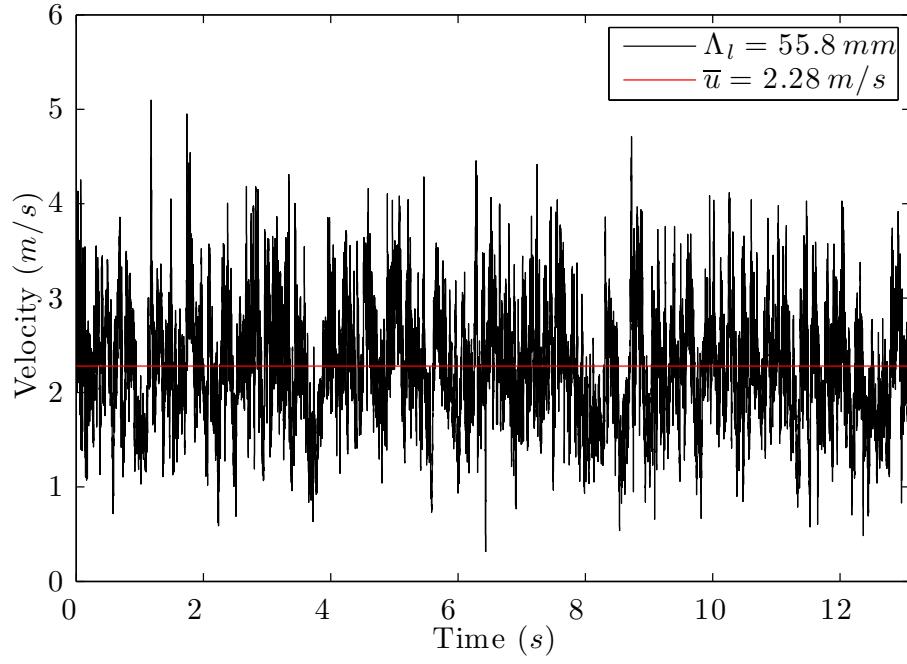


Figure 50: Hotwire data for the zero pressure gradient configuration, 9.25 *cm* from the wall, 3 *cm* upstream of the hole.

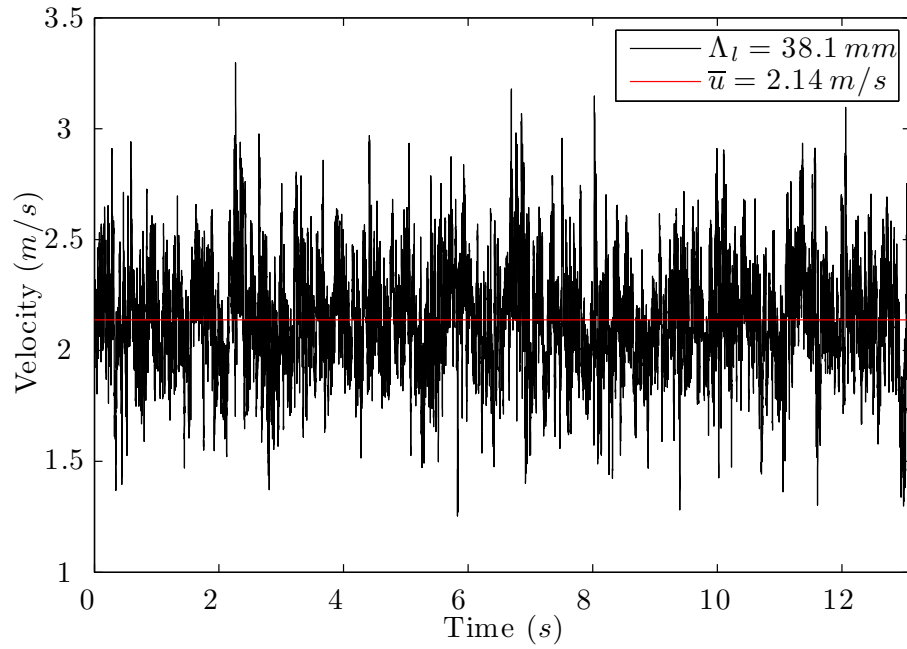


Figure 51: Hotwire data for the favorable pressure gradient configuration, 9.25 *cm* from the wall, 3 *cm* upstream of the hole.

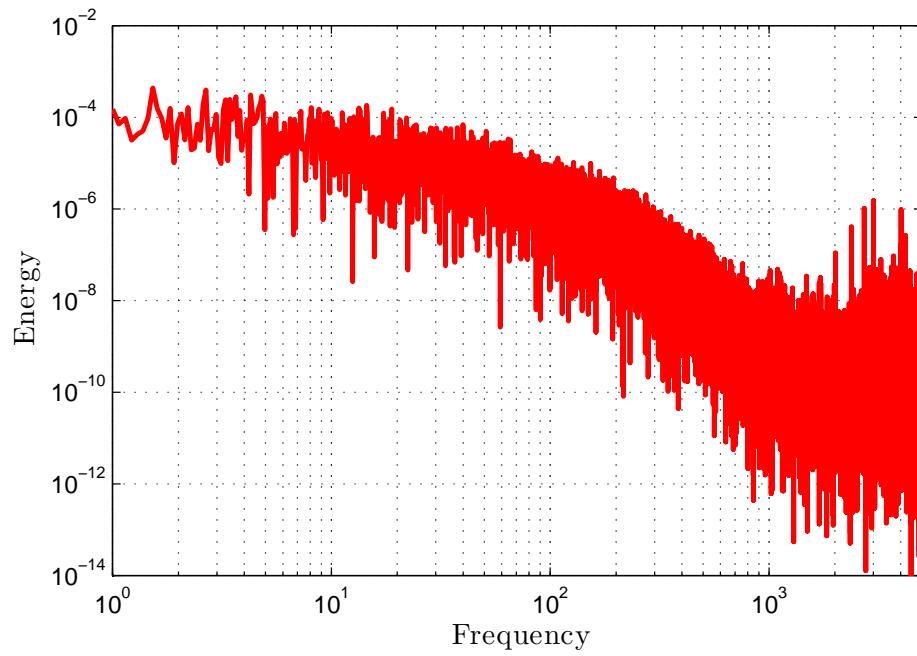


Figure 52: Power spectral density for the favorable pressure gradient configuration, 8 *cm* from the wall, 3 *cm* upstream of the hole.

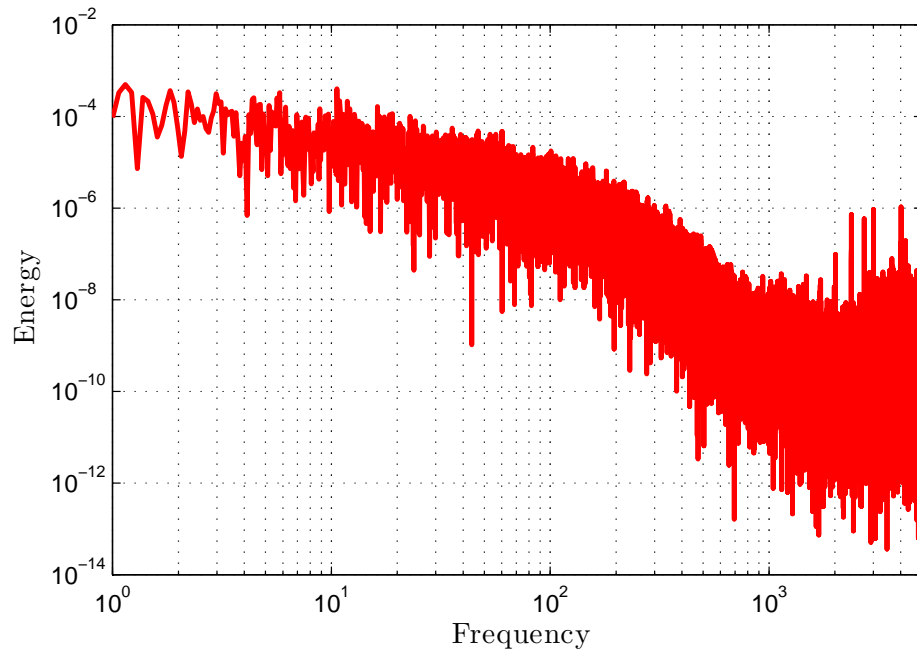


Figure 53: Power spectral density for the favorable pressure gradient configuration, 9.25 *cm* from the wall, 3 *cm* upstream of the hole.

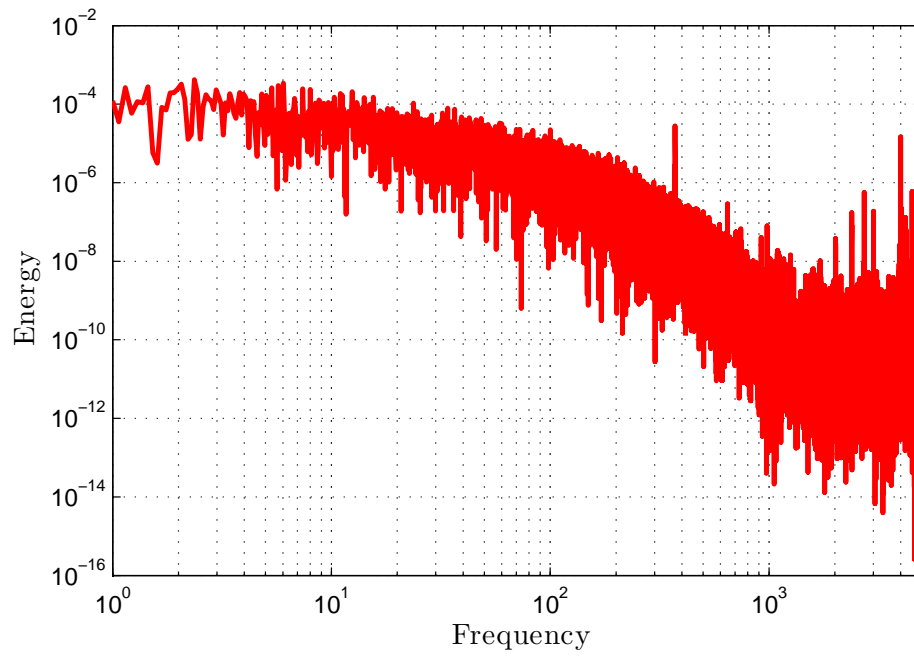


Figure 54: Power spectral density for the favorable pressure gradient configuration, 10.5 *cm* from the wall, 3 *cm* upstream of the hole.

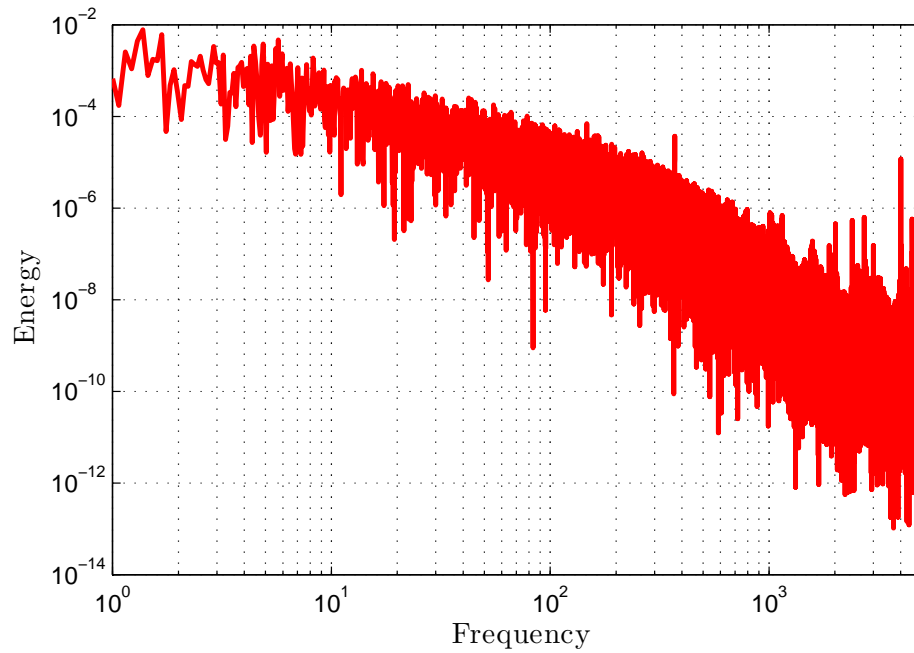


Figure 55: Power spectral density for the zero pressure gradient configuration, 8 *cm* from the wall, 3 *cm* upstream of the hole.

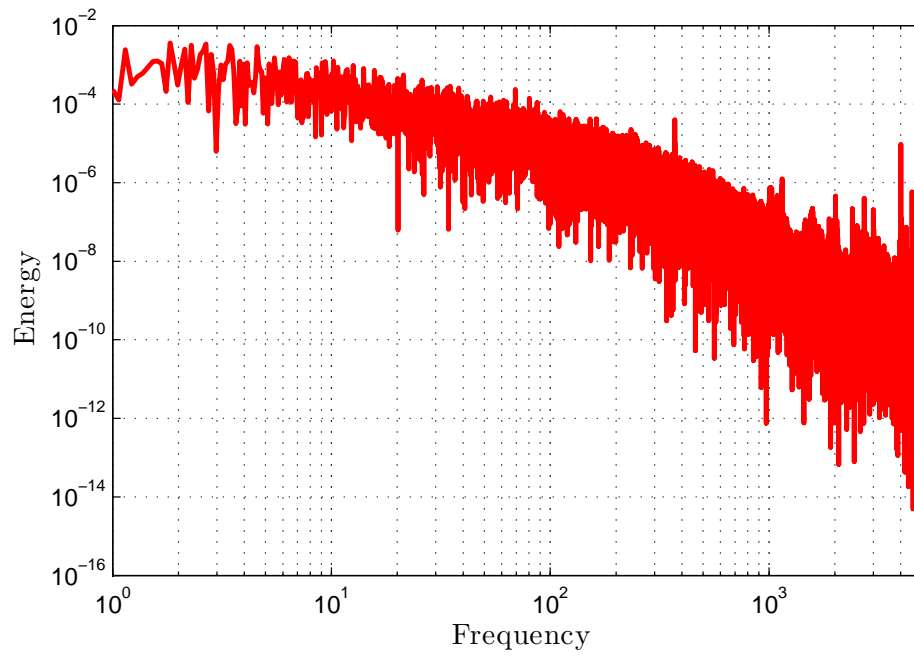


Figure 56: Power spectral density for the zero pressure gradient configuration, 9.25 *cm* from the wall, 3 *cm* upstream of the hole.

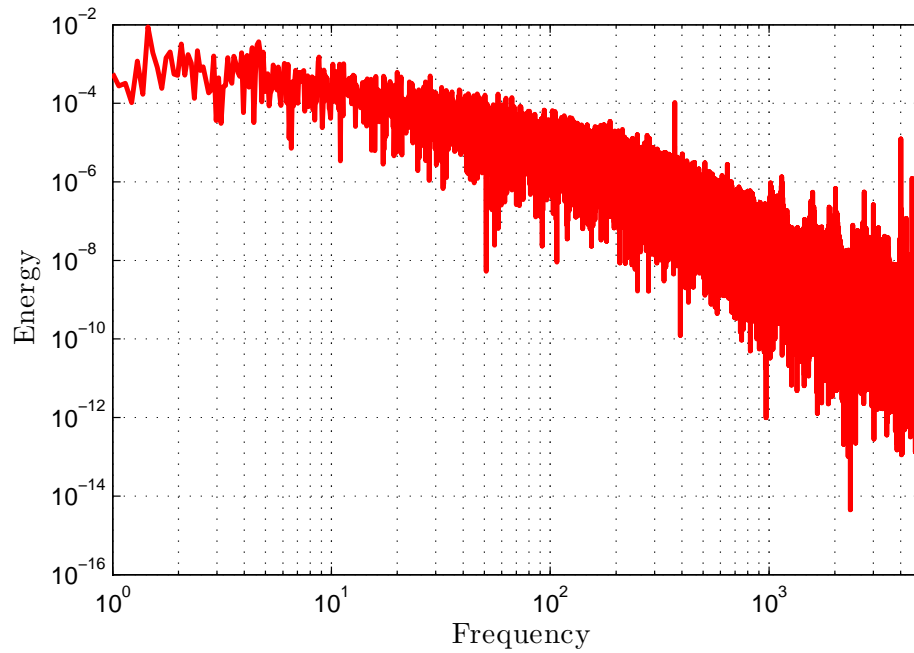


Figure 57: Power spectral density for the zero pressure gradient configuration, 10.5 *cm* from the wall, 3 *cm* upstream of the hole.

### A.3 Infrared Thermography System

The infrared (IR) camera was used to collect surface temperatures of a coupon over a period of 10 seconds. The maximum acquisition rate for the device was 30 images per second. The camera contains subroutines for calibration based on atmospheric temperature, humidity, and surface emissivity. Rather than use these curve fits, I chose to calibrate the response of the camera to thermocouples at a known temperature.

First, four K-type thermocouples were calibrated using boiling water and an ice bath. Each thermocouple was made from the same batch of wire, so bias errors were expected to be low. In the ice bath, each thermocouple measured  $273.2\text{ K}$ , and in the boiling water they each measured  $371.3\text{ K}$ . The ambient pressure was recorded as  $946.3\text{ kPa}$ . The well known Antoine equation [82] for the boiling point of water

$$T_b = \frac{1730.63}{8.07131 - \log_{10} P} - 233.426 \quad (115)$$

where  $T_b$  is the boiling temperature in  $^{\circ}\text{C}$  and  $P$  is the atmospheric absolute pressure in *tor*, was used to calculate the boiling temperature at the current atmospheric pressure. It was determined the thermocouples were reading the correct boiling temperature within the accuracy of the output device ( $\pm 0.05\text{ K}$ ). No variation was discerned between the thermocouples at either temperature. The thermocouples were then placed on a coupon which was not used for actual testing and heated using the main flow from  $293\text{ K}$  to  $332\text{ K}$  to encompass the range of surface temperatures expected during any test. Figure 58 contains the curve used to calibrate the camera. 98 data points were used to generate this curve, where  $R^2 = 0.9998$  and  $sse = 3.8762\text{ K}^2$ . The resulting curve is

$$T_{cal} = 0.998 T_{IR} + 0.963 \quad (116)$$

where  $T_{IR}$  is the raw temperature from the IR camera and  $T_{cal}$  is the corrected, calibrated temperature.



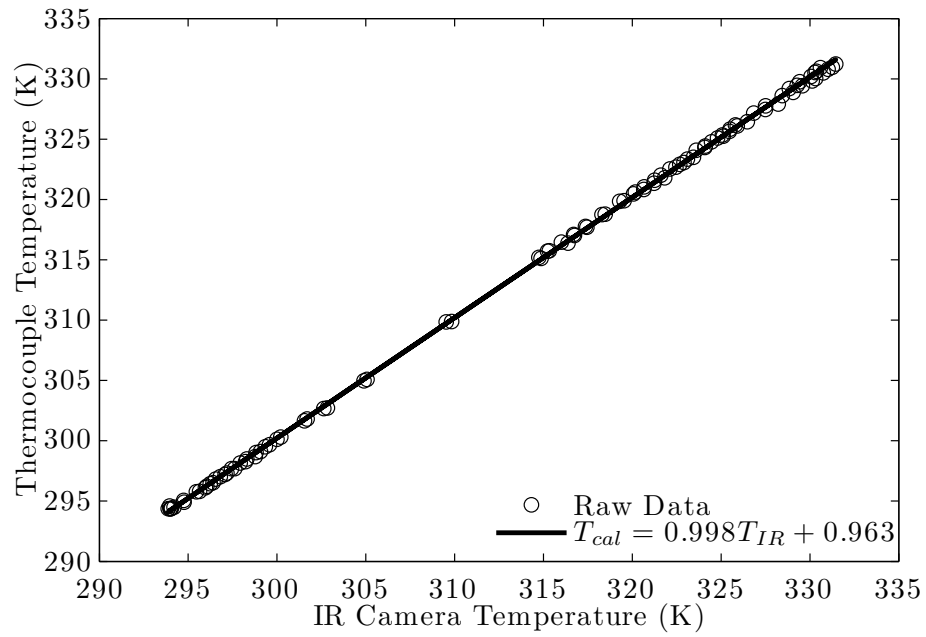


Figure 58: Calibration curve for IR data. Every pixel's temperature is operated on by the function in the figure to obtain the actual temperature as read by the thermocouples. This reduced the error in the IR camera's measurement of temperature to nearly that of the thermocouples.

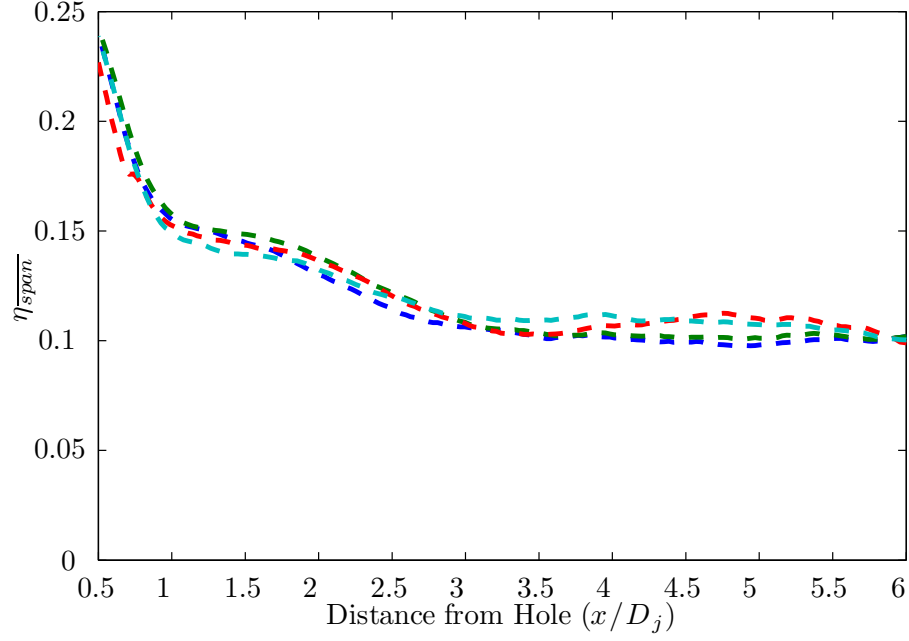


Figure 59: Results of repeatability tests. Four tests were run to determine how repeatable the transient technique is for this experimental setup.

#### A.4 Repeatability of Transient Technique

Another way to measure the error in a process is to test one data point several times and thereby obtain a value for repeatability of the population. I chose to repeat the high pressure gradient case with  $D_\infty/D_j = 16$  at a blowing ratio of  $F = 1.0$  and ran these repeatability tests in the same method as the other data points. Span-wise averaged adiabatic effectiveness is plotted for these tests in Fig. 59. The standard error for these tests was 0.74%.

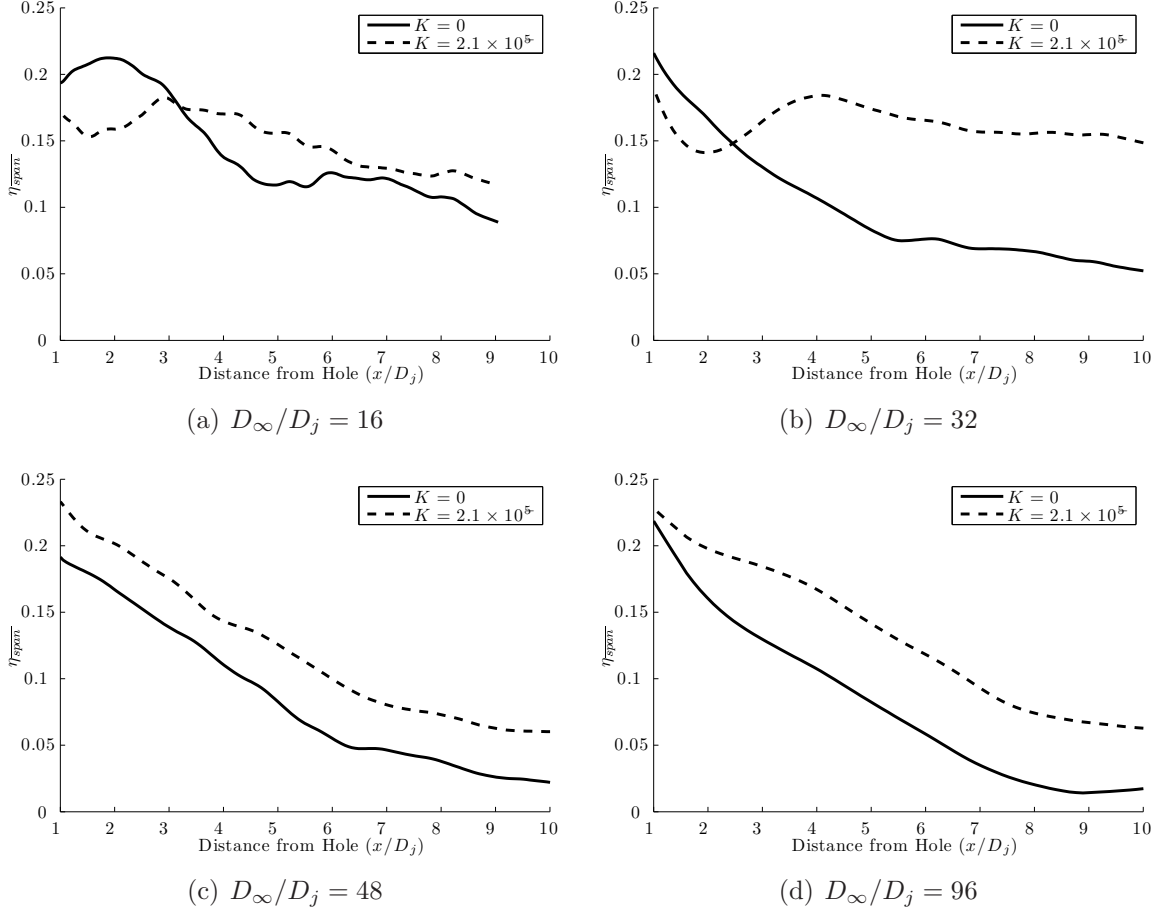


Figure 60: Effect of pressure gradient on adiabatic effectiveness,  $F = 0.5$ ,  $\alpha = 90^\circ$

### A.5 Figures of pressure gradient Comparisons

Figures 60-64 show the effects of inducing a stream-wise pressure gradient on span-wise averaged adiabatic effectiveness. These figures are referenced in Sec. 5.2 (p. 96).

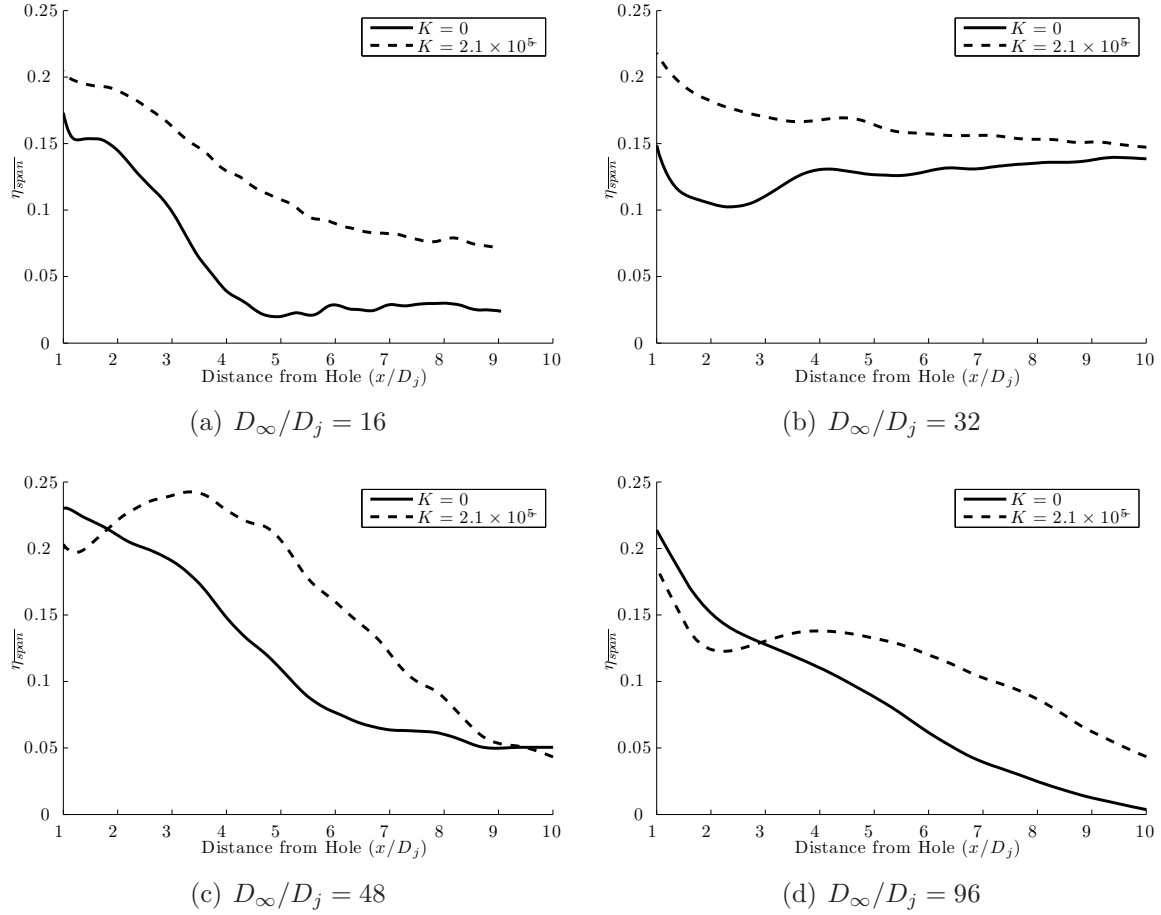


Figure 61: Effect of pressure gradient on adiabatic effectiveness,  $F = 0.7$ ,  $\alpha = 90^\circ$

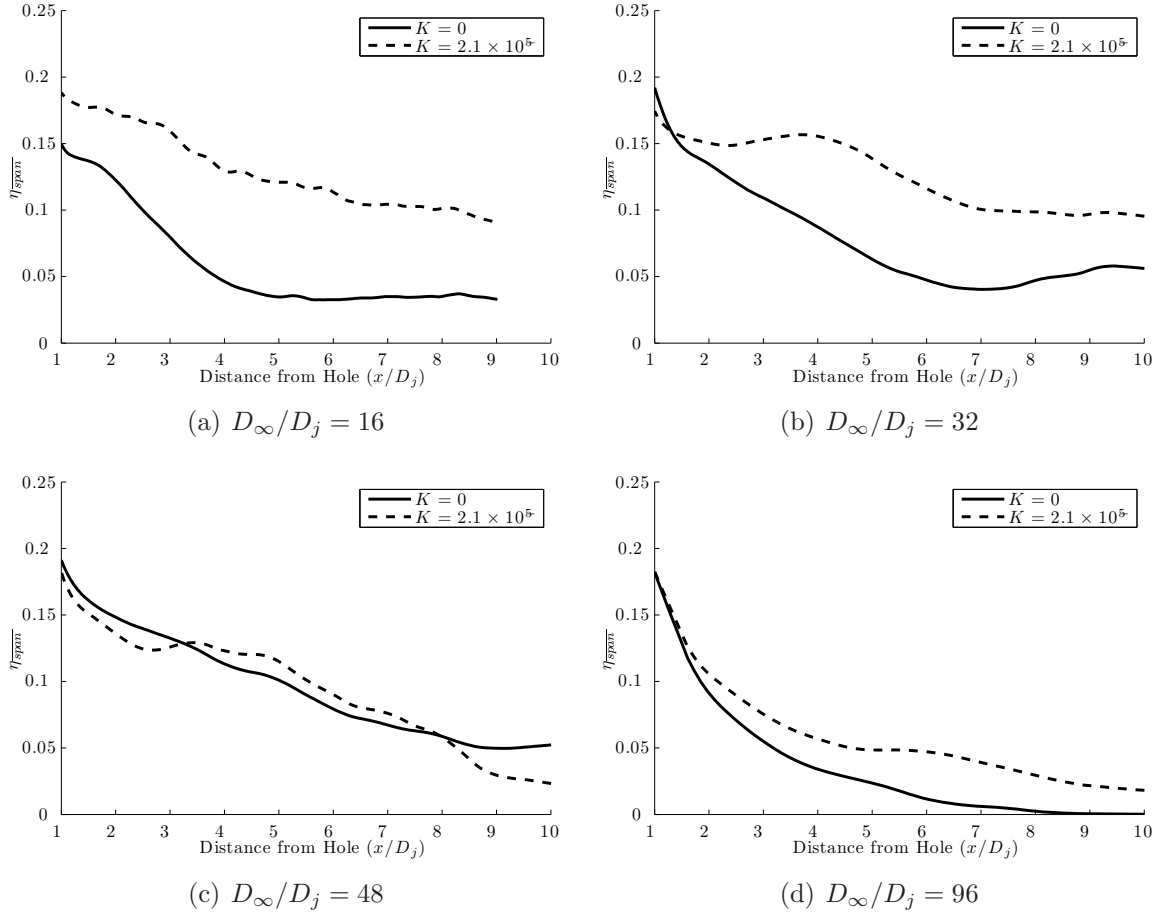
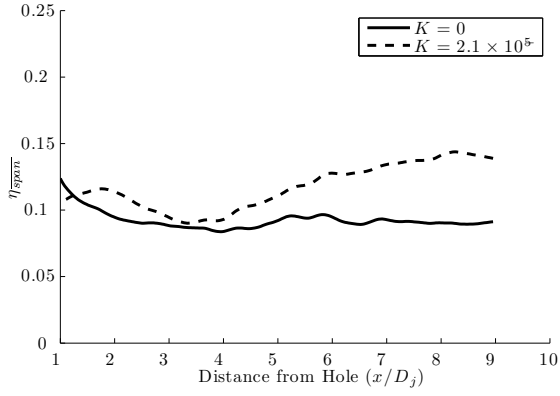
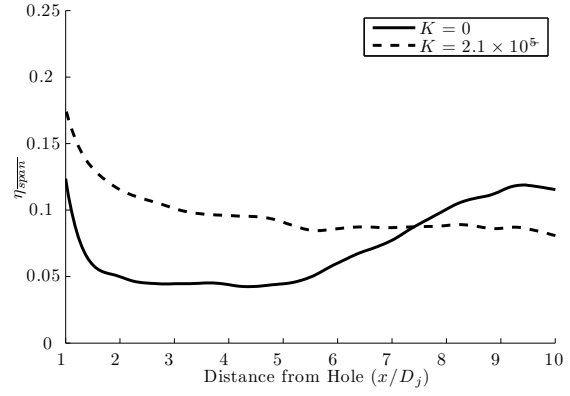


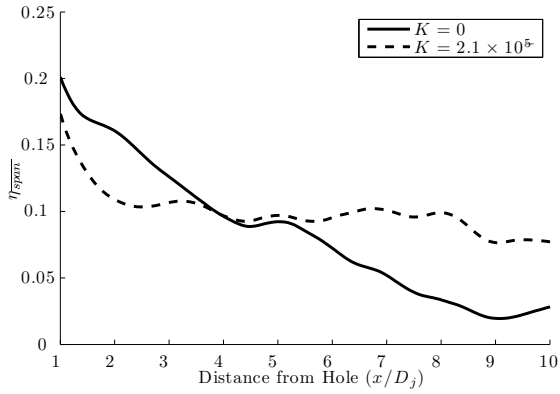
Figure 62: Effect of pressure gradient on adiabatic effectiveness,  $F = 1.0$ ,  $\alpha = 90^\circ$



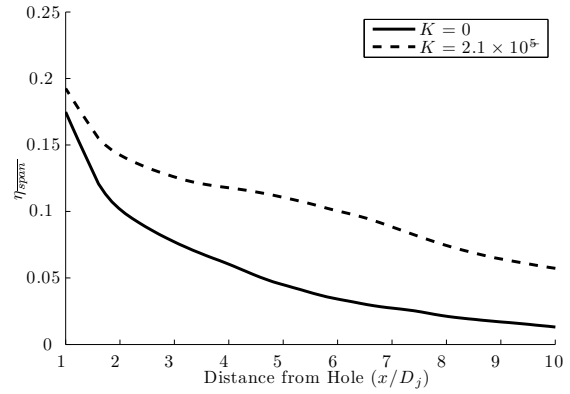
(a)  $D_\infty/D_j = 16$



(b)  $D_\infty/D_j = 32$

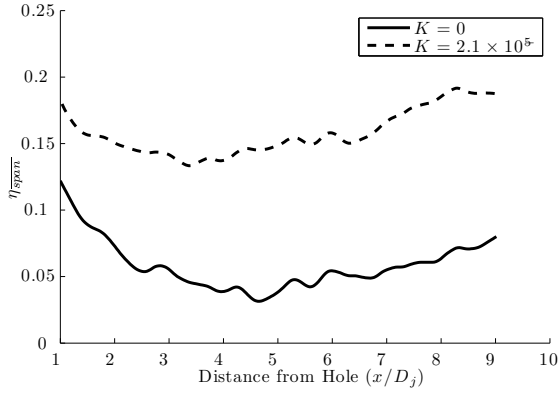


(c)  $D_\infty/D_j = 48$

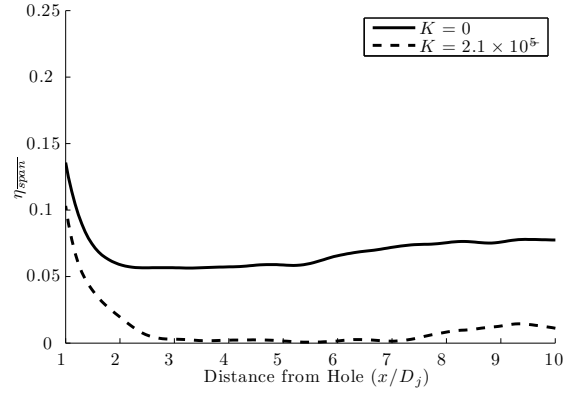


(d)  $D_\infty/D_j = 96$

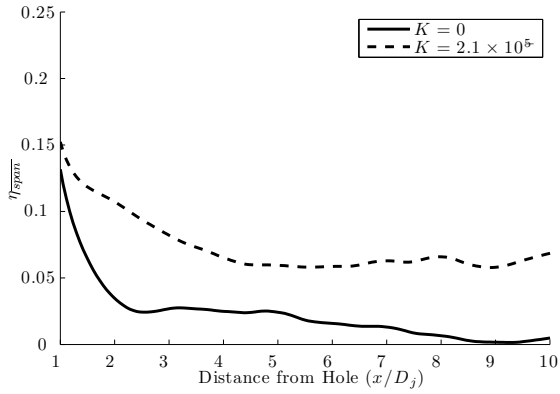
Figure 63: Effect of pressure gradient on adiabatic effectiveness,  $F = 1.25$ ,  $\alpha = 90^\circ$



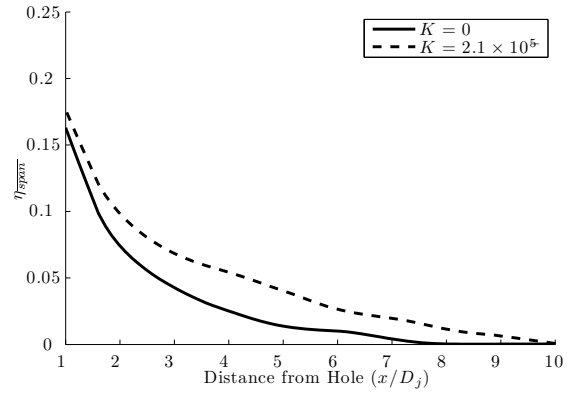
(a)  $D_\infty/D_j = 16$



(b)  $D_\infty/D_j = 32$



(c)  $D_\infty/D_j = 48$



(d)  $D_\infty/D_j = 96$

Figure 64: Effect of pressure gradient on adiabatic effectiveness,  $F = 1.50$ ,  $\alpha = 90^\circ$

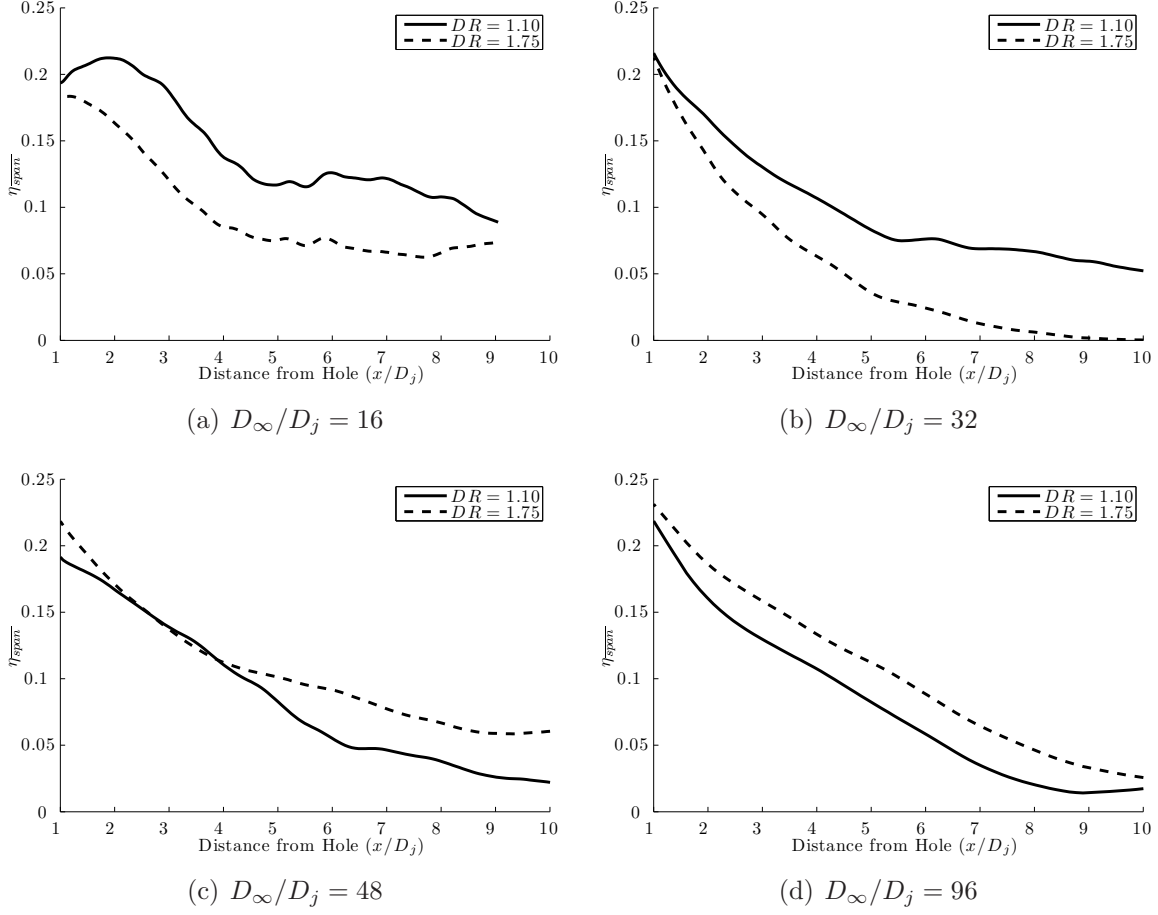


Figure 65: Effect of high density ratio on adiabatic effectiveness,  $F = 0.5$ ,  $\alpha = 90^\circ$

### A.6 Figures of Density Ratio Comparisons

The following Figs. (65(a)-69(d)) show the effects of a higher density ratio on span-wise averaged adiabatic effectiveness. These figures are referenced in Sec. 5.3 (p. 98).



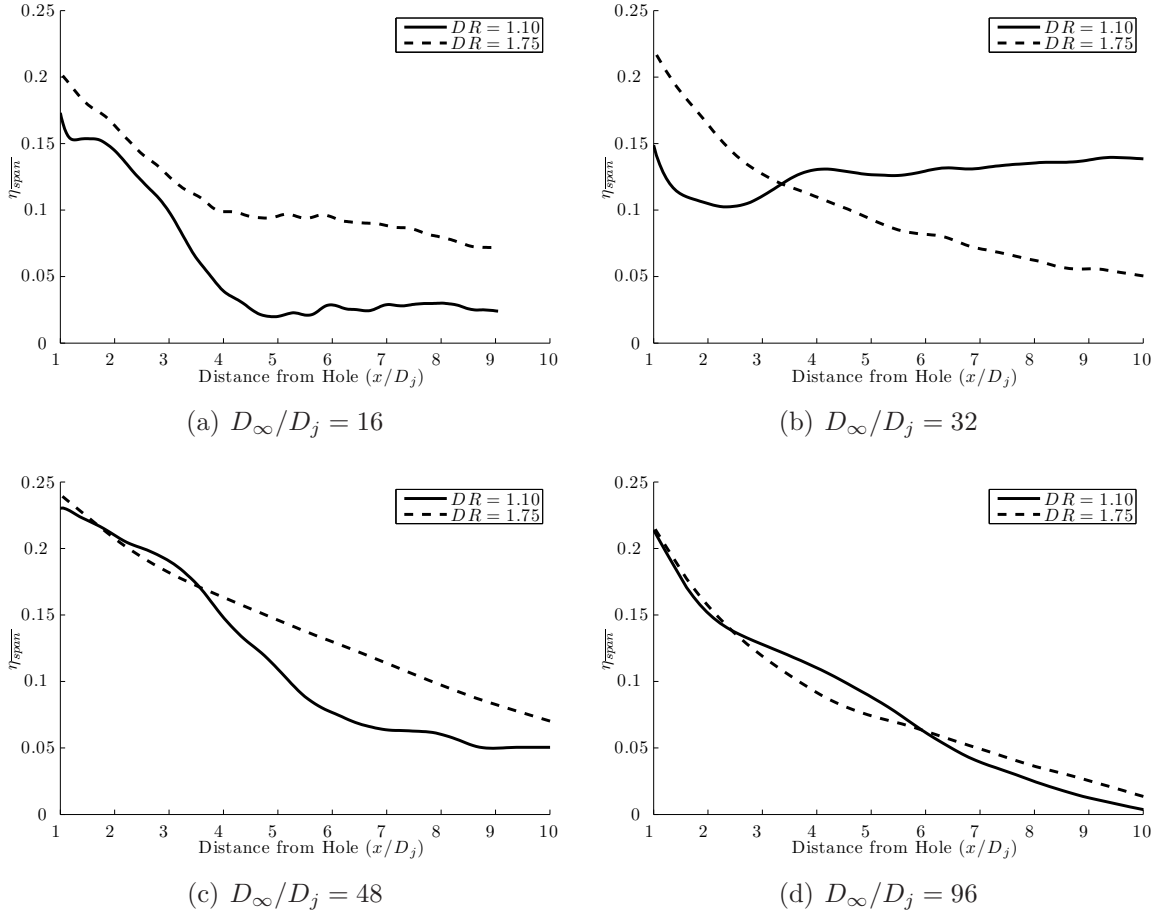


Figure 66: Effect of high density ratio on adiabatic effectiveness,  $F = 0.7$ ,  $\alpha = 90^\circ$

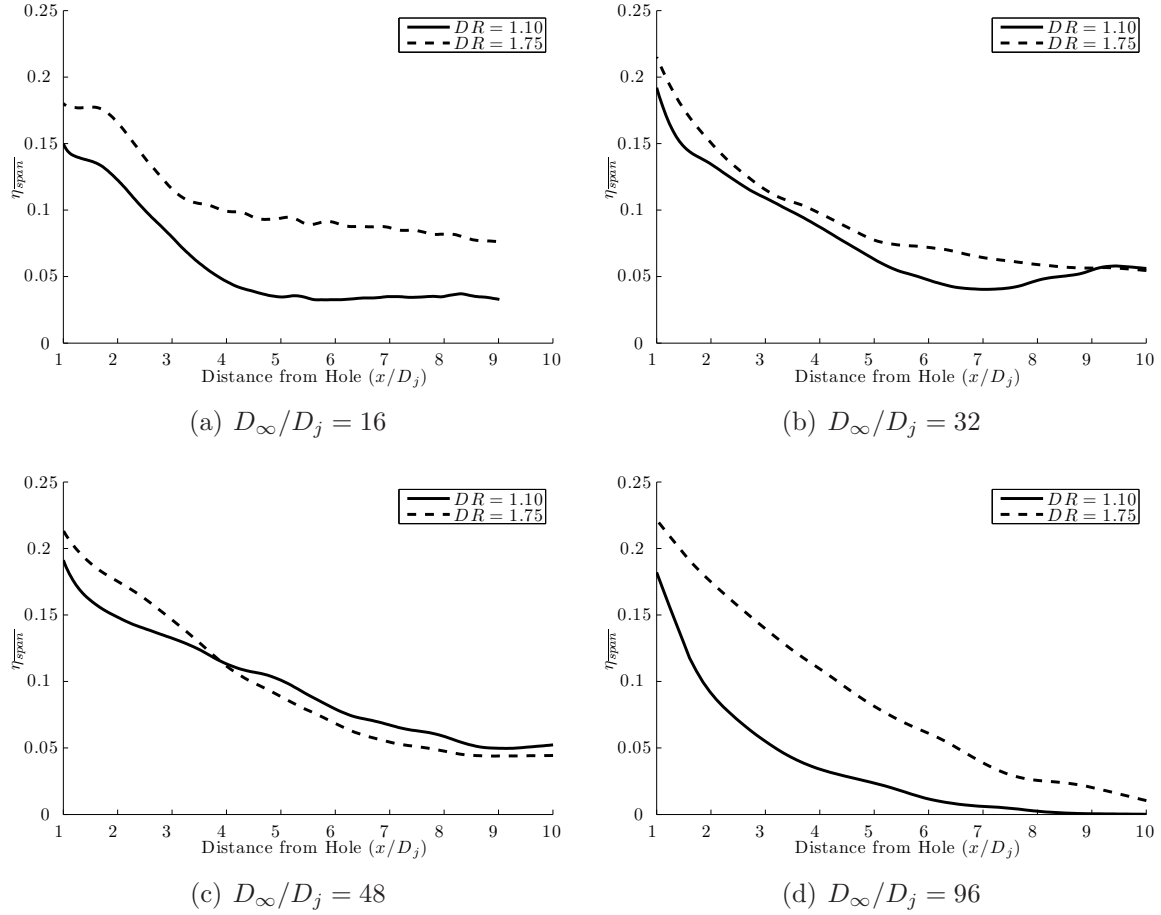


Figure 67: Effect of high density ratio on adiabatic effectiveness,  $F = 1.0$ ,  $\alpha = 90^\circ$

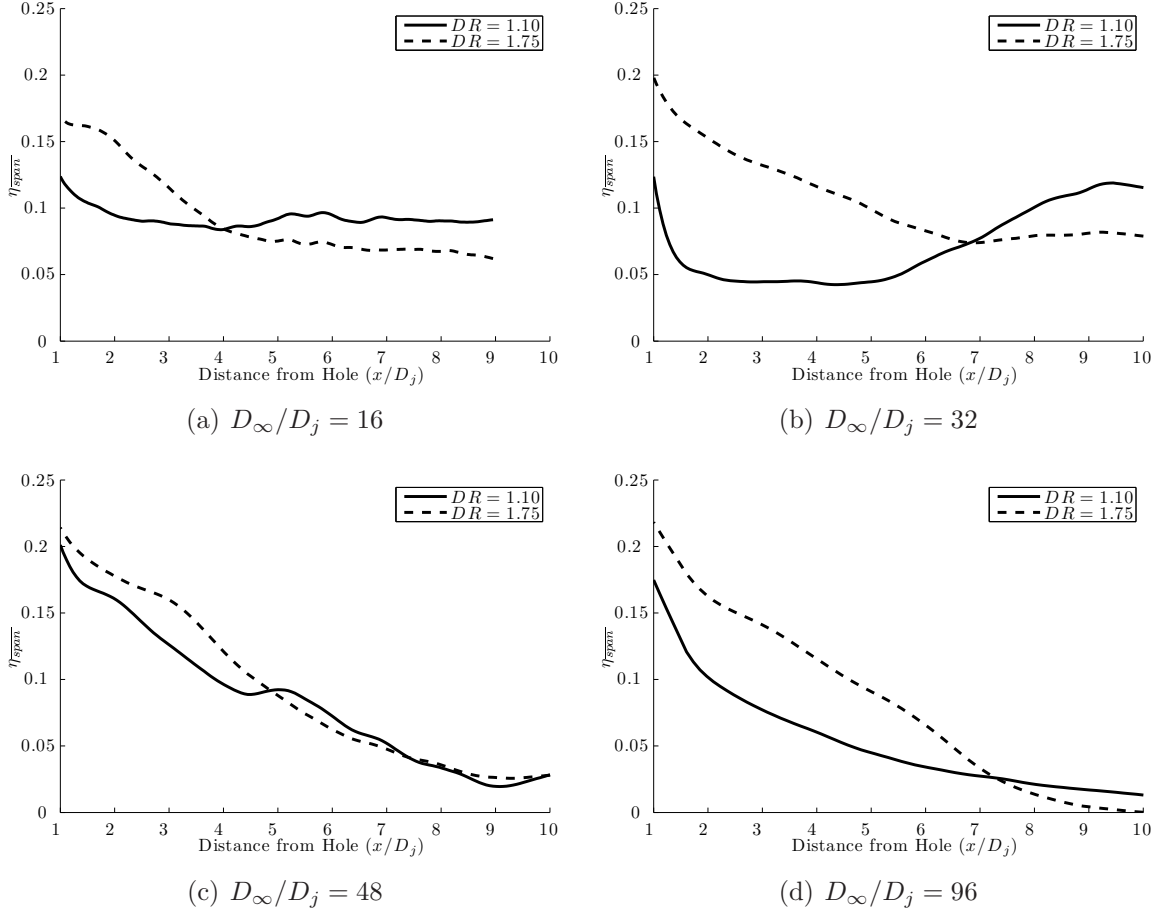
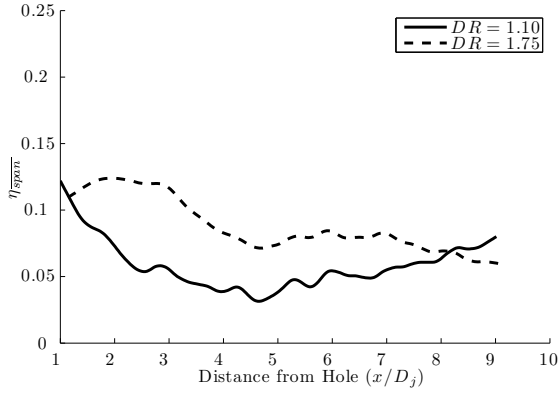
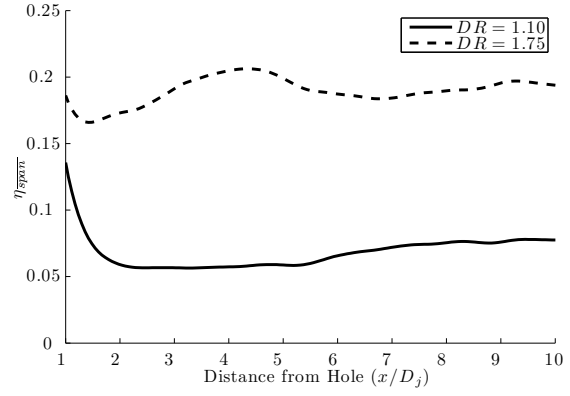


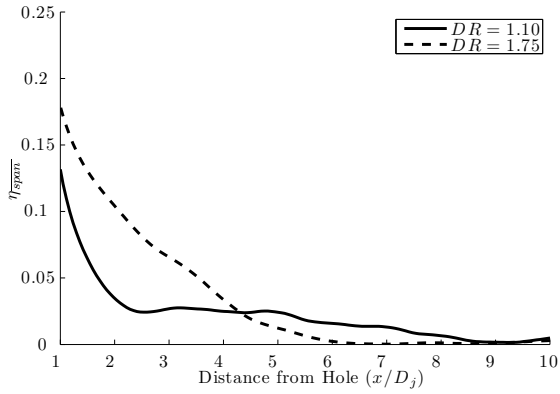
Figure 68: Effect of high density ratio on adiabatic effectiveness,  $F = 1.25$ ,  $\alpha = 90^\circ$



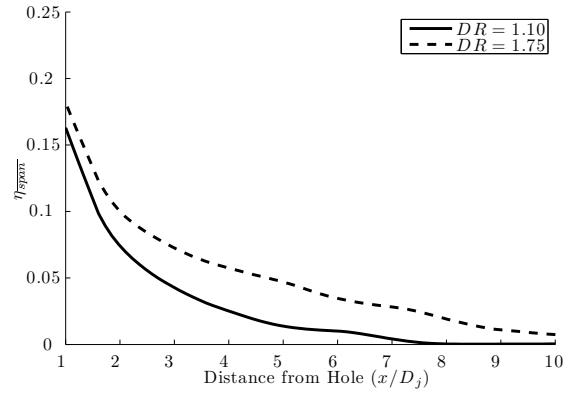
(a)  $D_\infty/D_j = 16$



(b)  $D_\infty/D_j = 32$



(c)  $D_\infty/D_j = 48$



(d)  $D_\infty/D_j = 96$

Figure 69: Effect of high density ratio on adiabatic effectiveness,  $F = 1.50$ ,  $\alpha = 90^\circ$

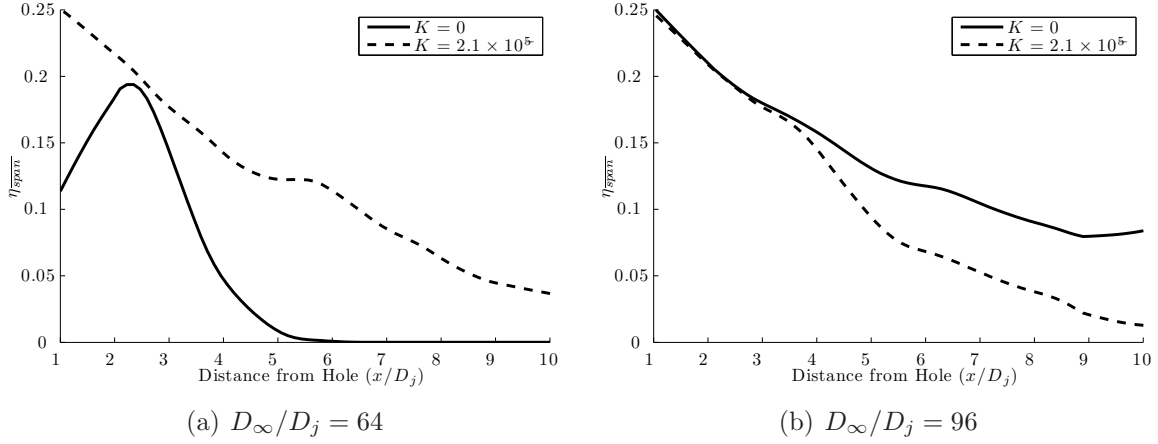


Figure 70: Effect of pressure gradient on adiabatic effectiveness,  $F = 0.5$ ,  $\alpha = 0^\circ$

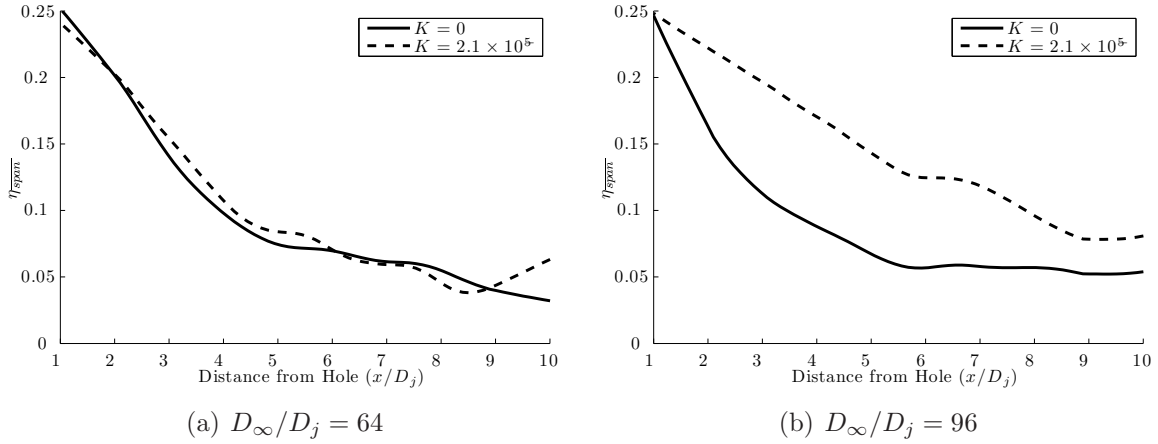


Figure 71: Effect of pressure gradient on adiabatic effectiveness,  $F = 0.7$ ,  $\alpha = 0^\circ$

### A.7 Figures of Zero Compound Injection Angle Comparisons

Figures 70-74 show the effects of inducing a stream-wise pressure gradient on span-wise averaged adiabatic effectiveness with zero compound injection angle and a  $30^\circ$  normal injection angle. Figures 75-79, starting on p. 149, show the effects of a high density ratio on span-wise averaged adiabatic effectiveness for the same geometry. These figures are referenced in Sec. 5.5 (p. 105).

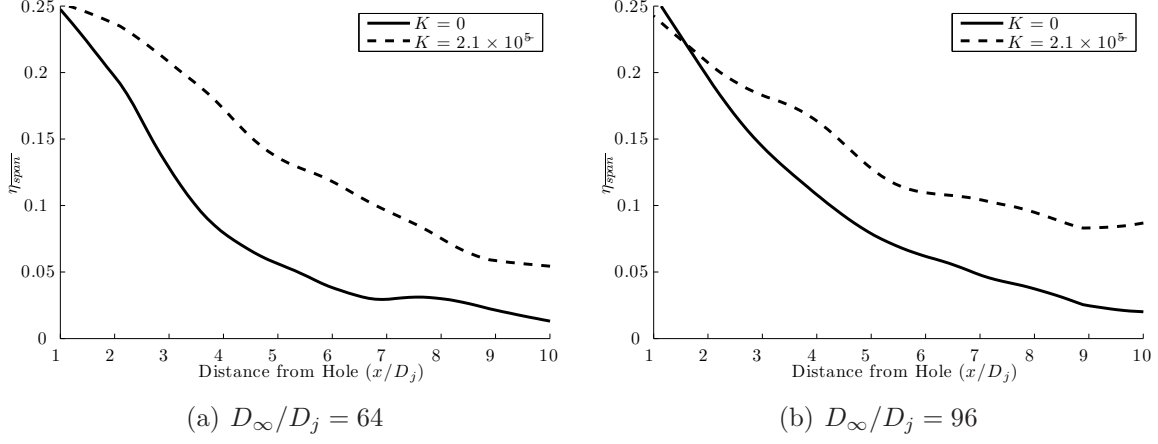


Figure 72: Effect of pressure gradient on adiabatic effectiveness,  $F = 1.0$ ,  $\alpha = 0^\circ$

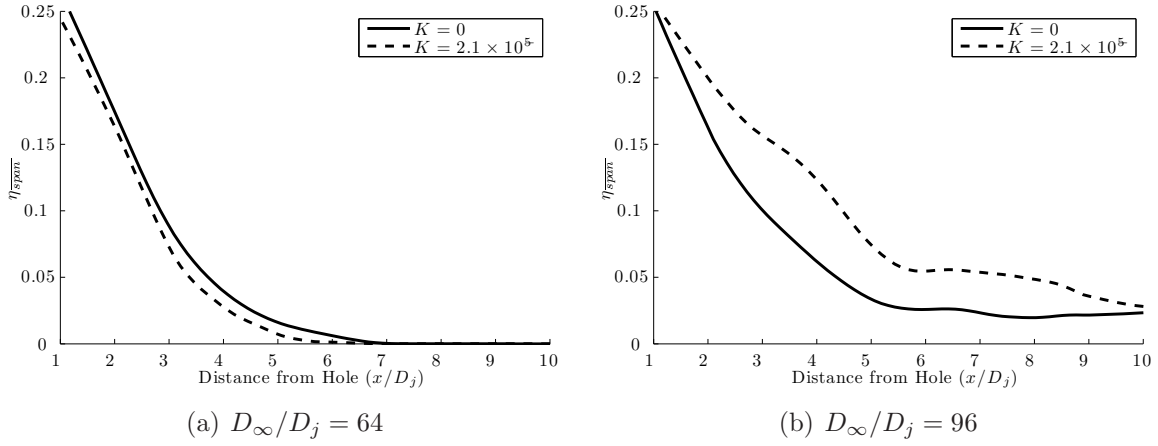


Figure 73: Effect of pressure gradient on adiabatic effectiveness,  $F = 1.25$ ,  $\alpha = 0^\circ$

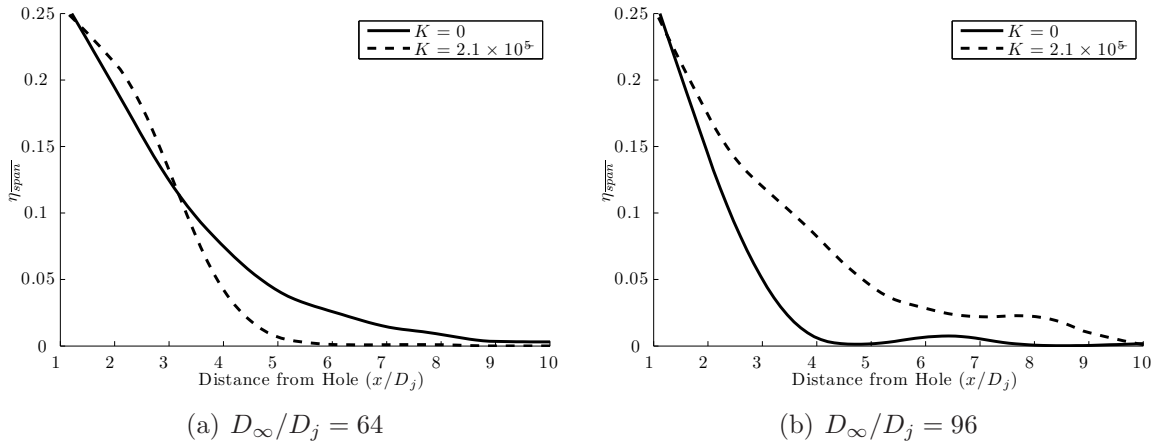


Figure 74: Effect of pressure gradient on adiabatic effectiveness,  $F = 1.50$ ,  $\alpha = 0^\circ$

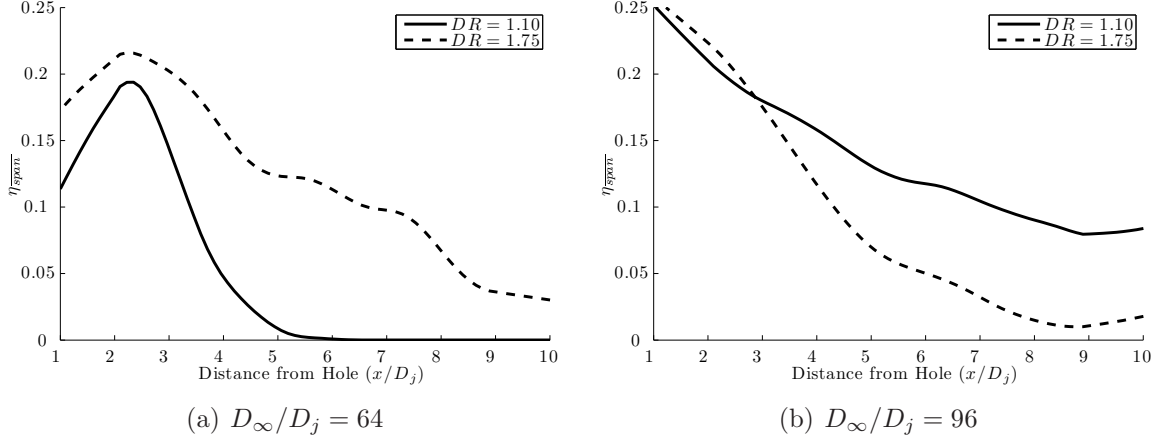


Figure 75: Effect of high density ratio on adiabatic effectiveness,  $F = 0.5$ ,  $\alpha = 0^\circ$

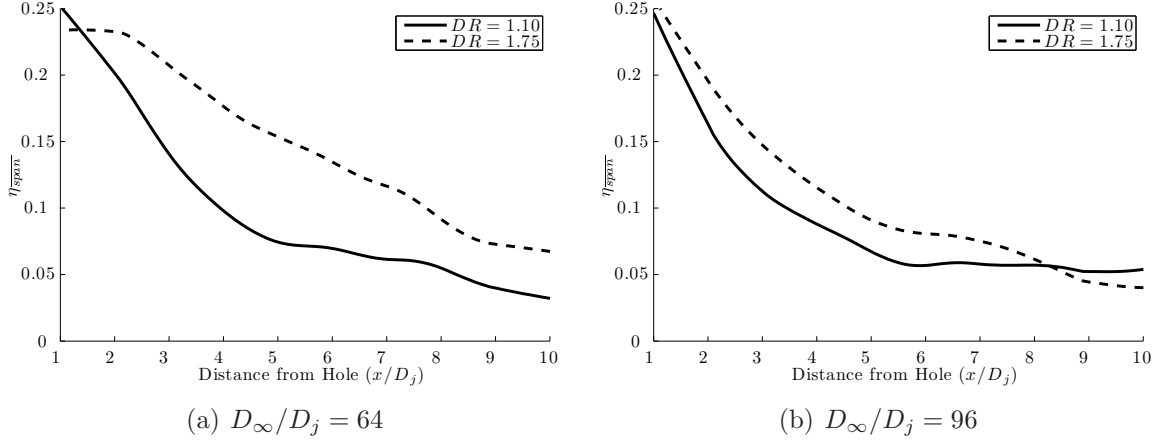


Figure 76: Effect of high density ratio on adiabatic effectiveness,  $F = 0.7$ ,  $\alpha = 0^\circ$

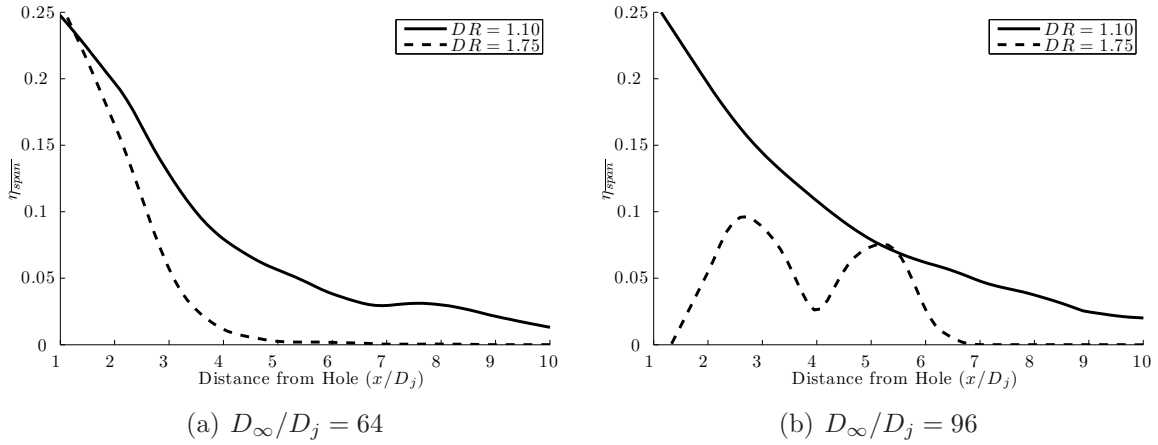


Figure 77: Effect of high density ratio on adiabatic effectiveness,  $F = 1.0$ ,  $\alpha = 0^\circ$

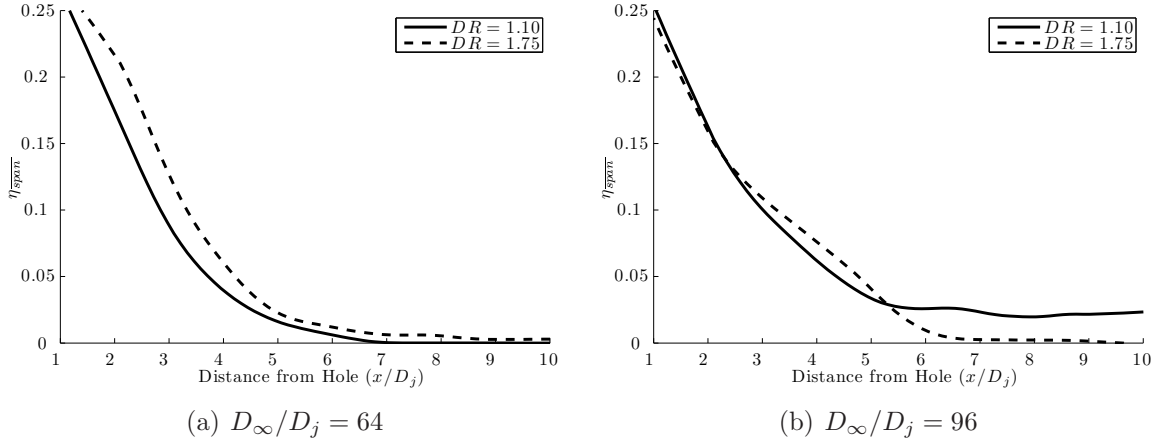


Figure 78: Effect of high density ratio on adiabatic effectiveness,  $F = 1.25$ ,  $\alpha = 0^\circ$

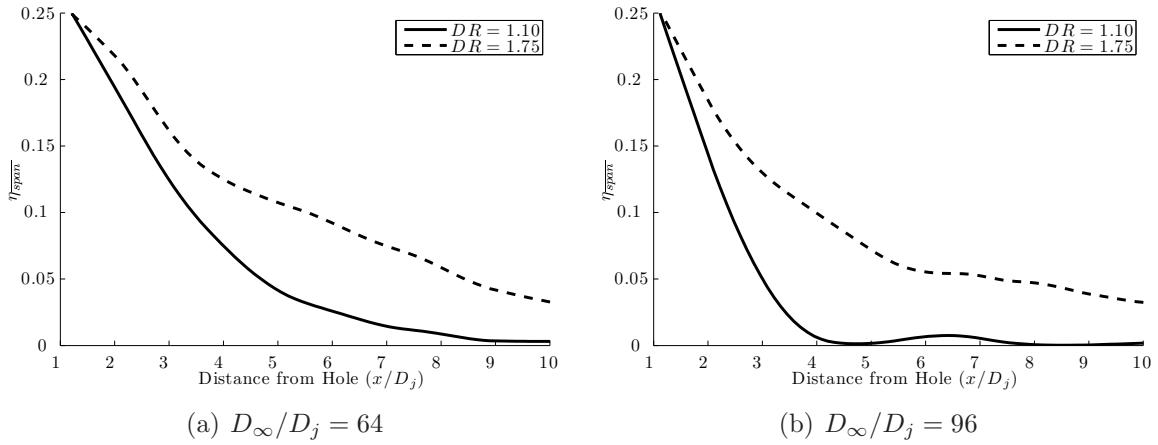


Figure 79: Effect of high density ratio on adiabatic effectiveness,  $F = 1.50$ ,  $\alpha = 0^\circ$



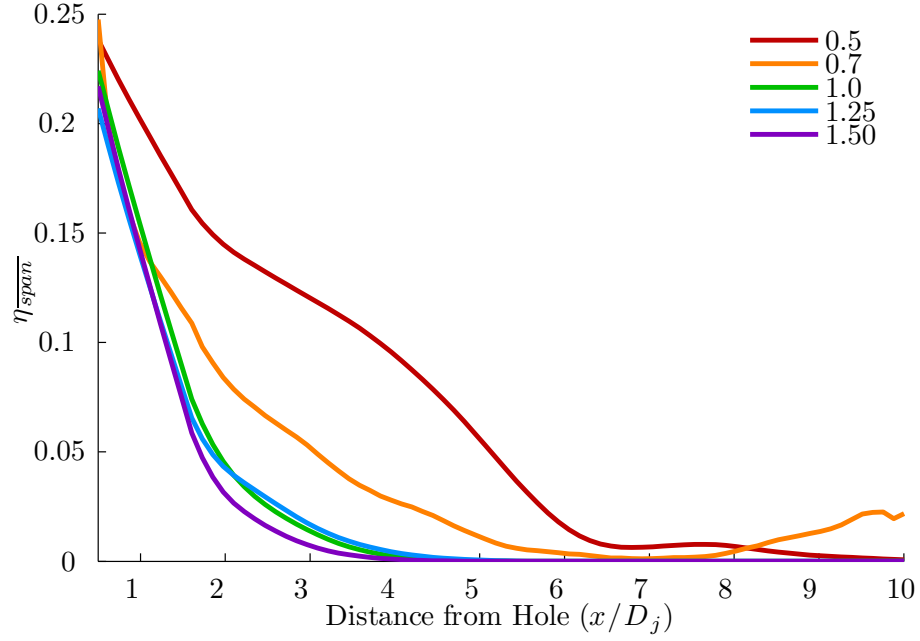


Figure 80: Adiabatic effectiveness for  $D_\infty/D_j = 64$

#### A.8 Figures of $D_\infty/D_j = 64$

I noted in Sec. 5.1 (p. 93) the data for the 90° compound injection case where  $D_\infty/D_j = 64$  appears out of family for all the tested cases. This data is included here for completeness.

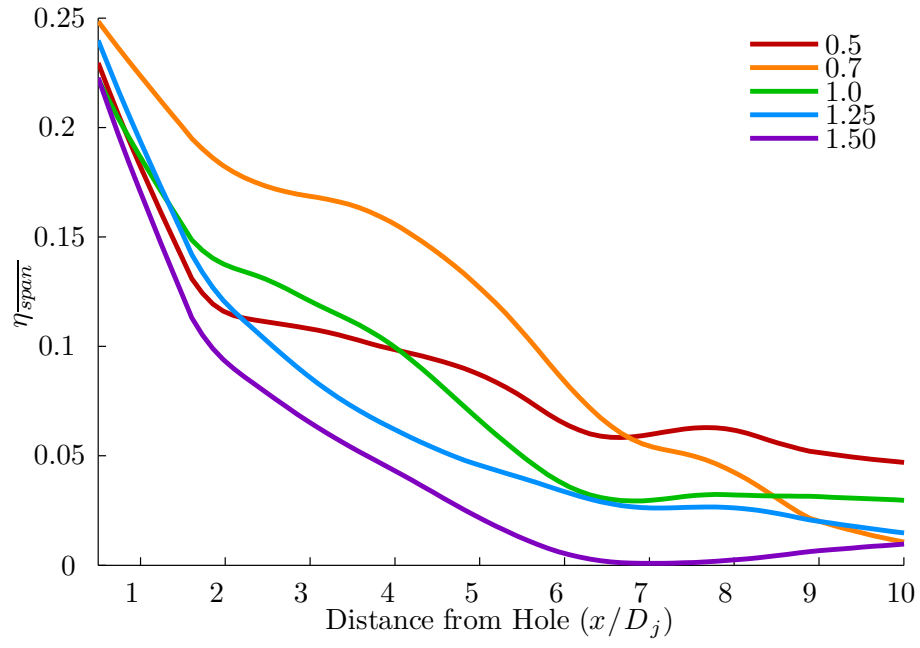


Figure 81: Adiabatic effectiveness with strong favorable pressure gradient for  $D_\infty/D_j = 64$

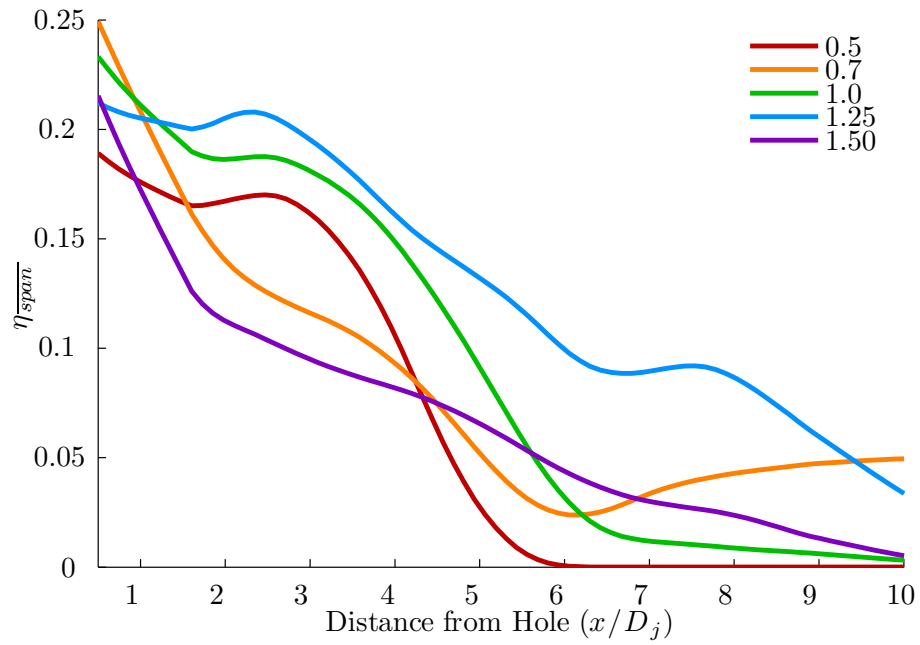


Figure 82: Adiabatic effectiveness with high density ratio for  $D_\infty/D_j = 64$

## Bibliography

1. P. G. Hill and C. R. Peterson. *Mechanics and Thermodynamics of Propulsion*. Addison-Wesley, Reading, MA, 1992.
2. J. Meinert, J. Huhn, E. Serbest, and O. J. Haidn. Investigations on the effect of foreign gas transpiration on a turbulent boundary layer. In *36th AIAA/ASME/SAE/ASEE Joint Propulsion Conference & Exhibit*, number AIAA 2000-3386, Huntsville, AL, July 2000.
3. W. Zinner, D. Haeseler, C. Mading, V. Rubinsky, V. Gorokhov, S. Hrisanfov, and G. Nikulin. Development of advanced technologies for future cryogenic thrust chamber applications. *AIAA*, 97-3312, 1997.
4. W. M. Burkhardt, S. E. Tobin, and H. H. Mueggenburg. Formed platelet liner concept for regeneratively cooled chambers. In *AIAA/SAE/ASME/ASEE 26th Joint Propulsion Conference*, number AIAA 90-2117, 1990.
5. D. G. Bogard and K. A. Thole. Gas turbine film cooling. *J. Propulsion and Power*, 22(2):249–270, 2006. AIAA.
6. W. D. Rannie. A simplified theory of porous wall cooling. Technical report, Jet Propulsion Laboratory Calif. Inst. of Tech., 1947.
7. W.M. Kays, M.E. Crawford, and B. Weigand. *Convective Heat and Mass Transfer*. McGraw-Hill, New York, 2005.
8. D. Greuel, A. Herbertz, O. J. Haidn, M. Ortelt, and H. Hald. Transpiration cooling applied to C/C liners of cryogenic liquid rocket engines. In *40th AIAA/ASME/SAE/ASEE Joint Propulsion Conference and Exhibit*, number AIAA 2004 - 3682, Ft Lauderdale, FL, July 2004.
9. L. O. F. Jeromin. The status of research in turbulent boundary layers with fluid injection. Technical report, Engineering Department, Univ. Cambridge, 1970.
10. D. R. Bartz. *Turbulent Boundary-Layer Heat Transfer from Rapidly Accelerating Flow of Rocket Combustion Gases and of Heated Air*, pages 1–108. Advances in Heat Transfer, Vol 2. Academic Press, New York, 1965.
11. H. Mueggenburg and G. Repas. A highly durable injector faceplate design concept for  $O_2/H_2$  propellants. In *AIAA, ASME, SAE, and ASEE, Joint Propulsion Conference and Exhibit, 26th*, number AIAA-1990-2181, Orlando, FL, June 1990.
12. W. S. Weisinger. An experimental determination of temperature profiles in a fluid flowing over a transpiration cooled flat plate. Master’s thesis, Air Force Inst. Tech., 1964.
13. J. A. Landis. Numerical study of a transpiration cooled rocket nozzle. Master’s thesis, Air Force Inst. Tech., 1995.

14. J. Lenertz. Effects of blowing ratio on heat transfer to the throat region of a porous-walled nozzle. Master's thesis, Air Force Inst. Tech., 1994.
15. F. Chen, W. J. Bowman, and R. Bowersox. Effect of transpiration cooling on nozzle heat transfer. *J. Spacecraft*, 33(3):453–455, 1995.
16. F. Chen. Effects of blowing ratios on heat transfer to the throat region of a porous-walled nozzle. Master's thesis, Air Force Inst. Tech., 1995.
17. J. A. Landis and W. J. Bowman. Numerical study of a transpiration cooled rocket. In *AIAA, ASME, SAE, and ASEE, Joint Propulsion Conference and Exhibit, 32nd*, number AIAA 96-2580, Lake Beuna Vista, FL, July 1996.
18. W. J. Bowman, M. E. Himes, R. J. McMullan, R. C. Wier, and M. P. Wilson. A review of transpiration cooling in pipes. *AIAA*, 97-2575, 1997.
19. K. J. Kacynski and J. D. Hoffman. The prediction of nozzle performance and heat transfer in hydrogen/oxygen rocket engines with transpiration cooling, film cooling, and high area ratios. In *30th AIAA/ASME/SAE/ASEE Joint Propulsion Conference*, number AIAA 94-2757, Indianapolis, IN, June 1994.
20. D. E. Glass, A. D. Dilley, and H. N. Kelly. Numerical analysis of convection transpiration cooling. In *9th International Space Planes and Hypersonic Systems and Technologies Conference*, number AIAA 99-4911, Norfolk, VA, November 1999.
21. D. E. Glass, A. D. Dilley, and H. N. Kelly. Numerical analysis of convection transpiration cooling. *J. Spacecraft and Rockets*, 38(1):15–20, 2001.
22. A. Bucchi, C. Bruno, and A. Cungiunti. Transpiration cooling performance in LOX/methane liquid-fuel rocket engines. *J. Spacecraft and Rockets*, 42(3):476–486, 2005.
23. J. Chung, M. Bai, L. Tully, G. Jones, D. Bai, and W. Watkins. Heat transfer enhancement in a cooling channel with metal foam inserts. In *43rd AIAA/ASME/SAE/ASEE Joint Propulsion Conference and Exhibit*, number AIAA 2007-5544, July 2007.
24. E. Sozer and W. Shyy. Modeling of fluid dynamics and heat transfer through porous media for liquid rocket propulsion. In *43rd AIAA/ASME/SAE/ASEE Joint Propulsion Conference and Exhibit*, number AIAA 2007-5549, Cincinnati, OH, July 2007.
25. S. Ergun. Fluid flow through packed column. *Chem. Eng. Prog.*, 48:89–94, 1952.
26. N. W. Foster and D. Lampard. The flow and film cooling effectiveness following injection through a row of holes. *J. Engineering for Power*, 102:584–588, 1980.
27. M. Harrington, M. McWaters, D. G. Bogard, C. Lemmon, and K. Thole. Full coverage film cooling with short normal injection holes. *J. Turbomachinery*, 123:798–805, 2001.

28. G. B. Kelly and D. G. Bogard. An investigation of the heat transfer for full converage film cooling. *ASME*, GT2003-38719, 2003.
29. D. B. Spalding. A standard formulation of the steady convective mass transfer problem. *Int. J. Heat and Mass Transfer*, 1:192–207, 1960.
30. D. B. Spalding and S. W. Chi. The drag of a compressible turbulent boundary layer on a smooth flat plate with and without heat transfer. *J. Fluid Mech.*, 18:117–143, 1964.
31. D. B. Spalding. Contribution to the theory of heat transfer across a turbulent boundary layer. *Int. J. Heat and Mass Transfer*, 7:743–761, 1964.
32. F. M. White. *Viscous Fluid Flow*. McGraw-Hill, New York, 2006.
33. S. J. AlSaji. *The Transpired Turbulent Boundary Layer with Heat Transfer*. PhD thesis, Univ. Utah, 1968.
34. T. N. Stevenson. Inner region of transpired turbulent boundary layers. *AIAA*, 6(3):553–554, 1968.
35. M. W. Rubesin. An analytical estimation of the effects of transpiration cooling on the heat-transfer and skin-friction characteristic of a compressible turbulent boundary layer. Technical Report NACA TN 3341, NACA-TN-3341, 1954.
36. D. S. Hacker. Empirical prediction of turbulent boundary layer instability along a flat plate with constant mass addition at the wall. *Jet Propulsion*, 26:786, 1956.
37. H. S. Mickley and R. S. Davis. Momentum transfer for flow over a flat plate with blowing. Technical Report NACA-TN-4017, NACA, 1957.
38. E. R. Bartle and B. M. Leadon. The effectiveness as a universal measure of mass transfer cooling for a turbulent boundary layer. In *Proceedings of the 1962 Heat Transfer and Fluid Mechanics Institute*, Stanford, 1962. Stanford University Press.
39. S. S. Kutateladze and A. I. Leont'ev. *Turbulent Boundary Layers in Compressible Gasses*, pages 67–86. Academic Press, New York, 1964.
40. R. B. Kinney. Fully developed frictional and heat-transfer characteristics of laminar flow in porous tubes. *Int. J. Heat and Mass Transfer*, 11:1393–1401, 1968.
41. M. Lezuo and O. J. Haidn. Transpiration cooling using gaseous hydrogen. *AIAA*, 97-2909, 1997.
42. D. K. Huzel and D. H. Huang. *Modern Engineering for Design of Liquid-Propellant Rocket Engines*. AIAA, Washington, 1992.
43. F. Ren, J. R. Tang, L. Y. Liu, Z. Z. Wu, and H. S. Sun. Influence of transpiration cooling on turbulent boundary layer structure. *AIAA*, 98-2684, 1998.
44. T. Cebeci. *An Engineering Approach to the Calculation of Aerodynamic Flows*. Horizons, Long Beach, CA, 1999.

45. A. Teekaram, C. Forth, and T. Jones. The use of foreign gas to simulate the effects of density ratios in film cooling. *J. Turbomachinery*, 111:57–62, 1989.
46. J. P. Hartnett, R. C. Birkebak, and E. R. G. Eckert. Velocity distributions, temperature distributions, effectiveness, and heat transfer for air injected through a tangential slot into a turbulent boundary layer. *J. Heat Transfer*, 83:283–306, August 1961.
47. J. Cutbirth and D. G. Bogard. Effects of coolant density ratio on film cooling. *ASME*, GT2003-38582, 2003.
48. H. Schlichting and K. Gersten. *Boundary Layer Theory*. Springer, New York, 2000.
49. K.H. Dellimore, C. Cruz, A.W. Marshall, and C.P. Cadau. A jet model for slot film cooling with effect of variation in the mainstream pressure. In *43rd AIAA/ASME/SAE/ASEE Joint Propulsion Conference & Exhibit*, number AIAA 2007-5004, Cincinnati, OH, July 2007.
50. S. Ito, R. Goldstein, and E. R. G. Eckert. Film cooling of a gas turbine blade. *J. Turbomachinery*, 112:472–478, 1990.
51. G. Jumper, W. Elrod, and R. Rivir. Film cooling effectiveness in high turbulence flow. *J. Turbomachinery*, 113:479–483, 1991.
52. J.P. Bons, R.B. Rivir, C.D. MacArthur, and D.J. Pestian. The effect of unsteadiness on film cooling effectiveness. In *33rd Aerospace Sciences Meeting and Exhibit*, number AIAA 95-0306, Reno, NV, January 1995.
53. D. L. Schmidt and D. G. Bogard. Effects of free-stream turbulence and surface roughness on film cooling. *ASME*, 96-GT-462, 1996.
54. K. Kadotani and R. Goldstein. On the nature of jets entering a turbulent flow part B—film cooling performance. *J. Engineering for Power*, 101:488–470, 1979.
55. J. L. Rutledge. Suction side roughness effects on film cooling heat transfer on a turbine vane. Master’s thesis, Univ. Texas Austin, May 2004.
56. J. L. Rutledge, D. Robertson, and D. G. Bogard. Degradation of film cooling performance on a turbine vane suction side due to surface roughness. *J. Turbomachinery*, 128:547–554, July 2006.
57. R. L. Simpson, R. J. Moffat, and W. M. Kays. The turbulent boundary layer on a porous plate: Experimental skin friction with variable injection and suction. *Int. J. Heat and Mass Transfer*, 12:771–789, 1969.
58. P. Raghuraman, B. J. Anderson, S. N. Sieger, D. C. Rousar, J. W. Hidahl, and K. E. Baxter. The HEDI transpiration cooling concept—lightweight, durable, flight proven. In *6th AIAA/ASME Joint Thermophysics and Heat Transfer Conference*, number AIAA 94-2005, Colorado Springs, CO, June 1994.

59. L. Weiqiang, C. Qizhi, and W. Baoyuan. Transpiration cooling of rocket thrust chamber with liquid oxygen. *AIAA*, 98-890, 1998.
60. L. Weiqiang and C. Qizhi. The effect of transpiration cooling with liquid oxygen on the flow field. *AIAA*, 98-3515, 1998.
61. M. Lezuo and O. J. Haidn. Transpiration cooling in  $H_2/O_2$ -combustion devices. In *AIAA, ASME, SAE, and ASEE, Joint Propulsion Conference and Exhibit, 32nd*, number AIAA 96-2581, Lake Buena Vista, FL, July 1996.
62. H. Darcy. *Les Fontaines Publiques de la ville de Dijon*. Dalmont, Paris, 1856.
63. K. Frohlike, O. J. Haidn, and E. Serbest. New experimental results on transpiration cooling for hydrogen/oxygen rocket combustion chambers. *AIAA*, 98-3443, 1998.
64. E. Serbest, O. J. Haidn, and D. Greuel. Effusion cooling of throat region in rocket engines applying fibre reinforced ceramics. In *37th AIAA, ASME, SAE, ASEE JPC Conference and Exhibit*, number AIAA 2001-3410, Salt Lake City, UT, July 2001.
65. S.S. Dunn and D.E. Coats. Nozzle performance predictions using the TDK 97 code. *AIAA*, 97-2807, 1997.
66. D. Haeseler, C. Mading, V. Rubinsky, V. Gorokhov, and S. Khrisanfov. Experimental investigation of transpiration cooled hydrogen-oxygen subscale chambers. *AIAA*, 98-3364, 1998.
67. M. Ortelt, H. Hald, I. Fischer, D. Greuel, O. J. Haidn, and D. Suslov. Empirical verification of effusion cooled CMC rocket thrust chambers. In *41st AIAA/ASME/SAE/ASEE Joint Propulsion Conference & Exhibit*, number AIAA 2005-3569, Tuscon, AZ, July 2005.
68. M. Thames, B. Landrum, and J. B. Hendricks. Thermal/fluid study of perforated plates for transpiration cooled rocket chambers. *AIAA*, 98-3442, 1998.
69. H. N. Wang and J. H. Wang. A numerical investigation of ablation and transpiration cooling using the local thermal non-equilibrium model. In *42nd AIAA/ASME/SAE/ASEE Joint Propulsion Conference & Exhibit*, number AIAA 2006-5264, Sacramento, CA, July 2006.
70. G. Karypis and V. Kumar. A fast and high quality multilevel scheme for partitioning irregular graphs. *SIAM J. Sci. Comp.*, 20(1):359–392, 1999.
71. K.L. Harrison and D.G. Bogard. CFD predictions of film cooling adiabatic effectiveness for cylindrical holes embedded in narrow and wide transverse trenches. In *Proceedings of GT2007*, number GT2007-28005, Montreal, May 2007.
72. T.H. Shih, W.W. Lou, A. Shabbir, Z. Yang, and J. Zhu. A new  $k-\epsilon$  eddy viscosity model for high reynolds number turbulent flows. *Computers Fluids*, 24:227–238, 1995.

73. O. Kartuzova, D. Danila, M.B. Ibrahim, and R.J. Volino. CFD simulation of jet pulsation effects on film cooling of flat plates. In *Proceedings of ASME Turbo Expo 2008*, number GT2008-50284, Berlin, June 2008.
74. J. Hassan and S. Yavuzkurt. Comparison of four different two-equation turbulence models in predicting film cooling performance. In *Proceedings of Turbo Expo 2006*, number GT2006-90860, Barcelona, 2006.
75. J.L. Rutledge. *Pulsed Film Cooling on a Turbine Blade Leading Edge*. PhD thesis, Air Force Inst. Tech., September 2009.
76. J.L. Rutledge, P.I. King, and R. Rivir. CFD predictions of pulsed film cooling heat flux on a turbine blade leading edge. In *Proceedings of the IMECE*, number IMECE2008-67276, Nov 2008 2008.
77. J.F. McCall and R.D. Branam. Transpiration cooling models applied to perforated plates in a converging rocket nozzle. In *JANNAF 4th LPS Subcommittee Meeting*, number LPS-II-11, Lake Buena Vista, FL, Dec 2008.
78. S. Ou, S.V. Ekkad, and R.B. Rivir. Method of infrared thermography, 2006.
79. W.S. Anderson. Design, construction, and validation of the AFIT small scale combuston facility and sectional model of the ultra-compact combustor. Master's thesis, Air Force Inst. Tech., March 2007.
80. A. C. Eckbreth. *Laser Diagnostics for Combustion Temperature and Species*. Abacus, Cambridge, 1988.
81. S.J. Kline and F.A. McClintock. Describing uncertainties in single-sample experiments. *Mech. Eng.*, page 3, January 1953.
82. M. R. Lindeburg. *Mechanical Engineering Reference Manual*. Professional, Belmont, CA, 11th edition, 2001.



## *Vita*

Jonathan Floyd McCall was born in Canoga Park, CA in 1981. Jonathan grew up in Hesperia, CA, and graduated in May of 1998 from Sultana High School in the top 7% of his class. That summer he earned his private pilot's license (ASEL), eventually adding an instrument rating in 2001. He earned his Bachelor of Science in Aerospace Engineering at Embry-Riddle Aeronautical University in Prescott, AZ, in December 2002 where he was commissioned through ROTC as a second lieutenant in the United States Air Force. While at his first assignment to the Defense Support Program (DSP) at Los Angeles Air Force Base, CA, Jonathan was part of the launch team which delivered the final two satellites of that program to successful on-orbit service. He concurrently earned his Master of Science in Aerospace Engineering from California State University, Long Beach in May 2005, graduating in the top 1% of his class. Jonathan is a registered Professional Engineer in California. Upon completion of his Ph.D. in Astronautical Engineering at the Air Force Institute of Technology, he'll be assigned to the Air Force Research Laboratory Propulsion Directorate (RZA), Wright-Patterson AFB, OH, to work on scramjet development. Jonathan is married to a USAF Officer in the JAG Corps; together they have one son.

Permanent address: 8960 Pepperidge Ct  
Plymouth, MI 48170

<b>REPORT DOCUMENTATION PAGE</b>					<i>Form Approved</i> <i>OMB No. 0704-0188</i>	
The public reporting burden for this collection of information is estimated to average 1 hour per response, including the time for reviewing instructions, searching existing data sources, gathering and maintaining the data needed, and completing and reviewing the collection of information. Send comments regarding this burden estimate or any other aspect of this collection of information, including suggestions for reducing this burden to Department of Defense, Washington Headquarters Services, Directorate for Information Operations and Reports (0704-0188), 1215 Jefferson Davis Highway, Suite 1204, Arlington, VA 22202-4302. Respondents should be aware that notwithstanding any other provision of law, no person shall be subject to any penalty for failing to comply with a collection of information if it does not display a currently valid OMB control number. <b>PLEASE DO NOT RETURN YOUR FORM TO THE ABOVE ADDRESS.</b>						
<b>1. REPORT DATE (DD-MM-YYYY)</b> 09-09-2009		<b>2. REPORT TYPE</b> Doctoral Dissertation			<b>3. DATES COVERED (From — To)</b> Sep 2006 — Sep 2009	
<b>4. TITLE AND SUBTITLE</b>  Discrete Film Cooling in a Rocket with Curved Walls				<b>5a. CONTRACT NUMBER</b>		
				<b>5b. GRANT NUMBER</b>		
				<b>5c. PROGRAM ELEMENT NUMBER</b>		
<b>6. AUTHOR(S)</b>  Jonathan Floyd McCall, P.E., Captain, USAF				<b>5d. PROJECT NUMBER</b>		
				<b>5e. TASK NUMBER</b>		
				<b>5f. WORK UNIT NUMBER</b>		
<b>7. PERFORMING ORGANIZATION NAME(S) AND ADDRESS(ES)</b> Air Force Institute of Technology Graduate School of Engineering and Management 2950 Hobson Way WPAFB, OH 45433-7765					<b>8. PERFORMING ORGANIZATION REPORT NUMBER</b>  AFIT/DS/ENY/09-D02	
<b>9. SPONSORING / MONITORING AGENCY NAME(S) AND ADDRESS(ES)</b> Air Force Research Laboratory Propulsion Directorate 4 Draco Drive Edwards AFB, CA 93524 POC: Dr. Rich Cohn (661) 275-6177					<b>10. SPONSOR/MONITOR'S ACRONYM(S)</b>  AFRL/RZSE	
					<b>11. SPONSOR/MONITOR'S REPORT NUMBER(S)</b>	
<b>12. DISTRIBUTION / AVAILABILITY STATEMENT</b>  Approval for Public Release; distribution unlimited						
<b>13. SUPPLEMENTARY NOTES</b>						
<b>14. ABSTRACT</b>  This study quantified the effects of discrete wall-based film cooling in a rocket with curved walls. Simulations and experiments showed decreasing with wall radius of curvature, holding jet diameter constant, improves net heat flux reduction (NHFR) and adiabatic effectiveness ( $\eta$ ) for 90° compound injected cylindrical jets, though $\eta$ is reduced at the highest curvature. NHFR and $\eta$ improved further with a high favorable stream-wise pressure gradient ( $K=2.1 \times 10^{-5}$ ) at all tested blowing ratios, but were not affected much by a high density ratio ( $DR=1.76$ ) using carbon dioxide as the coolant. Experiments were run at a Reynolds number of 31K and a free-stream turbulence intensity of 26% with varying wall and jet radii. Simulations showed the Rannie transpiration model may be used to predict the cooling performance of a wall with full coverage film cooling using a correction formula based on the hole coverage area. Three improvements were made to the method of simultaneous acquisition of adiabatic wall temperature and heat flux coefficient.						
<b>15. SUBJECT TERMS</b>  rockets, film cooling, heat transfer, CFD, transpiration cooling, infrared thermography						
<b>16. SECURITY CLASSIFICATION OF:</b>			<b>17. LIMITATION OF ABSTRACT</b>		<b>18. NUMBER OF PAGES</b>	
a. REPORT	b. ABSTRACT	c. THIS PAGE	UU		178	
U	U	U				
<b>19a. NAME OF RESPONSIBLE PERSON</b> Richard D. Branam, Lt Col, USAF					<b>19b. TELEPHONE NUMBER (include area code)</b> (937) 255-3636, ext 7485	